

PROCEDURAL ANALYSES OF IMAGE-BASED AND  
MULTISCALE MATERIAL INVESTIGATIONS

by  
C. Gus Becker

**© Copyright by C. Gus Becker, 2023**  
All Rights Reserved

A thesis submitted to the Faculty and the Board of Trustees of the Colorado School of Mines in partial fulfillment of the requirements for the degree of Doctor of Philosophy (Materials Science).

Golden, Colorado

Date \_\_\_\_\_

Signed: \_\_\_\_\_

C. Gus Becker

Signed: \_\_\_\_\_

Dr. Amy Clarke  
Thesis Advisor

Golden, Colorado

Date \_\_\_\_\_

Signed: \_\_\_\_\_

Dr. Ivar Reimanis  
Professor and Department Head  
Department of Metallurgical and Materials Engineering

## ABSTRACT

Methods of material investigation often produce data in the form of images. Visual assessments can convey qualitative analyses of these images, but expressing these initial analyses in a quantitative manner is nontrivial. This work studies the role of image processing procedures in extracting information for material investigations.

The first objective of this work was to explore the feasibility of in-situ, microfocus x-radiography to monitor the composition of a binary alloy during solidification. Features in an image are represented by localized intensities which must be connected to physical quantities before quantitative information can be interpreted in an image. In this study, an image processing procedure was developed to reduce noise across a large number of radiographs captured during directional solidification. The final radiograph in the series, depicting the as-solidified sample, was compared with composition data captured via energy dispersive spectroscopy (EDS) to show radiographic intensity trends matched the compositional trends in the EDS data.

The second objective of this work was to determine the success of image processing procedures for identifying and tracking solid-liquid (S-L) interfaces during in-situ, melt pool analysis of solidification experiments. These measurements allowed for the calculation of solidification velocity. When paired with information about the thermal gradients in these experiments (obtainable by comparison with simulations), this information allows for a characterization of the structure and therefore properties of the as-solidified metal. The detection procedures were developed for synchrotron x-radiography of simulated additive manufacturing (AM) and dynamic transmission electron microscopy (DTEM) of thin film rapid solidification and compared with manual measurements. This work sought to determine whether these procedures would be able to reduce inconsistencies due to subjective judgment calls made during manual annotation. In the case of the AM simulator, the results showed large deviations due to noise, but a higher amount of the detected measurements were within the average manual distribution. For the rapid solidification, detected results matched the manual results closely.

The third objective of this work was to improve the segmentation of multi-sized, irregularly-shaped, and tightly-clustered particles in a 2D image. There are many algorithms to automatically segment features within images, but these algorithms work best for features with uniform sizes and shapes that have well-defined boundaries. In this

study, a new segmentation procedure is proposed which consists of three steps: preprocessing to over-identify particles, application of a watershed algorithm to intentionally over-segment these particles into regions, and a custom algorithm to selectively merge these over-segmented regions based on edge intensity between regions. The resulting merged-region results and the results from a typical watershed segmentation are both compared with a manual segmentation of the same image. The fit between the merged-region results and the manual segmentation is calculated to be higher than the fit between the typical watershed and manual segmentation.

The final objective of this work was to develop a flexible workflow for generating 3D geometries of granular materials from microfocus x-ray computed tomography (XCT) data. These geometries are to be used as initial conditions in image-based physics simulations. A software package called *Segmentflow* was developed to contain the workflow functions. *Segmentflow* is controlled by an input file which specifies the input data to be segmented, the segmentation parameters, and the output format of the results. The features of *Segmentflow* are exhibited by creating simulation-ready geometries from an XCT scan of a mock high explosives system consisting of F50 silica sand and a Kel-F polymer binder. The geometries are verified by analyzing the segmented particles and comparing the results to a typical size distribution of F50 sand. A variety of mesh postprocessing is also performed to show how *Segmentflow* can be used to control the complexity of a simulation.

## TABLE OF CONTENTS

ABSTRACT . . . . .	iii
LIST OF FIGURES . . . . .	ix
LIST OF TABLES . . . . .	xvi
ACKNOWLEDGMENTS . . . . .	xvii
DEDICATION . . . . .	xviii
CHAPTER 1 INTRODUCTION . . . . .	1
1.1 Research Objectives and Questions . . . . .	2
1.2 Thesis Overview . . . . .	3
CHAPTER 2 LITERATURE REVIEW . . . . .	4
2.1 X-Radiography . . . . .	4
2.2 Additive Manufacturing . . . . .	6
2.3 X-Ray Computed Tomography . . . . .	6
2.4 Image Segmentation . . . . .	7
2.5 Image-Based Modeling . . . . .	8
CHAPTER 3 INTEGRATING IN SITU X-RAY IMAGING, ENERGY DISPERSIVE SPECTROSCOPY, AND CALCULATED PHASE DIAGRAM ANALYSIS OF SOLUTE SEGREGATION DURING SOLIDIFICATION OF AN AL-AG ALLOY . . . . .	10
3.1 Abstract . . . . .	10
3.2 Introduction . . . . .	11
3.3 Methods . . . . .	13

3.3.1	Image Post-Processing and Analysis . . . . .	14
3.3.2	Post-Solidification SEM Imaging and Compositional Mapping . . . . .	15
3.3.3	CalPhiD Modeling . . . . .	16
3.4	Results and Discussion . . . . .	16
3.4.1	In Situ x-Radiography . . . . .	16
3.4.2	Backscattered Electron Image Comparison . . . . .	16
3.4.3	Solidification Calculation Comparison . . . . .	17
3.4.4	Comparing EDS and x-Radiography . . . . .	20
3.4.5	Perspectives . . . . .	23
3.5	Conclusion . . . . .	24
3.6	Acknowledgements . . . . .	25
<b>CHAPTER 4</b>	<b>PROCEDURALLY DETECTING SOLID-LIQUID INTERFACES DURING SIMULATED ADDITIVE MANUFACTURING AND RAPID SOLIDIFICATION . . . . .</b>	<b>26</b>
4.1	introduction . . . . .	26
4.2	Methods . . . . .	28
4.2.1	Ni-Mo-Al Simulated AM . . . . .	29
4.2.2	Simulated AM Detection Procedure . . . . .	29
4.2.3	Simulated AM Manual Measurements . . . . .	31
4.2.4	Al-Si Rapid Solidification . . . . .	32
4.2.5	Rapid Solidification Detection Procedure . . . . .	32
4.2.6	Rapid Solidification Manual Measurements . . . . .	37
4.3	Results . . . . .	37
4.3.1	Simulated AM Results . . . . .	37

4.3.2	Rapid Solidification Results . . . . .	39
4.4	Discussion . . . . .	40
4.4.1	AM Simulator . . . . .	40
4.4.2	Rapid Solidification . . . . .	44
4.5	Conclusions . . . . .	46
4.6	Acknowledgements . . . . .	48
<b>CHAPTER 5</b>	<b>IMPLEMENTING EDGE STRENGTH CORRECTIONS TO IMPROVE SEGMENTATION OF IRREGULARLY-SHAPED, MULTI-SIZED, AND TIGHTLY-CLUSTERED PARTICLES</b> . . . . .	<b>49</b>
5.1	Introduction . . . . .	49
5.2	Methods . . . . .	51
5.2.1	Adding a Preprocessing Routine to Generate New Markers . . . . .	52
5.2.2	Preparing Over-Segmentation . . . . .	53
5.3	Delaunay Triangulation to Connect Markers and Detect Edges . . . . .	55
5.4	Results . . . . .	57
5.5	Discussion . . . . .	59
5.6	Conclusions . . . . .	62
<b>CHAPTER 6</b>	<b>SEGMENTFLOW: A SEGMENTATION WORKFLOW PACKAGE FOR CREATING SIMULATION-READY GEOMETRIES FROM 3D IMAGE DATA</b> . . . . .	<b>64</b>
6.1	Introduction . . . . .	64
6.2	Methods . . . . .	66
6.2.1	Input Handling . . . . .	66
6.2.2	Preprocessing . . . . .	67
6.2.3	Semantic Segmentation . . . . .	67

6.3	Instance Segmentation . . . . .	69
6.3.1	Surface Mesh Creation . . . . .	70
6.3.2	Surface Mesh Postprocessing . . . . .	70
6.4	Results . . . . .	71
6.4.1	Sphere of Equivalent Volume to Determine Size . . . . .	71
6.4.2	Aspect Ratio of Bounding Box to Determine Size . . . . .	72
6.5	Discussion . . . . .	73
6.6	Conclusions . . . . .	77
CHAPTER 7	SUMMARY AND CONCLUSIONS . . . . .	79
7.1	Summary . . . . .	79
7.2	Conclusions . . . . .	79
7.2.1	Relating X-Radiography to Composition . . . . .	79
7.2.2	Procedural Analysis of Melt Pool Tracking . . . . .	80
7.2.3	Segmentation of Irregular and Tightly Clustered Particles . . . . .	82
7.2.4	Generating Image-Based Modeling Geometries . . . . .	83
CHAPTER 8	RECOMMENDATIONS FOR FUTURE WORK . . . . .	85
8.1	Optimization of AM Simulator Detection . . . . .	85
8.2	Extension of Edge Strength Corrected Segmentation . . . . .	86
8.3	Additional Segmentation Functionality for Segmentflow . . . . .	86
REFERENCES	. . . . .	88
APPENDIX	COPYRIGHT PERMISSIONS . . . . .	106
A.1	Permission from Publisher . . . . .	106
A.2	Permission from Co-Authors . . . . .	113

## LIST OF FIGURES

Figure 3.1	(a - c) In situ x-radiographs showing the mesoscale solidification of an Al-9.68 Ag at.% sample, with time shown in seconds passed since the start of solidification within the viewing window. (d - i) Additional frames for a region of interest in the middle right of the full sample. Lighter regions are Al-rich, whereas darker regions are Ag-rich. . . . .	17
Figure 3.2	(a) Post-solidification BSE image montage with the area of the sample analyzed through in situ x-radiography indicated by the red overlay. (b) BSE image rotated and cropped to the x-radiography analysis area with the yellow overlay corresponding to the region of interest in Figure 3.1.d - i. (c) BSE image with grayscale values inverted to facilitate visual comparison to x-radiography with the region of interest once again indicated by the yellow overlay. (d) X-radiograph of the fully solidified sample (939 s after the start of solidification). Yellow overlay corresponds to the same region of interest as in (b) and (c). . . . .	18
Figure 3.3	(a) An equilibrium Al-Ag phase diagram with the sample composition (Al-9.68 Ag at.%) indicated by a red line. (b) Thermo-Calc solidification calculations showing Ag concentrations in the liquid and solid phases (Scheil, solid lines) and phase percentages (Equilibrium, dotted lines). . . . .	19
Figure 3.4	(a) Comparison between the Scheil solidification simulation results expressed as solid composition versus fraction solid (blue) and the Scheil solid composition data mapped to the fraction solid as measured in this region of the radiographs (orange). (b) Mapping fraction solid to composition of the solid at the point of solidification (at% Al) during in situ x-radiography. Color represents decreasing Al content of the solid forming during solidification. . . . .	19
Figure 3.5	(a) BSE image of an Al-Ag sample showing the position of an EDS line scan measuring the Al content. (b) X-radiograph of the same sample region, post-solidification. (c) Al content from the EDS line scan (orange) and the transmitted x-ray intensity (blue), collected across the length of the lines in (a) and (b) respectively. Each dataset is standardized to a unitless range for comparison. EDS features annotated as c1 - 10 correlate to x-radiography features annotated as c1' - 10', respectively. . . . .	21

Figure 3.6	(a) BSE image of an Al-Ag sample showing the position of an EDS line scan measuring the Al content. (b) X-radiograph of the same sample region, post-solidification. (c) Al content from the EDS line scan (orange) and the transmitted x-ray intensity from the x-radiograph (blue). Each dataset was standardized to a unitless range for comparison, with data collected across the length of the lines in (a) and (b), starting at the top left endpoint of the line and moving towards the bottom center of the images. . . . .	22
Figure 4.1	Subset of a time sequence of x-radiography depicting the solidification of a Ni-1.9 Mo-6.6 Al (wt.%) single crystal after melting with a laser at 104 W (20% maximum power). (a) Full image of radiograph right after the laser shuts off ( $t = 0 \mu\text{s}$ ). (b) Radiograph from (a) cropped to the melt pool and immediate surroundings ( $t = 0 \mu\text{s}$ ). (c) Cropped radiograph showing partial solidification and visible solid-liquid (S-L) interface ( $t = 100 \mu\text{s}$ ). (d) Cropped radiograph showing further solidification and a smaller S-L interface ( $t = 200 \mu\text{s}$ ). (e) Cropped radiograph showing near total solidification with S-L interface no longer easily visible ( $t = 300 \mu\text{s}$ ). . . . .	30
Figure 4.2	The procedural image processing routine for identifying the solid-liquid (S-L) interface for a radiograph taken during the solidification portion of the experiment. (a) Raw radiograph showing the melt pool and S-L interface. (b) Smoothing with a Gaussian filter and subtraction from the succeeding smoothed radiograph in the time sequence. (c) Intensity rescaling by clipping the top and bottom five percent intensities. (d) Denoising and intensity inversion. (e) Upper minimum threshold to convert to binary image. (f) Skeletonization to create one-pixel wide regions. . . . .	31
Figure 4.3	(a - d) Subset of radiography sequence, showing the solid-liquid interface receding throughout the experiment. (e - f) Skeletonized regions overlaid in red on subset of radiography sequence, showing the as-detected position of the solid-liquid interface throughout the experiment. . . . .	32
Figure 4.4	(a) Dynamic transmission electron microscope (DTEM) image showing nine frames of a rapidly solidifying Al-3 Si sample with a $20 \mu\text{s}$ delay and $2.5 \mu\text{s}$ capture interval. The chronology of the experiment starts with the lower right image, moves up the right column, down the center column, and finally up the left column to end at the top left image. (b) The same image with false color highlighting intensity differences across the image. . . . .	33

Figure 4.5	(a - c) Subset of frames with intensity unchanged following extraction from full DTEM image. Frames correspond to 20 $\mu$ s, 30 $\mu$ s, and 40 $\mu$ s after the laser melted the sample. (d - f) Pseudo flat-field images created with large-sigma Gaussian filter and mean-filled background. Created from corresponding frames (a - c). . . . .	34
Figure 4.6	Comparison between raw DTEM frames and intensity-rescaled frames following pseudo-flat-field correction. (a - c) Subset of frames with intensity unchanged following extraction from full DTEM image. Frames correspond to 20 $\mu$ s, 30 $\mu$ s, and 40 $\mu$ s after the laser melted the sample. (d - f) Subset of frames following pseudo flat-field images created with large-sigma Gaussian filter and mean-filled background. Created from corresponding frames as (a - c) and pseudo flat-field images (Figure 4.5.d - f). . . . .	35
Figure 4.7	Series of morphological operations to automatically mask the liquid region of each solidifying frame from the DTEM image. (a) Upper minimum threshold of 20 $\mu$ s frame (Figure 4.6.d). (b) Result of morphological opening of (a) to severe small connections across the solid-liquid interface followed by filtering of regions smaller than the mean area of all the regions present. (c) Inversion of b followed by removal of regions connected to the border. (d) Selection of region in (c) with largest area. (e) Morphological closing of (c) to connect small gaps across the solid-liquid interface that were not disconnected in the opening in (b). (f) Filling of all holes to create the final identified region. . . . .	36
Figure 4.8	(a - c) Subset of normalized frames depicting Al-Si solidification 20 $\mu$ s, 30 $\mu$ s, and 40 $\mu$ s after the laser melted the sample. (d - f) Roughly elliptical identified regions containing the melt pools resulting from the series of morphologic operations (Figure 4.7.a - f) applied to each frame. . . . .	37
Figure 4.9	(a - c) Subset of normalized frames depicting Al-Si solidification 20 $\mu$ s, 30 $\mu$ s, and 40 $\mu$ s after the laser melted the sample. (d - f) Identified regions overlaid with fitted ellipses generated by finding ellipse parameters that match the centroid and second moment of the identified regions. The color of the pixels show the extent to which the fit matches the identified region. True fit pixels are within both the identified region and the ellipse (green), misfit pixels are beyond the identified region but still within the ellipse (yellow), and unfit pixels are beyond both the identified region and the ellipse (blue). . . . .	38

Figure 4.10	(a - c) Subset of normalized frames depicting Al-Si solidification 20 $\mu$ s, 30 $\mu$ s, and 40 $\mu$ s after the laser melted the sample. (d - f) Identified regions overlaid with ellipses of optimized fit. Optimization maximizes true fit match (green) and minimizes misfit match (yellow) and unfit match (blue). The starting point of the optimization are the ellipses of matching centroid and second moment (Figure 4.9. d - f).	39
Figure 4.11	Optimized fitted ellipses overlaid on each rescaled frame as yellow dashed lines.	40
Figure 4.12	Interfaces detected by the automated procedure (blue) compared with manually identified interfaces (orange, green, and red) for the 104 W experiment. Interface location is defined by the distance from the bottom of the solid-liquid interface to top of the image, starting when the laser shuts off ( $t = 0 \mu$ s).	41
Figure 4.13	Interfaces detected by the automated procedure (blue) compared with manually identified interfaces (orange, green, and red) for the 156 W experiment. Interface location is defined by the distance from the bottom of the solid-liquid interface to top of the image, starting when the laser shuts off ( $t = 0 \mu$ s).	42
Figure 4.14	Interfaces detected by the automated procedure (blue) compared with manually identified interfaces (orange, green, and red) for the 208 W experiment. Interface location is defined by the distance from the bottom of the solid-liquid interface to top of the image, starting when the laser shuts off ( $t = 0 \mu$ s).	43
Figure 4.15	Size of melt pools over time throughout the third rapid solidification experiment. The detected ellipses (blue) have a low deviation from the manually measured interfaces (orange, green, and red).	44
Figure 4.16	Size of melt pools over time throughout the third rapid solidification experiment. The detected ellipses (blue) have a low deviation from the manually measured interfaces (orange, green, and red).	45
Figure 4.17	Size of melt pools over time throughout the third rapid solidification experiment. The detected ellipses (blue) have a low deviation from the manually measured interfaces (orange, green, and red) until the end of the experiment.	46
Figure 5.1	(a) Raw image depicting sand particles sliced from a 3D CT scan. (b) Binary image created from the raw image with Otsu thresholding. Yellow regions represent foreground pixels (valued one) while purple regions represent background pixels (valued zero).	52

Figure 5.2	(a) Image depicting sand particles sliced from a 3D CT scan. (b) Euclidean distance transformation of Otsu-binarized image (Figure 5.1.b) with local maxima denoted by red points. (c) Watershed segmentation of inverted Euclidean distance transformation seeded by local minima of the inverted distance transformation (red points). . . . .	53
Figure 5.3	(a) Image depicting sand grains sliced from a 3D CT scan. (b) Image rescaled to the range defined by the 5th and 95th percentile intensities. (c) Rescaled image after histogram equalization to enhance maxima within the particles. (d) Histogram-equalized image converted into a ternary image following application of a multi-Otsu algorithm with three classes. (e) Binary image created by thresholding the with uppermost value calculated by multi-Otsu algorithm. All holes within resulting regions of binary image are filled. (f) Euclidean distance transformation of multi-Otsu binary image with local maxima denoted by red points. . . . .	54
Figure 5.4	(a) Rescaled image depicting sand grains (Figure 5.3.b). (b) Rescaled image after application of a Sobel filter to enhance the edges of particles within the image. (c) Sobel-filtered image after adaptive histogram equalization is performed to further enhance particle edges. . . . .	55
Figure 5.5	(a) Rescaled image depicting sand grains overlaid with inverted distance transformation minima in red. (b) Edge image (Figure 5.4.c) with minima overlaid. White points are removed by filtering process for being too close to the particle edges while red points will be used as markers for the watershed segmentation. (c) Edge-filtered local minima (red) overlaid on the rescaled image. . . . .	55
Figure 5.6	(a) Image depicting sand grains to be segmented. (b) Euclidean distance transformation of multi-Otsu-binarized image (Figure 5.3.e) with edge-filtered local maxima denoted by red points. (c) Watershed segmentation results of the inverted Euclidean distance transformation seeded by the edge-filtered local maxima in previous image. . . . .	56
Figure 5.7	(a) Edge-filtered maxima used as markers (red) overlaid on the edge image (Figure 5.4.c). (b) Edge image overlaid with Delaunay triangulation. Red lines denote lines across which an edge was detected while white lines denote lines across which no edges were detected. Markers connected by white lines are defined as existing in the same “particle neighborhood”. . . . .	58

Figure 5.8	(a) Image depicting sand particles to compare with segmentation results. (b) Over-segmented regions resulting from extended watershed routine, but before regions are merged (Figure 5.6.c). Red points correspond to marker used to segment the region. (c) Final segmented regions after merging neighboring regions without a separating edge (Figure 5.7.b). Each red point corresponds to the marker of a merged region closest to the average location of all the centroids of the merged neighboring regions. . . . .	59
Figure 5.9	(a) Manual segmentation from hand drawing individual overlays on each visually discernible sand grain. (b) Typical watershed segmentation (Figure 5.2). This segmentation achieves an 82.09% match with the manual segmentation. (c) Watershed segmentation with red overlay depicting pixels mismatched from the manual segmentation. (d) Manual segmentation plotted again for ease of comparison with merged-region segmentation. (e) Merged-region segmentation from merging over-segmented neighboring regions without a separating edge (Figure 5.8). This segmentation achieves an 87.02% match with the manual segmentation, approximately a 7% improvement from the typical watershed segmentation. (f) Merged-region segmentation with red overlay depicting pixels mismatched from the manual segmentation. . . . .	60
Figure 6.1	Histogram processing used to determine the threshold values to perform semantic segmentation on images. The blue line represents the raw histogram. The orange line represents the smoothed histogram. The red points denote the local maxima. The green points denote the local minima between these maxima which are used to threshold the material classes. . . . .	68
Figure 6.2	(a) Low contrast image slice from raw CT scan. (b) Image slice after intensity is rescaled. (c) Semantic segmentation following thresholding of rescaled image using the minima of the smoothed histogram (Figure 6.1). The purple regions represent the void class, the blue regions represent the binder class, and the yellow regions represent the sand grain class. . . . .	69
Figure 6.3	Expected result from passing F50 sand through a series of sieves, expressed in percent of total grains retained at each step. Sieve size is given in microns. . . . .	72

Figure 6.4	Size distribution of segmented particles binned according to the sphere of equivalent volume of each particle. Solid lines represent the cumulative distribution of particles at increasing sieve sizes. The blue solid line represents the typical values for F50 sand and the other solid lines represent the values determined from the particles obtained by segmenting the CT scan with a watershed algorithm seeded with different values for the minimum peak distance ( $d_{seed}$ ). Dashed lines of corresponding color represent the error between the segmentation and typical values. . . . .	73
Figure 6.5	Size distribution of segmented particles binned according to the bounding box aspect ratio of each particle. Solid lines represent the cumulative distribution of particles at increasing sieve sizes. The blue solid line represents the typical values for F50 sand and the other solid lines represent the values determined from the particles obtained by segmenting the CT scan with a watershed algorithm seeded with different values for the minimum peak distance ( $d_{seed}$ ). Dashed lines of corresponding color represent the error between the segmentation and typical values. . . . .	74
Figure 6.6	Surface meshes of all 41,553 particles segmented from the F50 sand sample loaded from three different views: (a) the top, (b) a high angle, and (c) the side. . . . .	75
Figure 6.7	(a) A slice of the rescaled intensity CT scan image with particles of interest labeled to allow for ease of comparison and discussion between the three segmentations. (b) Corresponding slice of Segmentation B, as seeded by markers selected with a 5 pixel minimum peak distance, with the second lowest total accumulated error in particle size. (c) Corresponding slice of Segmentation C, as seeded by markers selected with a 6 pixel minimum peak distance, with the lowest total accumulated error in particle size. (d) Corresponding slice of Segmentation D, as seeded by markers selected with a 7 pixel minimum peak distance, with the third lowest total accumulated error in particle size. . . . .	76
Figure 6.8	(a) Surface mesh produced from a segmented particle. Mesh originally has 1524 triangles across its surface. (b) Smoothing applied to surface mesh as part of the mesh postprocessing capabilities of <i>Segmentflow</i> . (c) Mesh simplified beyond 200 triangles. (d) Mesh simplified beyond 20 triangles. . . . .	77

## LIST OF TABLES

Table 6.1 Segmented Particle Errors Relative to Typical F50 Sand . . . . . 75

## ACKNOWLEDGMENTS

I would like to acknowledge and thank the following people and groups: Dr. Amy Clarke and Dr. Kester Clarke for guiding the research presented here; the nondestructive testing group E-6 at Los Alamos National Laboratory, the National Nuclear Security Administration through the Predictive Sciences Academic Alliance Program, the Office of Naval Research through the Multidisciplinary University Research Initiatives program, and the Center for Advanced Non Ferrous Structural Alloys (CANFSA) for funding different portions of this work; Dr. Jonah Klemm-Toole and Dr. Daniel Adams for their valuable input as part of my thesis committee; and my family and friends for supporting me along the way, including the many other students at Mines and collaborating universities whose collaborations, feedback, and advice made this work possible.

For my partner Kaila.  
I will always be grateful for your love and support during this time!

## CHAPTER 1

### INTRODUCTION

Image processing is an important part of many scientific workflows involving data collected in the form of images. Image processing can be used to improve clarity in images, highlight specific content or objects, extract quantitative information, and more. In the realm of quantitative information extraction, sizes of objects and/or regions can be measured.

X-radiography is the process of generating images using x-rays transmitted through a material. Contrast in these images come from x-ray absorption properties of the material being imaged, thus materials with localized compositions and material structures/phases can be differentiated in these images.

X-ray computed tomography (XCT) is the process imaging a material in three dimensions by capturing a series of two-dimensional x-radiographs from a variety of angles around a central axis such that a three-dimensional reconstruction of the images can be created. This reconstruction is representative of the volume of the material imaged.

Metal additive manufacturing (AM) is the process of creating a part layer-by-layer, as opposed to more traditional subtractive processes. AM is an umbrella term for a variety of processes that may include powder or wire feedstock fused together in some way, typically by melting with laser or electron beam.

Image segmentation is a form of image processing in which one or multiple features in an image are separated from the rest of the image. This separation is done by splitting an image into There are different methods for segmenting images, but the simplest is by setting a threshold value, and creating a binary image which defines a foreground of regions of the image that are of-interest, and defines features as separate from the background. This often requires image segmentation, in which an image is split into two or more regions which can then be classified and analyzed to convey information about intensity, size, location, shape, and/or distribution of the features. Image segmentation can be performed on a single image, or a volume (often represented as a series of images acting as slices).

## **1.1 Research Objectives and Questions**

The objective of this project was to explore the role of image processing procedures in material investigation. This was done by investigating the connection between x-radiography intensity and composition of a binary alloy, developing procedures for tracking solid-liquid interfaces during solidification experiments, extending watershed segmentation procedure to improve results for nonuniform particles, and developing a software package for informing physics simulation with initial conditions from x-ray computed tomography data. The following questions were developed to address these objectives:

- 1. How can in-situ x-radiography be used in conjunction with other methods of analysis to infer composition of an Al-Ag alloy during solidification?*

Studies have been performed using calibration experiments to relate x-ray image intensity to composition during solidification of binary alloys. To study whether these calibration experiments are necessary, directional solidification of an Al-Ag alloy was monitored with in-situ, microfocus radiography. The radiograph intensity was compared to energy dispersive spectroscopy and the data were analyzed for similar trends.

- 2. How successful is an image processing procedure at automating the identification, tracking, and velocity calculation of solid-liquid interfaces during in-situ solidification experiments?*

Identifying, tracking, and analyzing the solid-liquid interface in solidification experiments is necessary to extract important information like solidification velocity and melt pool shape, but the task of manually tracking interfaces is time consuming and prone to human error and biases. Using traditional image processing methods, routines were developed to identify, track, and analyze the solid-liquid interfaces in additive manufacturing simulator experiments as well as rapid solidification experiments captured with a dynamic transmission electron microscope. The resulting melt pool locations were used to calculate solidification velocities and compared to results from manually tracking the interfaces.

- 3. How can the segmentation of multi-sized, irregularly-shaped, and tightly-clustered particles be improved?*

Watershed segmentation is a common method for segmenting objects in an image from other objects and from the background. One method of performing these types of algorithms is by “seeding” the algorithm with “marker” points. Each marker will become a segmented region, so controlling the marker points is one way to control the results.

Often markers are narrowed down using the distance between adjacent points, but this distance can be extremely variable for multi-sized and irregularly-shaped. Delaunay triangulation, which is an algorithm which generates a connected grid of points, is tested to determine if it can be used along with edge strength to filter markers across varying distances.

*4. How can a workflow be designed to extract 3D geometries from x-ray computed tomography data such that the geometry of a physical sample can be reproduced digitally for use as initial conditions in an image-based physics simulation?*

X-ray computed tomography (XCT) is a useful tool for nondestructive testing of materials. A mock high explosives system of F50 silica sand coated in Kel-F, a polymeric binder, was subject to XCT to generate a set of 3D images. *Segmentflow*, a Python-based, segmentation workflow software package was developed to enable the segmentation of individual sand grains within the XCT data. Based on parameters specified in an input file, *Segmentflow* can output the segmented grains in a variety of formats to be used in physics simulations.

## 1.2 Thesis Overview

This thesis seeks to answer the research questions outlined above through the presentation of eight chapters. This first chapter serves as an introduction to the rest of the work, including a brief background section that defining major concepts. Chapter 1 provides a more in-depth presentation of concepts covered by way of literature review. The next four chapters, Chapters 3 - 6, are published or intend to be published. Chapter 3 is based on work published in the Journal of The Minerals, Metals and Materials Society. This chapter explores the feasibility of comparing analyses of x-radiography images to compositional mapping of the same sample. Chapters 4 - 6 are each separate manuscripts intended for publication. Chapter 4 describes analyses procedures developed to calculate solidification velocities procedurally for two separate solidification experiments. The results of each procedure are compared to manual measurements. Chapter 5 presents a new procedure for segmenting irregular and tightly-packed particles, extended from current procedures commonly referred to in literature. Chapter 6 presents a software package developed to establish a segmentation workflow and create geometries to be used in image-based physics modeling. Chapter 7 summarizes the work across the chapters and provides some conclusions. Finally, Chapter 8 provides recommendations for future work following the work covered in this thesis.

## CHAPTER 2

### LITERATURE REVIEW

This chapter presents background information necessary to understand the motivations behind the work presented in this thesis.

#### 2.1 X-Radiography

In a university laboratory in 1895, Wilhelm Conrad Röntgen was studying cathode rays when a crystal began mysteriously fluorescing. Further investigation led Röntgen to believe he had discovered a previously unknown type of radiation. He developed experiments to compare these newly discovered rays with visible light and published the data, using the term “x-rays” to describe this new type of radiation “for the sake of brevity” [1]. Röntgen also includes the first published x-radiographic image, or radiograph, in this work: a human hand showing the skeleton within and a ring on one finger.

Today, x-radiography is a powerful tool that takes advantage of the interaction between matter and photons in the x-ray energy range. Photons can be absorbed, reflected, and transmitted through matter. By exposing a sample of interest to x-ray photons, information can be inferred about the volume of the exposed sample by detecting the transmitted. The extent of transmitted photons collected on the surface of a detector convey information as a two-dimensional projection. The projection of transmitted x-rays was first recorded via photographic film, but x-rays are now typically converted to visible light via scintillator and captured on a charge coupled device (CCD) that converts the visible light into a digital radiograph. The intensity of each pixel in a radiograph is proportional to the number of photons incident to a corresponding location on the detector over some integration time. High photon flux on the detector corresponds to regions of a material with high x-ray transmittance, whereas lower photon flux corresponds to regions of the material absorbing or otherwise deflecting x-rays. Regions of the detector recording many photon interactions are represented as light pixels in the radiograph, whereas regions recording fewer photon interactions are represented by darker pixels. Since x-radiography can convey information about the inside of a material without physically exposing the inside, the technique is often classified as a non-destructive testing technique.

There are many challenges associated with x-radiography applied to the study of materials. The x-rays generated from traditional x-ray sources are typically created by

impinging an electron beam onto an anode. The spatial resolution of the x-radiography possible with x-rays generated in this manner can be improved by focusing the electron beam onto a micron-sized area. While x-rays were quickly adopted in the medical field and to other static applications, the technique wasn't applied to the in-situ study of materials until Miller and Beech utilized an x-ray tube with a micron-sized focus area to study the solidification of binary alloys [2]. In this study, the authors demonstrate x-radiography of Al-Cu and Al-Sn during solidification with a spatial resolution of 10  $\mu\text{m}$ , noting choice of alloy system as an important factor in this type of in-situ study. Light alloys with low x-ray absorptive coefficients serve as good candidates, as this allows for a greater rate of x-ray transmission, minimizing the exposure time for the transmitted x-rays and therefore reducing blur in the image. The authors also note that contrast is improved in binary alloys in which the x-ray absorptions of the constituent elements differ. In a following study, Miller et al. detail their experimental setup [3]. For samples of 300  $\mu\text{m}$  thickness, two recording methods are explained. Film is used to report a spatial resolution of 10  $\mu\text{m}$  with an exposure time that varies from 0.4 to 2.5 s and an interval between exposures from 5 to 30 s as the film is pulled by hand to be advanced. A continuous observation method is also reported using a TV monitor, allowing pictures of the screen to be taken with an exposure time of 0.03 s, however the spatial resolution is compromised to hundreds of microns due to the resolution limitations of the fluorescent screen. Even still, the field-of-view is around 50  $\text{mm}^2$  to each side. Subsequent studies with similar x-ray systems use in-situ x-radiography to observe the dissolution of solid gold and silver into the less-dense, liquid sodium [4], the diffusion of ions [5], and further metallic solidification [6–9]. This method eventually become known as microfocus x-radiography due to the micron-scale focus area necessary to produce x-rays with sufficient imaging properties.

Mathiesen et al. published early work using synchrotron sources for x-radiographic analyses of materials [10]. Until this time, the only in-situ study of materials with synchrotron x-rays had been x-ray topography, in which an image is constructed based on differences of the extent of diffraction of incident x-rays [11]. This differs from a radiographic image in which the extent of absorption is exploited for image contrast. Just like with x-radiography, x-ray topography was first applied to the in-situ observation of materials with laboratory x-ray sources [12–14] but later studies extended the method to synchrotron x-ray sources [15, 16]. The research performed by Mathiesen et al. used x-rays generated by synchrotrons to observe dendritic solidification in Sn-Pb and Al-Cu alloys, stating this type of work was not feasible with the spatial and temporal resolutions possible with synchrotron x-ray topography or microfocus x-radiography at the time

[10, 17]. The authors report spatial resolutions around  $2.5\text{ }\mu\text{m}$  and exposure times of as little as 0.25 s. This increased resolution comes at the cost of a  $1.4\text{ mm}^2$  field-of-view, which is smaller than achievable with microfocus x-radiography. In 2011, the portability of microfocus x-radiography was exhibited with a study that developed a setup to enable x-radiography in microgravity for the study of solidification [18]. This led to a sounding rocket study in which the solidification of an Al-Cu alloy was observed solidifying *in situ* with microfocus x-radiography [19]. The improved spatial and temporal resolutions possible with synchrotron x-radiography make the technique preferable compared to microfocus x-radiography for *in-situ* studies of quickly developing material processes occurring at the near-microscope scale [20–22].

## 2.2 Additive Manufacturing

Additive manufacturing (AM), in which 3D parts are built layer by layer, as opposed to traditional subtractive processing methods, is an area of materials research where high spatial and temporal resolutions are important. Observing these AM processes *in situ* can further the understanding of the connections between processing parameters and developed microstructures in resulting as-built parts. Direct AM processes can be divided into powder bed fusion (PBF) and direct energy deposition methods (DED) [23, 24]. PBF methods involve a focusing energy to melt or sinter powder [25, 26], whereas DED methods generate a melt pool with focused energy into which additional material is deposited [27]. Laser powder bed fusion (LPBF) is an example of a PBF process in which a laser is scanned across a bed of powder, layer by layer, according to 3D model data. The powder is melted, and upon solidification, is joined to the layer below [28]. Simulated LPBF was monitored *in situ* using synchrotron x-radiography was achieved with a temporal resolution of  $20\text{ }\mu\text{s}$  (50 kHz frame rate) to monitor the [29]. This technique has enabled many *in-situ* studies of LPBF including the evolution of vapor-filled depression, or keyhole, morphologies [30], fluid dynamics in the melt pool [31, 32], pore formation [33], powder spattering [34], melt pool variation [35], and dynamic fracture behavior [36].

## 2.3 X-Ray Computed Tomography

X-ray computed tomography (XCT) is another useful technique to aid in the study of AM processes. This technique is not *in situ*, but XCT can data is 3D in nature and can advance understandings of dynamic processes by analyzing the properties of parts built using AM processes. Experiments varying processing parameters like laser power, scan

velocity, and scan spacing, followed by analysis of resulting parts with synchrotron XCT enabled the connection between processing parameters and porosity in electron beam PBF [37] and LPBF [38].

Microfocus x-rays can also been used to study AM processes using XCT, and present some benefits compared to synchrotron XCT. Microfocus x-ray sources are capable of higher x-ray energies than synchrotron x-rays. Higher energy x-rays have a higher penetration capability, allowing for imaging of larger samples. This allows for AM studies to be performed at the scale of full parts. Microfocus XCT, or microCT, has connected processing parameters to resulting porosity for a full cubic sample with an edge length of 5 mm [39]. Imaging at the scale of a full part has also enabled the analysis of 3D surface roughness of an AM-built structure [40]. In addition to higher x-ray energies, microCT also has the benefit of being performed in a laboratory, as opposed to a synchrotron user facility. This experimental flexibility is represented in a workflow developed to quantifying porosity and enable the optimization of AM processing parameters for quality control purposes [41].

## 2.4 Image Segmentation

Image segmentation is an important tool in CT analysis workflows as well as other image-based methods of analysis. Segmentation is the isolation of specific features in an image such that those features can be analyzed and quantified. For example, the pores identified in the studies mentioned previously [39, 41] were segmented from the surrounding sample in order to analyze their location, size, and distribution. In 2D image analyses, segmentation is often performed manually by annotating features in an image using graphical user interface (GUI) software such as ImageJ [42] or even with Python using packages such as napari [43]. Annotation may involve placing points on an image or drawing boundaries such that the image can be divided into separate regions. Specifying a threshold value is another method of segmenting an image which removes some of the workload required when manually annotating images. This is especially useful in 3D data when features are spread across multiple images. By selecting an intensity value, the image can be segmented into two regions above or below that value, either in a single 2D image or a stack of 2D images representing a 3D volume. This type of method is still manual because the threshold value is chosen, however algorithms also exist for calculating a threshold value for a given image. Otsu's method is a thresholding algorithm that calculates one or multiple threshold values based on the distribution of intensities in an image and the desired number of classes into which the image will be segmented [44].

Watershed segmentation is a technique that can be used to algorithmically segment features in an image [45–48]. The name comes from a metaphor used to describe the technique: a simulated flooding process is applied to an image that acts as a topographic surface. The “water” starts at a level below all intensities (elevations) in the image, and rises progressively. The first time water rises above the level of a region unconnected to another filled region, it creates a new catchment basin. Wherever two catchment basins come together, a “dam” is constructed, demarcating the segmented regions when the flooding is over. In addition to basic watershed segmentation in the simulated water floods the image uniformly, marker-based watershed segmentation is also possible in which seed points, or markers, are used as starting points for the flooding, causing these points to act as “pour points,” using the same metaphor [49, 50]. Watershed algorithms are also able to operate in 3D even though the flooding metaphor does not withstand the addition of a dimension. Watershed algorithms serve an important role in the workflows of many fields, from cell nuclei [51, 52] to stone aggregates [53, 54].

Any image passed into an image analysis algorithm yield the same results, improving reproducibility of image analysis workflows. It’s important to note that reproducibility is not the same thing as objectivity. This is not only because algorithms are human constructs, but also because the implementation of algorithms involves subjective decisions [55]. While the same image input into an algorithm will yield the same results, the application of any preprocessing steps can alter the results. To maximize reproducibility, it is important to note every step in an image analysis workflow. This can be done by listing out processing steps performed or by writing analysis workflows as scripts that can be run again using software like Python or MATLAB. Even GUI software like ImageJ sometimes have the capability recording or writing workflows as reproducible macros or scripts. *Jupyter* notebooks are another good option for image analysis workflows [56]. The cell-based structure of *Jupyter* notebook files enables incremental execution of processes to show results of a workflow at multiple phases, rather than at the end only. This can be useful to see how an image evolves through a process.

## 2.5 Image-Based Modeling

Beyond revealing information statistical information about the size, shape, and distribution of features in an image, the results from image segmentation can be used in computer simulations. In biology and biophysics, CT scans and MRIs of organs enable realistic geometries in the simulation of computational fluid dynamics (CFD) of bloodflow [57], heat transfer for cancer cryosurgery [58], tumor shrinkage and treatment planning in radiation therapy [59–61], and electromechanical turbulence in the heart [62]. In

neuroscience, fluorescent microscopy and structured illumination microscopy enable cell-modeling of non-neuron brain cells [63] and computational geometry analysis of neuron features [64]. In the study of Li-ion batteries, focused ion beam scanning electron microscopy, EDS, and XCT enabled the mechanical and electrochemical response simulations [65–68]. In materials science synchrotron XCT enabled the characterization and simulation of thermal conductivity in 3D composite textile architectures for space applications [69–71] and microscale finite element modeling of fiber reinforced polymers [72–74]. In geoscience, microfocus XCT enabled the simulation of CFD in porous media at the pore scale [75]. In each of these cases, segmentation was used in some form, but segmentation is not perfect, and quantifying uncertainty in segmentation results is a way to understand how that uncertainty can affect the simulations in which the segmentations are used [60, 76].

# CHAPTER 3

## INTEGRATING IN SITU X-RAY IMAGING, ENERGY DISPERSIVE SPECTROSCOPY, AND CALCULATED PHASE DIAGRAM ANALYSIS OF SOLUTE SEGREGATION DURING SOLIDIFICATION OF AN AL-AG ALLOY

Modified from a paper [77] published in JOM: Journal of the Minerals, Metals and Materials Society<sup>1</sup>.

C. Gus Becker<sup>2,3</sup>, Damien Tourret<sup>4</sup>, Doug Smith<sup>2</sup>, Brian Rodgers<sup>2</sup>, Seth Imhoff<sup>5</sup>, John Gibbs<sup>5</sup>, James Hunter<sup>5</sup>, Michelle Espy<sup>5</sup>, Kester Clarke<sup>2</sup>, and Amy Clarke<sup>2</sup>.

### 3.1 Abstract

High-energy, microfocus x-ray imaging, or x-radiography, is a useful tool for in situ analysis and monitoring of materials processing. Large fields-of-view, spatial and temporal resolutions sufficient for mesoscopic imaging, and high-energy x-rays capable of probing metallic alloy samples make the technique attractive for in situ solidification studies in the laboratory. Here, we demonstrate the usefulness of high-energy, microfocus x-radiography in the laboratory, particularly when paired with complementary techniques. Multimodal, multiscale characterization was performed, including x-radiographic analysis of solidifying Al-Ag and compositional analysis of the same sample after solidification with scanning electron microscopy (SEM) and energy dispersive x-ray spectroscopy (EDS). The dynamics observed through x-radiography during solidification are compared to the compositional results obtained by EDS. The fraction solid measured in radiographs is also used in combination with a calculation of phase diagrams (CalPhaD) Scheil solidification simulation to reconstruct a spatiotemporal microsegregation map. The multimodal, multiscale characterization techniques presented here illustrate a promising pathway toward improved analyses and monitoring of materials processing within a laboratory setting.

---

<sup>1</sup>Reprinted with permission of the publisher of JOM, Springer Nature.

<sup>2</sup>Colorado School of Mines, 1500 Illinois St, Golden, CO 80401, USA

<sup>3</sup>Corresponding author

<sup>4</sup>IMDEA Materials Institute, Calle Eric Kandel 2, Getafe, 28906 Madrid, Spain.

<sup>5</sup>Los Alamos National Laboratory, P.O. Box 1663, Los Alamos, NM 87545

### 3.2 Introduction

In situ observation is not in itself new to the study of solidification. New methods are constantly developed and improved to capture new information through in situ observation, as evidenced by recent reviews on in situ solidification observation [78–80]. Two dominant methods of producing x-rays allow for useful in situ x-ray imaging, or x-radiography: microfocus sources and synchrotron sources. In a microfocus x-ray source, a stream of electrons from a high-voltage power source is focused on a small spot on an anode. As the electrons impinge the surface of the anode, x-rays are generated through bremsstrahlung radiation. In a synchrotron source, x-rays are produced when high-velocity electrons in a synchrotron facility are forced to change directions by magnetic fields. Each method of producing x-rays has its benefits. Synchrotron x-radiography produces a high flux of photons to capture images, enabling spatial resolutions typically around 1  $\mu\text{m}$  and temporal resolutions high enough to capture early-stage solidification phenomena [81]. However, the field-of-view (FOV) in these experiments is not as large as microfocus experiments, typically only about 1  $\text{mm}^2$  [82]. Additionally, these experiments require a particle accelerator to create the radiation, so experiments need to be scheduled and performed at a user facility. Microfocus x-ray sources are also typically able to produce higher energy x-rays, allowing for successful imaging of thicker or higher atomic number ( $Z$ ) materials. Spatial and temporal resolutions of microfocus systems are lower than those of synchrotron facilities, but still competitive at up to 5  $\mu\text{m}$  and 6 Hz, respectively [83].

Transmittance of x-rays through a material depends on variables such as thickness, sample geometry, and material composition. In uniformly thin metallic samples, elemental composition plays a large role, as higher  $Z$  atoms absorb and deflect more x-rays than lower  $Z$  atoms [84]. The Al-Ag binary system, while considered a model age-hardening alloy due to solid-state precipitation behavior characterized at an atomic level [29], is also favorable for in situ x-radiography experiments. This is because the large  $Z$  difference of the two elements allows for high-intensity contrasts in captured images. This property is the motivation for using an alloy in the Al-Ag system for the current work.

Solidification processes have been observed in situ since the 1960s when transparent, organic compounds were observed to solidify in ways similar to metals, exhibiting planar, cellular, and dendritic growth [85]. In the 1970s, sealed-tube x-ray sources were first used to monitor solidification of metals [86]. In the late 1980s, synchrotron x-ray topography was used to monitor the solidification of steel using TV

monitors [15], followed by synchrotron x-ray topography of the Al-Cu binary system [16], and finally time-resolved x-ray imaging/x-radiography of binary alloys in the late 1990s/early 2000s [17, 82]. In the early 2010s, microfocus x-radiography was suggested as a method to perform *in situ* solidification experiments in a laboratory setting rather than at a synchrotron source, resulting in a microfocus setup being brought aboard the International Space Station as a way of performing *in situ* x-radiography of solidification of metals in micro-gravity [83], with similar experiments performed on sounding rockets [19] and parabolic flights [87].

Synchrotron x-radiography has been used to map x-ray intensity to composition through comparison with analysis performed with an electron probe microanalyzer (EPMA) [21]. Compositions have also been applied to x-radiography intensity, using calibration experiments involving phases of known composition to create a mapping function from radiograph intensities to composition [21, 88–93]. This type of method was used, for instance, to determine concentrations of solidifying Al-Ge from x-radiography intensities to compare with dendritic needle network simulations of the same system [94, 95]. These works provide a promising method for relating x-radiography intensity to composition when a calibration experiment is involved. When calibration experiments cannot be performed, it is of interest to determine whether x-radiography pixel intensities can still be used to infer *in situ* composition values during processing of materials. This current work explores the ability of pairing microfocus x-radiography with post-solidification compositional analysis similar to the aforementioned EPMA method, but more suitable for a laboratory setting.

On its own, x-radiography reveals relative variations affecting x-ray transmittance through a sample (e.g., Z differences), so it cannot be used to quantify composition gradients in a solidifying alloy, but certain types of microscopy are able to measure composition post-solidification. Scanning electron microscopy (SEM) is a versatile technique in which a focused beam of electrons is rastered across a sample surface to produce a variety of signals collected for imaging and microanalysis on the sub-micron scale. Two common signal types are backscattered electrons (BSE) and characteristic x-rays. Backscattered electrons are used to image microstructures. Contrast in these images is strongly influenced by compositional variations across the sample surface, because the BSE signal intensity increases with Z [96]. For this reason, BSE imaging is commonly paired with compositional mapping performed through energy dispersive spectroscopy (EDS) of characteristic x-rays.

In this article, we demonstrate a laboratory-based, multimodal approach to the multiscale characterization of metals during solidification, using the Al-Ag system as an

example. This technique bridges the mesoscopic length scale of high-energy, microfocus x-radiography with the microscopic length scale of EDS. By correlating data from each method of analysis, one can obtain a greater amount of information than could be determined from either method of analysis on its own. Scheil solidification calculations are performed to further contextualize the results and to provide a methodology to link phase fractions and compositions obtained during solidification. We also discuss some promising pathways linking simulations and experiments to further expand the breadth of data extracted from both in situ and post-solidification analyses.

### 3.3 Methods

A dynamic solidification set-up previously used for in situ synchrotron x-radiography was used to capture the dynamic solidification of an Al-9.68Ag at% sample measuring  $10 \times 17 \times 0.25$  mm. This thickness was chosen to constrain solidification structures to a single plane so that multiple features were not layered on top of each other when projected onto the 2D plane of the image. The sample was inserted into a boron nitride crucible, transparent to x-rays, which was placed in a vertically oriented steel rod assembly aligned with a window in the path of the x-rays to aid in transmission. Heating elements at the top and bottom of the rod assembly controlled a temperature gradient across the rod and sample, and allowed for controlled directional solidification. Details about the setup (as it was used previously for synchrotron x-radiography solidification experiments) can be found in the supplemental material of previous work [22, 97].

An X-Com 225 microfocus x-ray source was operated at a voltage of 206 kV, a current of 150  $\mu$ A, and a focal spot size of 30  $\mu$ m to generate the x-rays for radiography. A scintillator placed downstream from the sample and the source converted the x-rays transmitted through the sample to visible light, so the photons could be captured by a Varian CCD with a  $127 \times 127$   $\mu$ m pixel pitch and an integration time of 200 ms, correlating with a capture framerate of 5 Hz. A total of 6022 images were captured in an elapsed time of 1205 s. The geometric magnification from the placement of the sample between the source and detector resulted in a spatial resolution of 11  $\mu$ m per pixel in the radiographs and a  $21 \times 16$  mm FOV ( $>350$  mm $^2$ ). Since the experimental set-up for the solidification experiment was originally designed for use at a synchrotron facility, the collected radiographs capture a much larger area than was designed to be captured by synchrotron radiography. Of the entire FOV, only an area measuring  $8.3 \times 4.4$  mm (approximately 36 mm $^2$ ) is analyzed, which is still significantly larger than a typical maximum interrogated area in synchrotron x-ray experiments of approximately  $1.5 \times 2$  mm (approximately 3 mm $^2$ ).

### 3.3.1 Image Post-Processing and Analysis

To prepare the images for analysis, an image processing routine was performed across the entire set of images. A series of Python functions were developed to process the images loaded as numerical arrays. A series of open source packages were used to aid in this process: *Jupyter* notebooks for performing an iterative analysis while maintaining a reproducible workflow [56], *NumPy* for representing the images as numerical arrays and performing fast calculations [98], *imageio* for loading the images into the arrays [99], *scikit-image* for performing image-processing algorithms [100], and *napari* for visualizing and annotating the data with an interactive, multi-dimensional image viewer [43].

The first step in the processing routine is to crop the experimental image set to the smaller region of interest. Since the steel rod containing the crucible and solidifying sample has a window for the sample, the rest of the rod does not transmit as many x-rays outside the region containing the sample. Cropping out these regions and the lighter regions beyond the rod enable the greatest contrast range to be assessed across the solidifying structures of the sample. Once the images are cropped to within the window, a dark image (captured without the sample or x-rays present) and a beam image (captured without the sample but with x-rays present) are used to spatially normalize the images. The dark image is subtracted from the image set and divided by the difference of the beam image and the dark image, which reduces the intensity of artifacts in the image set introduced by the beam and the detector. The spatially normalized image set is temporally normalized by multiplying by the mean of each image and dividing by the total mean of the entire image set. This reduces intensity variations across the set of images. At this point, the pixels of each image corresponding to the 1st and 99th percentile are clipped to further increase contrast. To smooth out small variations in the images, while maintaining sharp edges between features within the images, a median filter is applied for each image.

The next phase of the processing routine separates a 50-image subset of the image set, in which the sample remains fully liquid, to normalize the solidifying portion of the sample to the liquid state. This normalization reduces artifacts in the image introduced by the sample assembly, including any nonuniformities in the crucible. The 50 images in which the sample is fully liquid (having undergone the previously described processing routine) are averaged together to form a single average liquid image, at which point each image in the solidifying portion of the image set is divided by this average liquid image. The final steps of the image-processing routine rotate the normalized images and

rescale the intensities of each image to the full range of the floating-point data type.

### 3.3.2 Post-Solidification SEM Imaging and Compositional Mapping

Following solidification, SEM was used to perform BSE imaging. Due to a faint, vertical brightness gradient in the as-captured BSE images, ImageJ [42] was used to apply a bandpass filter to the fast Fourier transform of each image prior to stitching in Image Composite Editor software. This approach flattened the images to ensure uniform brightness and contrast across the entire x-radiography FOV.

EDS was also used to evaluate the distribution of solute content along features of interest within the x-radiography FOV. To mitigate topographic effects, the sample was prepared by polishing through a 1  $\mu\text{m}$  diamond suspension solution. Backscatter imaging was performed at 30 kV in a Tescan S8252G dual-beam focused ion beam, and EDS line scan data were collected with an EDAX Octane Elect Plus detector. Collecting  $>10$  k counts per pixel significantly reduced noise in the EDS data, and led to semi-quantitative ZAF composition results in the APEX<sup>TM</sup> software.

EDS and x-radiography line profiles were compared across two regions in the Al-Ag sample. Image data from each technique were first manually aligned so that the line profiles would correspond to the same locations on the sample. The process of aligning the data involved taking the BSE montage and overlaying it on the processed radiograph, representing the sample at a point in time at the end of solidification. The large montage image allowed for multiple points of reference across the sample to correctly match the scale, translation, and rotation of the BSE montage relative to the radiograph. With the montage in place, images locating the EDS line scan on a smaller BSE image of each region were overlaid on the larger radiograph-BSE alignment, using surface defects of the BSE images to match the scale, translation, and rotation between the images. This portion of the analysis was done using Python and the *napari* image viewer, which allowed for layers corresponding to each image to be scaled, translated, and rotated relative to each other, while maintaining the ability to adjust opacity for each image layer to ensure an optimal alignment.

A one-dimensional median filter was applied to the EDS data to reduce noise in the signal. The line intensity profile from the radiograph was measured using Python and the measure submodule from *scikit-image*. The intensity profile was averaged across a line with a thickness of three pixels to reduce noise. To make comparisons between these datasets, even though they were collected through different modes of analysis (and therefore have different units corresponding to signal amplitudes), the datasets were standardized by subtracting the mean from each dataset and normalizing by the

standard deviation. The mean subtraction centers each dataset around zero to align each dataset vertically. Dividing by the standard deviation normalizes the variation in each of the datasets to a unitless range, allowing for variation from the mean to be compared, even though the original scales were not the same. The variation from the mean for each dataset should be similar if each is varying due to similar phenomena, e.g., the compositional differences present from solidification that we expect to see.

### 3.3.3 CalPhaD Modeling

Solute microsegregation has been modeled following Scheil solidification (assuming that no Ag diffusion occurs in the solid state and perfect mixing is maintained in the liquid) [101] and lever rule (full equilibrium) solidification. These calculations were performed by the calculation of phase diagrams (CalPhaD) method using Thermo-Calc software with the TCAL7 database.

## 3.4 Results and Discussion

This section compares the in-situ x-radiography, the backscattered electron images, and calculations from solidification theory and discusses how the methods viewed together provide more context about the material when viewed together than each of the methods would provide on their own.

### 3.4.1 In Situ x-Radiography

A subset of the sequence of processed x-radiographs presented shows the solidifying Al-rich dendrites and the progressively Ag-enriched liquid (Figure 3.1). Light and dark pixel intensities correspond to the Al-rich and Ag-enriched regions, respectively.

### 3.4.2 Backscattered Electron Image Comparison

Multiple post-solidification BSE images were used to create a single BSE image montage for comparison with the x-radiography data at the end of solidification (Fig. Figure 3.2). Because BSE signal intensity increases with Z [96], regions of high Ag concentrations are represented by lighter areas in the image, while darker areas represent low Ag concentrations. This being the case, it is reasonable to conclude that the small pits observed in very light regions inherited high Ag contents (e.g., from enriched interdendritic liquid) relative to their surroundings, leading to corrosion during polishing. In the radiographs, the intensity relationship is reversed because regions of

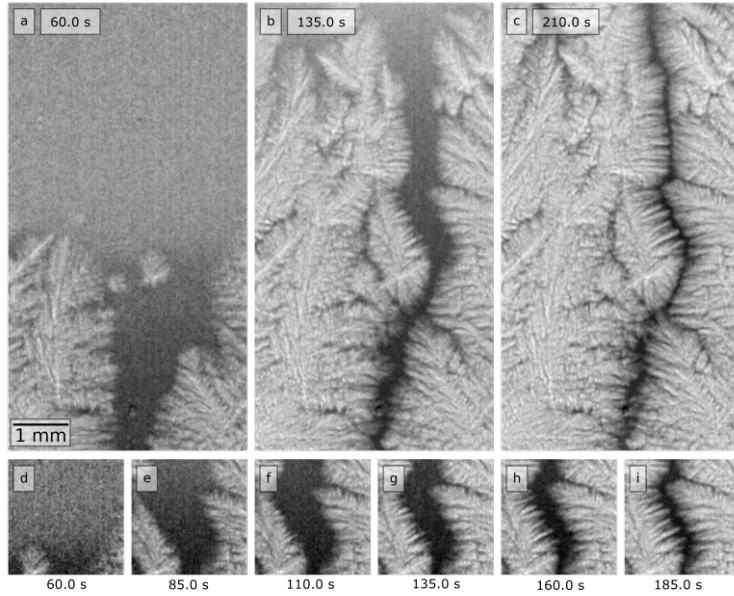


Figure 3.1 (a - c) In situ x-radiographs showing the mesoscale solidification of an Al-9.68 Ag at.% sample, with time shown in seconds passed since the start of solidification within the viewing window. (d - i) Additional frames for a region of interest in the middle right of the full sample. Lighter regions are Al-rich, whereas darker regions are Ag-rich.

high Ag decrease the transmission of x-rays, resulting in darker pixels. Despite differences in spatial resolution and signal depth between these two techniques, the BSE images (Figure 3.2.a, b) are perceived as inverted relative to the x-radiography (as expected). To allow for a clearer comparison, an inverted BSE image is included (Figure 3.2.c) to show the similarities in the solidified features with the fully solidified x-radiograph (Figure 3.2.d). This observation highlights the fact that Z values have a strong influence on contrast in x-radiography.

### 3.4.3 Solidification Calculation Comparison

Following the frame progression during solidification in Figure 3.1.d - i, the first solid to form is a light-colored dendrite. According to the phase diagram (Figure 3.2.a), this primary solid is expected to have a low Ag content, which causes the interdendritic fluid to become enriched with Ag. As solidification continues, Ag concentrations in both the recently frozen solid and the remaining liquid increase as the Al-rich solid continues to partition Ag into the liquid. The Scheil solidification model is shown and compared with the evolution of the fraction of phases using an equilibrium (lever rule) solidification path (Figure 3.2.b).

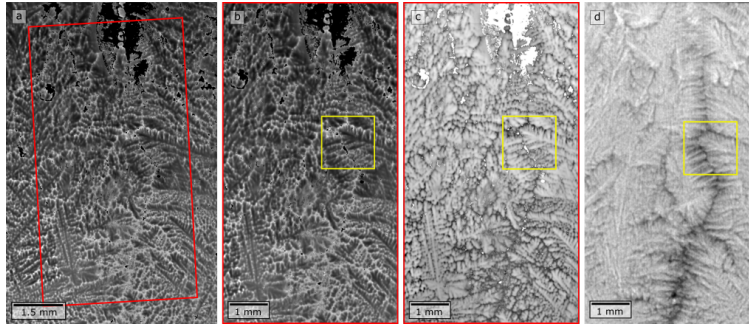


Figure 3.2 (a) Post-solidification BSE image montage with the area of the sample analyzed through in situ x-radiography indicated by the red overlay. (b) BSE image rotated and cropped to the x-radiography analysis area with the yellow overlay corresponding to the region of interest in Figure 3.1.d - i. (c) BSE image with grayscale values inverted to facilitate visual comparison to x-radiography with the region of interest once again indicated by the yellow overlay. (d) X-radiograph of the fully solidified sample (939 s after the start of solidification). Yellow overlay corresponds to the same region of interest as in (b) and (c).

In the Scheil calculation results (Figure 3.3.b), as expected from the phase diagram, Ag concentration is found to increase for both the liquid and solid phases during solidification, and the solidus temperature is reduced from the equilibrium value of 587°C to the eutectic temperature at around 566°C, as indicated by the ends of the Scheil curves (solid lines) compared to the equilibrium fractions (dotted lines). At this temperature, the Scheil model indicates that the remaining liquid reaches the eutectic point (33 mole percent Ag) and solidifies as an  $(\text{Al} + \gamma)$  microconstituent. The trend of progressive Ag enrichment in the liquid phase is consistent with the BSE images and x-radiographs.

The results obtained from the Scheil calculations can also be compared directly to the radiographs by measuring the fraction solidified at different times during solidification. Using Python, solid regions were identified and manually labeled by tracing the solid structures on label layers in the napari image viewer. This created binary mask images which were overlaid on each other to show the progression of the solidification. These binary masks were then analyzed using the measure submodule of scikit-image to compare the area solidified of each image to the total area of the images. At this point, the as-measured fraction solid, with each image representing different solidification temperatures, was compared to the Scheil simulation results expressed as fraction solid and temperature. By aligning the as-measured fraction solid with the Scheil calculated fraction solid, a mapping was made from solidification temperature (position in image sequence) to solid composition (Figure 3.4.a). The measurement of fraction solid does

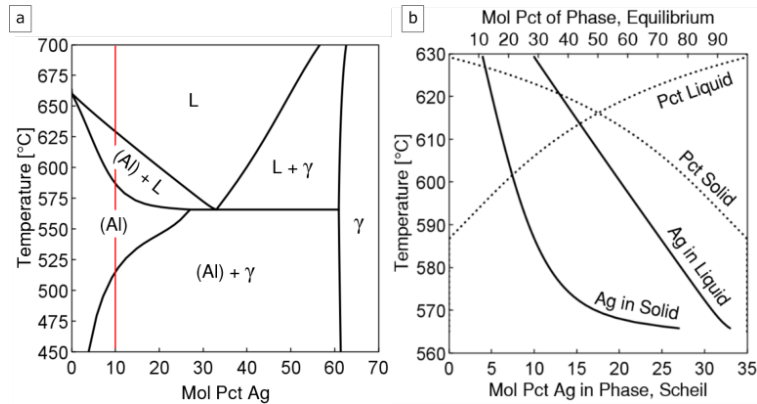


Figure 3.3 (a) An equilibrium Al-Ag phase diagram with the sample composition (Al-9.68 Ag at.%) indicated by a red line. (b) Thermo-Calc solidification calculations showing Ag concentrations in the liquid and solid phases (Scheil, solid lines) and phase percentages (Equilibrium, dotted lines).

not continue for the full range of solidification because the solidification occurred slowly at the end of the experiment, so the best fitting portion of the Scheil simulation also does not reach complete solidification. This image number to solid composition mapping from the Scheil simulation at any given instant was then used to estimate the concentration of the solid formed between two successive radiographs, ultimately constructing a spatiotemporal solute microsegregation map (Figure 3.4.b).

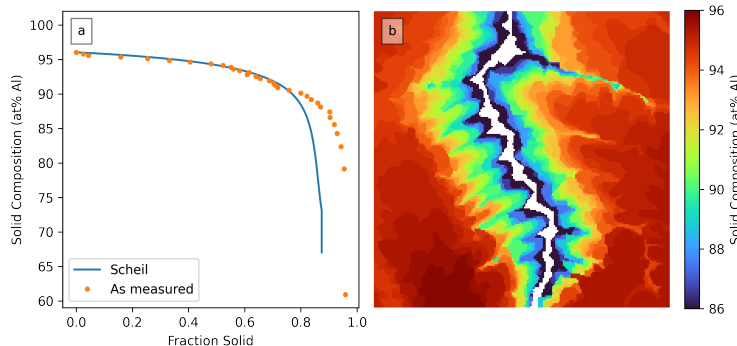


Figure 3.4 (a) Comparison between the Scheil solidification simulation results expressed as solid composition versus fraction solid (blue) and the Scheil solid composition data mapped to the fraction solid as measured in this region of the radiographs (orange). (b) Mapping fraction solid to composition of the solid at the point of solidification (at% Al) during in situ x-radiography. Color represents decreasing Al content of the solid forming during solidification.

Using this matching procedure between Scheil simulation results and radiographs, which is based on the observable solid fraction, the agreement between simulation and

experiments lead to a good match (Figure 3.4.a) for most of the freezing range, with some deviation at high solid fraction. This is directly due to a discrepancy in solid fraction between model and experiments: given the underlying assumption that the cooling rate is homogeneous and constant, temperature (simulation) and time (x-radiography) axes are thus kept linear with respect to each other, which in turn results in the deviation in fraction versus composition estimation at high solid fraction (Figure 3.4.a). This discrepancy could, to some extent, be addressed by relaxing the assumption of homogeneous and constant cooling rate, allowing it to deviate from this ideal case locally (in time and space), for instance, by directly using the concentration versus solid fraction curve from the CalPhaD calculation to estimate the concentration profile (instead of the solid fraction versus time and/or temperature). Another possible source of error stems from how the fraction solid was measured in the radiographs. Since the x-rays travel through the entire volume of the sample, liquid trapped between dendrites or dendrites that form but do not span the entire thickness of the sample could be measured as a fully solid area, even though they represent a volume that may not be completely solid. Additionally, only a single region of interest of the sample is analyzed in this way, so it is also possible that this region is not completely representative, as some solute may enter and exit this region to other portions of the sample, and temperature may also vary beyond this region. While the current 2D analysis already provides a reasonable estimation of the solid fraction, it might be further enhanced using contrast-based volumetric reconstruction through the sample.<sup>35</sup> An important feature of the microsegregation analysis technique proposed here is that, while approximate and relying on strong assumption (e.g., CalPhaD-based solidification path), it is straightforward to extend to multicomponent solute mapping. This would be impossible to obtain through radiography analysis alone and could provide an important tool for further analysis of time-dependent *in situ* imaging data.

### 3.4.4 Comparing EDS and x-Radiography

Comparisons between the EDS-determined compositions and the radiograph intensities can be made, despite differences in the techniques for collecting these datasets. These comparisons were made by using Python and the napari image viewer to manually overlay the BSE montage image, the individual BSE images containing the overlay of the line scan locations, and the x-radiograph showing the fully solidified structure. With these images aligned, a line could be placed on the x-radiography in the location corresponding to the EDS line scan, such that the corresponding pixel intensity of the x-radiograph could be determined. While pixel intensities in x-radiography convey

information about composition due to varying Z of the material in the sample, the intensities also convey information about the entire thickness of the sample. This is contrasted with the volume sampled by EDS, which is only on the order of 3  $\mu\text{m}$  from the metallographically prepared surface (approximately 30  $\mu\text{m}$  below the surface of the as-solidified sample). Since this volume is about two orders of magnitude smaller than the volume probed by x-radiography (already the small approximately 250  $\mu\text{m}$  thickness), the EDS is more akin to an analysis of the surface. These differences need to be considered when comparing the data. A comparison of an EDS line scan showing the Al content over the length of the line shows similar trends to the x-ray intensity profile of a line in the same location on the aligned radiograph (Figure 3.5).

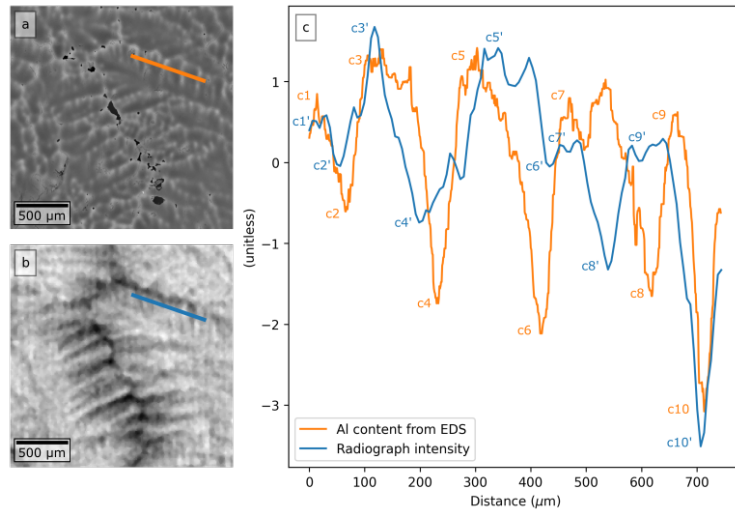


Figure 3.5 (a) BSE image of an Al-Ag sample showing the position of an EDS line scan measuring the Al content. (b) X-radiograph of the same sample region, post-solidification. (c) Al content from the EDS line scan (orange) and the transmitted x-ray intensity (blue), collected across the length of the lines in (a) and (b) respectively. Each dataset is standardized to a unitless range for comparison. EDS features annotated as c1 - 10 correlate to x-radiography features annotated as c1' - 10', respectively.

Annotations along the datasets in Figure 3.5.c show features consistent across the length of the line across the sample for both EDS and radiography. The line is oriented such that the beginning is near the tip of a primary dendrite, traveling along the secondary dendrite arms towards the areas that were first to solidify. Many correlated features exist between these datasets, such as the maxima annotated in Figure 3.5.c as c1 and c1', c3 and c3', and c5 and c5', and the minima annotated as c10 and c10'. Differences between the datasets can be reasonably explained considering the nature of the acquisition techniques. One way these discrepancies could manifest is through local

maxima or minima in the datasets not centered at the same location along the lines. Volume measurements captured by x-radiography are expected to deviate from the surface measurements captured by EDS in the case when a given feature in the sample (e.g., a secondary dendrite arm) may not be oriented in a way that places its center of volume directly in line with the cross-section measured at the surface by EDS.

Another manifestation of the discrepancies that arise due to the differences in volume versus surface effects of these two modes of analysis is considered in the region of the sample analyzed across well-defined secondary dendrite arms (Figure 3.6). The EDS and radiograph profile data is normalized in the same way as in Figure 3.5, and, although we see correlations between the minima and maxima of the datasets, the general trend across the entire length of the EDS data exhibits maxima and minima (corresponding to Al-rich dendritic and Ag-rich interdendritic regions, respectively) at similar intensities (orange line, Figure 3.6.c). In contrast, the x-radiography intensity (blue line) progressively increases across the length of the line.

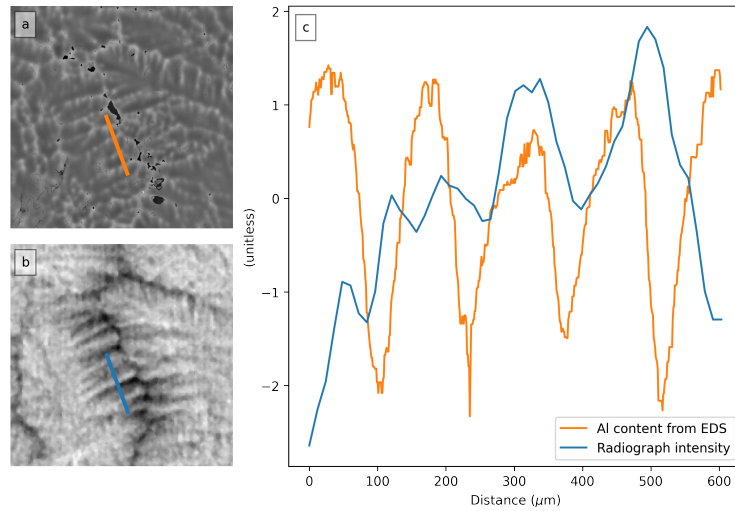


Figure 3.6 (a) BSE image of an Al-Ag sample showing the position of an EDS line scan measuring the Al content. (b) X-radiograph of the same sample region, post-solidification. (c) Al content from the EDS line scan (orange) and the transmitted x-ray intensity from the x-radiograph (blue). Each dataset was standardized to a unitless range for comparison, with data collected across the length of the lines in (a) and (b), starting at the top left endpoint of the line and moving towards the bottom center of the images.

One possibility for this discrepancy could be the decreasing thickness of the dendrite arms along the length of the line, rather than composition differences. Progressively increasing intensity in x-radiography data corresponds to progressively higher transmission of x-rays. Hence, the secondary dendrite arms further along the length of

the line of analysis could be progressively thinner, allowing for more x-rays to be transmitted. This may not be visible at the surface after solidification is complete (and therefore would not show in the EDS data). Even if the dendrite arms were the same size and shape, differing orientations with respect to each other could still cause the dendrite arms to have more volume in the path of the x-rays.

Another possibility that may explain some mismatch between the datasets is the existence of multiple layers of dendrites or of sidebranches within the sample thickness. In the annotations of Fig. Figure 3.6.c, most of the features of the EDS data are seen to correlate with the x-radiography, except for the feature annotated as c3. In the radiography, c3' consists of two separate peaks, whereas, in the EDS, what we see can be considered a higher single peak (with some noise). Possibly, a secondary dendrite arm between the two EDS maxima c1 and c3, but below the surface, such that it would be behind these other two surface dendrites, could lead to this additional local maximum in the radiography data, whereas it would remain undetectable from surface analysis. When we compare the areas around the length of the line on the SEM image (Fig. Figure 3.6.a) and the radiograph (Figure 3.6.b), we see the correlation between dendrite arms c1 and c1'; however, the interdendritic region c2 and the following dendrite arm c3 are clear in the EDS data, but neither c2' nor c3' is clear in the radiograph. Solid-state diffusion is another possibility to alter the compositions of the final, as-solidified microstructure measured by EDS, relative to those that exist just after solidification and observed by radiography.

While direct comparisons between x-radiography and EDS remain challenging, especially due to differences arising between the volume-probing nature of x-radiography and the surface analysis nature of EDS, the combination of these characterization methods enables relative changes during materials processing to be analyzed in a laboratory setting. Three-dimensional analysis, such as 3D computed tomography, could be considered as an additional concurrent data source, which would support or discard such interpretations of through-thickness features in the sample. Future work and some of the potential exploration pathways deriving from this work are briefly mentioned in the following section.

### 3.4.5 Perspectives

Combining both *in situ* and post-solidification diagnostics, as well as modeling and simulation tools, offers many exploration pathways for ongoing and future work. Using CalPhaD alone, several ways of reconstructing the microsegregation profile may be envisioned, only one of which has been illustrated here. Frameworks may be considered

that would for instance combine (1) compositional analysis directly from the gray-level radiographs [90–94, 102] (however, limited to binary alloys for a semi-quantitative analysis), (2) microsegregation simulations using different approaches, such as lever rule, Gulliver-Scheil, or models accounting for finite diffusivities (e.g., using CalPhaD-based or other volume-averaged methods [103]), and (3) further post-solidification compositional analyses, such as wavelength dispersive spectroscopy, the amount of redundancy with EDS possibly being used as a cross-validation tool or for more comprehensive analysis.

Combining *in situ* imaging data and simulations also provides numerous promising avenues for data analysis of transient conditions during solidification, and determination of physical parameters otherwise extremely challenging to estimate, if measurable at all. One recent example of such analysis is combined time-resolved 3D x-ray tomography data with phase-field modeling of grain growth to extract grain boundary mobilities and their orientation dependence over a statistically relevant sample size [104]. In the context of solidification, several crucial parameters are particularly challenging to obtain, one example of which is the anisotropy of solid-liquid interfacial properties like the excess free energy and its anisotropy. *In situ* imaging could be combined with corresponding simulations of microstructural evolution using phase-field modeling at the scale of a representative volume element [105] or other “mesoscale” solidification simulations using, for instance, envelope-based or needle-based approaches, providing further insight into *in situ* data at the scale of entire experiments [94, 106]. A rigorous integration of simulation and experiments will most likely involve the use of advanced statistical analysis techniques for large and highly multidimensional datasets, such as machine learning.

### 3.5 Conclusion

This work demonstrates a monitoring technique combining the mesoscopic, volume-probing investigation of high-energy, microfocus x-radiography and the microscopic, compositional analysis of SEM EDS, supported by Scheil solidification calculations. *In situ* x-radiography can provide relative composition and solid fraction evolutions by pixel intensity changes during solidification, while post-solidification EDS can provide more quantitative compositional information, but only after processing of the material and with localized surface analysis. The pairing of the data received through volume-probing x-radiography with compositional surface analysis captured by EDS creates a multimodal montage of data that is greater than the sum of its parts. The combination of these concurrent datasets with modeling data, here illustrated using

simple CalPhaD-based Scheil calculations, could reveal nuances beyond those directly accessible through either the imaging, compositional mapping, or simulations taken separately. Further development and calibration of the techniques illustrated here will allow for *in situ* compositional monitoring capabilities of dynamic processing of metals within a laboratory setting. Potential exists for a completely non-destructive, *in situ* monitoring technique available in the laboratory, with which a sufficient number of samples could be analyzed by x-radiography and EDS, supported by modeling data and perhaps calibration experiments, to provide a comprehensive way to capture important information about solidification dynamics. Furthermore, a database could be created to link radiograph intensities with EDS-derived compositions for enough relevant conditions (i.e., sample chemistries and geometries, processing conditions, etc.), combined with modern, fast-acting real-time post-processing (e.g., based on machine-learning algorithms), such that compositions could be inferred *in situ* with reasonable accuracy.

### 3.6 Acknowledgements

The microfocus x-radiography was supported by the US Department of Energy, Office of Science, Basic Energy Sciences under award no. DESC001606. The SEM EDS and preparation of this manuscript were supported by the US Department of Energy, Office of Science, Basic Energy Sciences under award no. DE-SC0020870. Los Alamos National Laboratory is operated by Triad National Security, LLC, for the National Nuclear Security Administration of US DOE (Contract No. 89233218CNA000001). The Tescan dual-beam FIB was funded through the support of the National Science Foundation (DMR-1828454). Many of the figures in this text were generated using Python [107], Matplotlib [108], and the open-source vector editing software InkScape [109].

# CHAPTER 4

## PROCEDURALLY DETECTING SOLID-LIQUID INTERFACES DURING SIMULATED ADDITIVE MANUFACTURING AND RAPID SOLIDIFICATION

In this chapter, procedures for detecting metallic melt pools are presented to automate the process of obtaining real-time solidification velocities to enable comparisons to process modeling and microstructural outcomes predicted by solidification theory and modeling. Procedures are developed to analyze two types of solidification experiments: simulated metal additive manufacturing (AM) of Ni-1.9 Mo-6.6 Al (wt.%) single crystals captured with x-radiography at the Advanced Photon Source (APS) synchrotron facility at Argonne National Laboratory (ANL) and rapid solidification of Al-3 wt.% Si thin films captured with dynamic transmission electron microscopy (DTEM) at Lawrence Livermore National Laboratory (LLNL). Each procedure differs due to the nature of the experiment, but each utilizes common Python libraries including *NumPy*, *imageio*, *scikit-image*, and *napari*, to perform steps including denoising, pseudo-flat-field intensity correction, segmentation, and optimization of ellipse fitting. The procedures are applied to three experiments of each type and the detected melt pool evolution is compared with manual measurements to show that the procedures are reasonably accurate. The AM simulator procedure is more prone to inaccuracies due to noise, and therefore less reliable than the rapid solidification procedure, which is more robust, partly due to a fit optimization step.

### 4.1 introduction

Metal additive manufacturing (AM) encompasses a promising collection of manufacturing techniques in which metallic parts are created layer by layer. These techniques can create parts with complex geometries that are not achievable with more traditional, subtractive techniques [110]. However, these techniques are not without their own challenges. AM-built parts often produce columnar dendrites during solidification. These anisotropic microstructures can lead to hot tearing [111–113]. While there has been some success leveraging anisotropy to intentionally localize properties in AM-built parts [114, 115], isotropic microstructures are usually preferred to reduce the tendency for cracks to form. This requires the growth of equiaxed grains as opposed to columnar grains. Many methods have been successful in encouraging equiaxed grain growth, including alteration of alloy composition [116–118], addition of grain nucleating

nanoparticles [112, 113], changing build height [119], changing feedstock rate [119, 120], and changing laser/electron beam processing parameters like power [119, 121, 122], scan speed [119–121], scan strategy [114, 122], and beam shape [123]. A series of models have enabled studies of the effects of beam processing parameters on melt pool dynamics and resulting microstructures. The first of such models was developed by Hunt to analytically describe the growth of equiaxed grains ahead of the columnar solid-liquid (S-L) interface, shedding light on the columnar-to-equiaxed transition (CET) [124]. This original CET model was developed for casting applications, but the Kurz-Giovanola-Trivedi model describing rapid solidification in the growth of columnar dendrites [125] enabled Gäumann et al. to extend Hunt's model to rapid solidification [126, 127]. The latter work of Gäumann et al. provided a simplified relationship between temperature gradient (G), solidification velocity (V), and a material constant (K), which enables predictions for when an alloy system undergoes equiaxed versus columnar growth. Using this relationship, studies have predicted and verified microstructures for varying processing parameters by comparing V, as calculated from experiments, and G, as estimated with heat transfer simulations in G-V maps [114, 123, 125, 127? –131]. These microstructure maps overlay experimental data with regions corresponding to columnar, equiaxed, and mixed microstructures. Microstructure maps can also be express process parameters directly, rather than G and V, to determine combinations of processing parameters likely to produce optimal microstructures [132, 133].

With the opportunity to view melt pool evolution and development of microstructures under AM-like conditions *in situ* comes the task of tracking image features across the duration of solidification. This feature tracking is often performed manually with some kind of image viewing and annotation software like *ImageJ* [42]. Manual tracking has been used to track droplet spatter [31, 134], melt pool length/depth and overall area shrinkage [134], pores [31, 33], vapor depression/keyhole depth [30, 33], powder motion and spattering [34], melt flow within the melt pool via tracing particles [135], and melt pool volume [35].

Most studies in literature do not explore automated methods of analyzing melt pool features, although a procedural method for identifying interfaces of melt pools has received a brief explanation in some studies [29, 136]. In these studies, the interfaces are identified on a row-by-row basis, based on local peaks in the second derivative of the radiographs. This methodology is provided in the supplementary materials, however, and no further explanation is given into how the peaks of the derivatives corresponding to the interfaces are selected from the other peaks present.

The goal of this work was to investigate the possibility of automating analyses necessary to calculate solidification velocities for the prediction of microstructure based on processing parameters. The successful execution of this type of automation would remove some inaccuracies related to human error and inconsistent subjective judgements across different researchers, while also improving analysis efficiency. Automatic analysis procedures are developed for two solidification experiments: an AM simulator experiment and a rapid solidification experiment. The AM simulator was developed at section 32-ID-B of the Advanced Photon Source (APS) synchrotron facility at Argonne National Laboratory [29] to simulate laser powder bed fusion (LPBF): an AM technique in which material is fused together, one layer at a time, using a high-energy laser [28]. That said, the AM simulator may also be used more generally to observe laser-substrate interactions (i.e., a substrate without a powder layer). Hard x-rays and high-speed x-ray detectors are used to image the melting and solidification of Ni-1.9 Mo-6.6 Al (wt.%) single crystals *in situ*, revealing the melt pool such that the S-L interfaces can be identified and tracked. The resulting location information of the S-L interfaces are used to calculate solidification velocities under LPBF-like conditions. The rapid solidification experiments were performed by melting thin films (approximately 100 nm in thickness) of Al-3 wt.% Si on an amorphous silicon nitride substrate and monitoring the solidification using a dynamic transmission electron microscope (DTEM) at Lawrence Livermore National Laboratory. DTEM has proven to be useful in many rapid solidification studies [137–148]. For each analysis procedure performed here, the automated measurements are compared to manual measurements to assess the performance of the procedures.

## 4.2 Methods

This section outlines the methods for performing the two types of experiments presented in this work, developing the procedures to automatically detect the solidifying melt pools as they are observed, and the process for manually identifying the melt pools. The presented procedures are written in the Python programming language and formatted into *Jupyter* notebooks [56]. Using Python with *Jupyter* notebooks is beneficial for both development and presentation. The cell-based nature of *Jupyter* notebook files allow for an iterative workflow for processing and analyzing data while also creating a reproducible procedure in the process. Variables declared in each cell are available to successive cells, allowing for use of the same variables across a notebook, while showing the output of a cell at any point of the procedure rather than at the end only. Since cells can contain formatted text in addition to code, scientific context can be

provided about in addition to technical information about the procedure itself in between code cells, improving readability and reproducibility. Other Python packages used in these procedures are *imageio* for reading and writing of image files [99], *NumPy* for representing the images as numerical arrays and performing fast calculations [98], *scikit-image* for performing image processing algorithms [100], and *napari* for visualizing and annotating the data with an interactive, multi-dimensional image viewer [43].

#### 4.2.1 Ni-Mo-Al Simulated AM

Experiments simulating the processing conditions of LPBF were performed using the AM simulator at sector 32-ID-B at the APS. The simulator consists of an argon-backfilled chamber containing a sample fixture holding a thin metallic plate sample (approximately 100  $\mu\text{m}$  thick) sandwiched between two glassy carbon plates in the path of a polychromatic x-ray beam. A 520 W laser is located above the sample. The experiments are performed by striking the top surface of the metallic sample with the laser, creating a pool of molten metal at the surface. High-speed x-radiography captures the melting and solidification of the sample with a downstream, high-speed detector. An image sequence through time is captured with a spatial resolution of 1.93  $\mu\text{m}$  per pixel, a framerate of 80,000 frames per second, and a field-of-view of 988 by 741  $\mu\text{m}$ . After the laser shuts off, the melted portion of the sample (hereafter referred to as the melt pool) can be seen solidifying based on the density and x-ray absorption differences between the liquid and the solid phases (Figure 4.1).

#### 4.2.2 Simulated AM Detection Procedure

To measure solidification velocities during the AM-like process, the S-L interface must be tracked through the radiograph sequence from the experiment. Once the location is known, the change in location over time yields the solidification velocity. To procedurally identify the S-L interface, the images are processed in a way that highlights the differences between each image and the preceding image in the time sequence. The first step performed is the conversion of all images from 16-bit unsigned integer format to a floating-point image format (Figure 4.2.a). This changes the intensity range from [0, 65536] to [0, 1] to enable floating point calculation and prevent a loss of information from rounding to the nearest integer. Next, a Gaussian filter is applied to each image. This smooths out noise in the images. Each smoothed image is then subtracted from the succeeding image (Figure 4.2.b). The resulting subtracted image visually highlights the moving interface and some varying noise in the images, since it is these features that are

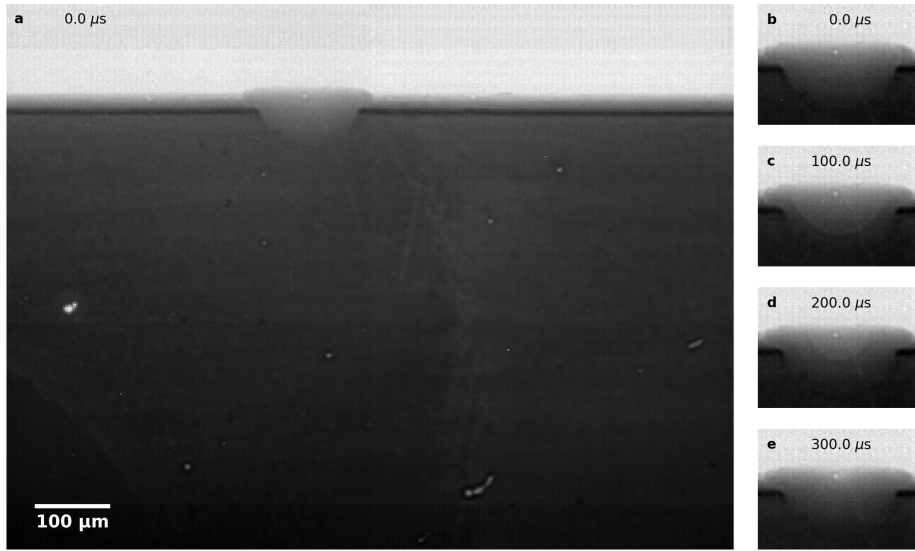


Figure 4.1 Subset of a time sequence of x-radiography depicting the solidification of a Ni-1.9 Mo-6.6 Al (wt.%) single crystal after melting with a laser at 104 W (20% maximum power). (a) Full image of radiograph right after the laser shuts off ( $t = 0 \mu\text{s}$ ). (b) Radiograph from (a) cropped to the melt pool and immediate surroundings ( $t = 0 \mu\text{s}$ ). (c) Cropped radiograph showing partial solidification and visible solid-liquid (S-L) interface ( $t = 100 \mu\text{s}$ ). (d) Cropped radiograph showing further solidification and a smaller S-L interface ( $t = 200 \mu\text{s}$ ). (e) Cropped radiograph showing near total solidification with S-L interface no longer easily visible ( $t = 300 \mu\text{s}$ ).

the areas of greatest difference in the sequence. The intensity of the subtracted image is rescaled by clipping the intensity of the image. This replaces the pixels with intensities in the upper and lower fifth percentile with the intensity value at those cutoffs respectively (Figure 4.2.c). The rescaled images are denoised using a total variation minimization algorithm [149] implemented in *scikit-image* as the function *restoration.denoise\_tv\_chambolle*. This further reduces the intensity of the remaining noisy regions in the image. The image is inverted so the regions corresponding to the S-L interface region are represented by high intensities in the image (Figure 4.2.d). An upper minimum threshold is applied to the inverted image to create a binary image (Figure 4.2.e). A skeletonization algorithm [150] implemented in *scikit-image* as the function *morphology.skeletonize* is used to erode each connected region in the image to one-pixel wide “skeleton” regions in the binary image (Figure 4.2.f).

The area of each skeleton region is analyzed using the function *measure.regionprops* from *scikit-image*. Since each region is one pixel wide, the area corresponds to the total length of the skeleton with each separate branch or “bone” laid end-to-end. For most images in the sequence, the largest skeleton correlates to the S-L interface. This is seen

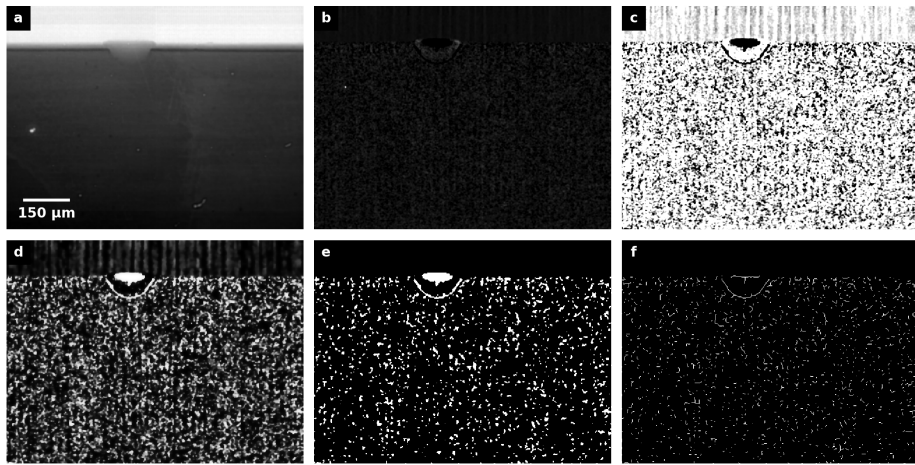


Figure 4.2 The procedural image processing routine for identifying the solid-liquid (S-L) interface for a radiograph taken during the solidification portion of the experiment. (a) Raw radiograph showing the melt pool and S-L interface. (b) Smoothing with a Gaussian filter and subtraction from the succeeding smoothed radiograph in the time sequence. (c) Intensity rescaling by clipping the top and bottom five percent intensities. (d) Denoising and intensity inversion. (e) Upper minimum threshold to convert to binary image. (f) Skeletonization to create one-pixel wide regions.

by overlaying the largest skeleton over the solidifying melt pool radiographs within the first 200  $\mu$ s after the laser shuts off (Figure 4.3).

#### 4.2.3 Simulated AM Manual Measurements

The position of the detected S-L interfaces was compared to manual measurements to assess the performance of the detection procedure. The Python package *napari* enables a graphic user interface (GUI) window to annotate multi-dimensional images, which was used to manually track the interfaces. The sequence of radiographs was opened in a *napari* series of frames segmented from the raw image. A *napari* points layer was also added to the window. This allowed a user to annotate the images with a point denoting the bottom of the interface for each image. This manual annotation was performed three times such that the variance of individual manual measurements could be analyzed and compared to the mean manual measurement along with the detected S-L interface locations.

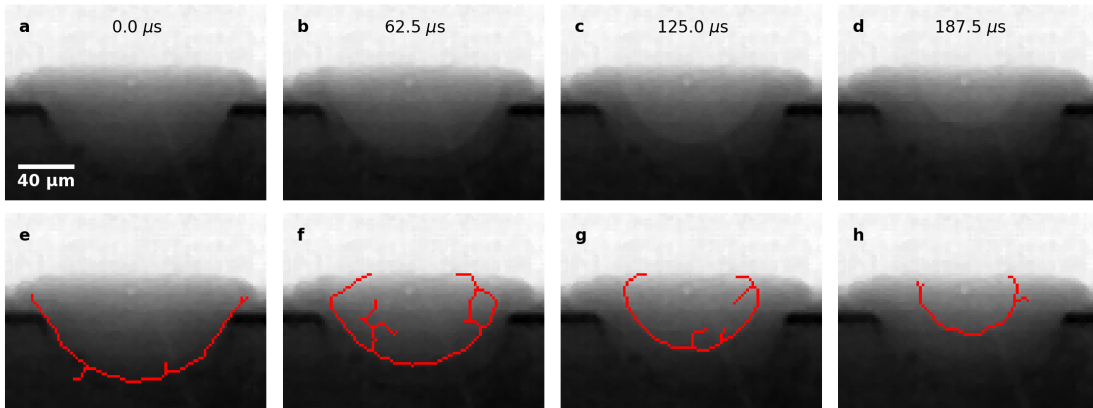


Figure 4.3 (a - d) Subset of radiography sequence, showing the solid-liquid interface receding throughout the experiment. (e - f) Skeletonized regions overlaid in red on subset of radiography sequence, showing the as-detected position of the solid-liquid interface throughout the experiment.

#### 4.2.4 Al-Si Rapid Solidification

To accurately model Al-Si solidification, solidification velocity must first be measured from experiments. Solidification was monitored *in situ* with a Dynamic Transmission Electron Microscope (DTEM). A thin film of Al-3 wt.% Si is deposited on a silicon nitride surface with a thickness of approximately 100 nm. A laser melts the Al-Si film and after a 20  $\mu$ s delay, an electron beam pulsing at 2.5  $\mu$ s intervals is transmitted through the sample. The resulting beam is rastered across a detector, which captures nine frames of the solidification at 120x magnification in a single image (Figure 4.4). An automated identification procedure was developed to calculate the solidification velocity by identifying the rapidly solidifying melt pool in each frame, fitting an ellipse to each of the melt pools, and analyzing the change in size of the ellipses. This procedure consists of a series of Python functions, mostly implemented using a set of packages similar to the packages used in the AM simulator procedure: *imageio*, *NumPy*, *scikit-image*, *matplotlib*, *SciPy*. The functions were executed in *Jupyter* notebooks to yield incremental results at each step for three separate DTEM images depicting rapid solidification of Al-3 wt.% Si.

#### 4.2.5 Rapid Solidification Detection Procedure

The detection procedure consists of four parts: preprocessing, morphologic operations, ellipse fitting, and analysis. In the preprocessing routine, the DTEM image is separated into nine frames by performing a lower minimum threshold to create a binary

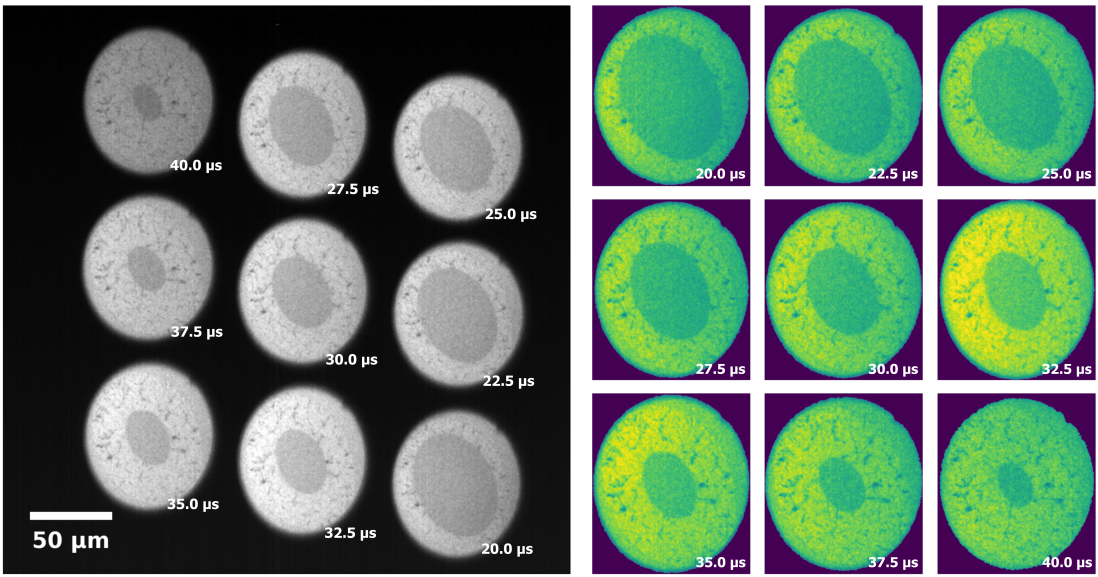


Figure 4.4 (a) Dynamic transmission electron microscope (DTEM) image showing nine frames of a rapidly solidifying Al-3 Si sample with a 20  $\mu\text{s}$  delay and 2.5  $\mu\text{s}$  capture interval. The chronology of the experiment starts with the lower right image, moves up the right column, down the center column, and finally up the left column to end at the top left image. (b) The same image with false color highlighting intensity differences across the image.

image. The binary image contains masks of the nine elliptical frames, which are labeled according to connected pixel region in the image using a *scikit-image*. The labeled image is passed to the *scikit-image* function *measure.regionprops*, which provides information necessary to crop each of the nine frames and center them into nine separate images of matching size. For each of these separated frames, a pseudo-flat-field image is created by smoothing the image with a large Gaussian filter and replacing the background pixels (beyond the elliptical frame) with the mean intensity of the image (Figure 4.5). Each resulting pseudo-flat-field image is used to normalize each frame, smoothing out localized intensity fluctuations. This pseudo-flat-field correction is performed for each of the nine frames (Figure 4.6).

Following the pseudo-flat-field correction, the rescaled frames are then subjected to the morphologic operation stage of the procedure. An upper minimum threshold is used to create a binary image (Figure 4.7.a), on which morphologic opening is performed to sever connections across the melt pool. With regions disconnected, regions smaller than the mean region size are removed from the binary image (Figure 4.7.b), then the image is inverted and regions at the border of the image are removed (Figure 4.7.c). At this point, the largest region is selected (Figure 4.7.d) and morphologic closing is performed

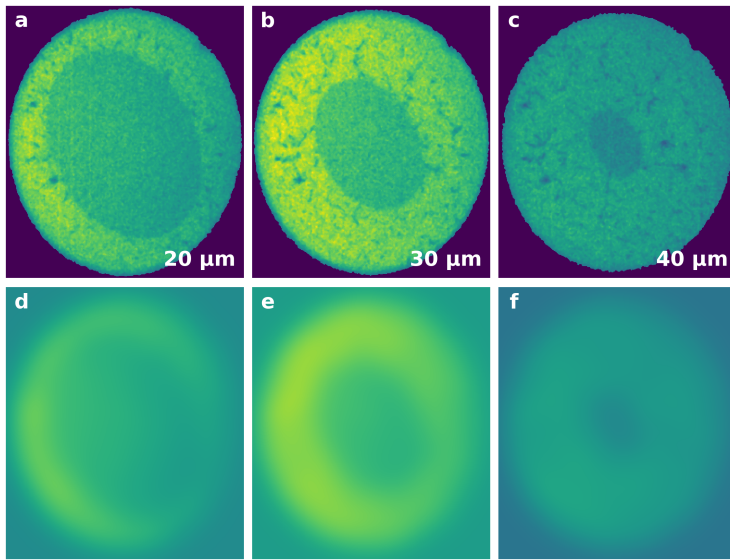


Figure 4.5 (a - c) Subset of frames with intensity unchanged following extraction from full DTEM image. Frames correspond to 20  $\mu\text{s}$ , 30  $\mu\text{s}$ , and 40  $\mu\text{s}$  after the laser melted the sample. (d - f) Pseudo flat-field images created with large-sigma Gaussian filter and mean-filled background. Created from corresponding frames (a - c).

to close any remaining gaps across the area corresponding to the S-L interface (Figure 4.7.e). Finally, all the holes inside the remaining region are filled, to create a single, roughly elliptical shape (Figure 4.7.f).

This routine is performed for each frame, resulting in nine roughly elliptical identified regions. These regions contain the melt pools, though the masks contain artifacts branching off from the elliptical melt pools that correspond to darker features around the edge of the true melt pools (Figure 4.8).

The ellipse fitting stage of the routine takes the identified region for each frame and fits an ellipse to the region. An ellipse with the same second moment as the identified region is calculated with the *scikit-image* function *measure.regionprops* as a first approximation fit. This ellipse is rasterized onto an image of the same size as the and at the same centroid as the identified region. Both the fitted ellipse and the identified region are represented as binary images with pixel intensities of either one or zero, so the mismatch between the two images can be represented by the sum of the pixels shared between the two images. True fit pixels represent the pixels valued one in both images. Misfit pixels represent the pixels valued zero in the identified region but valued one in the fitted ellipse image. Unfit pixels represent the pixels valued one in the identified regions but valued zero in the fitted ellipse image. Each of these types of pixels

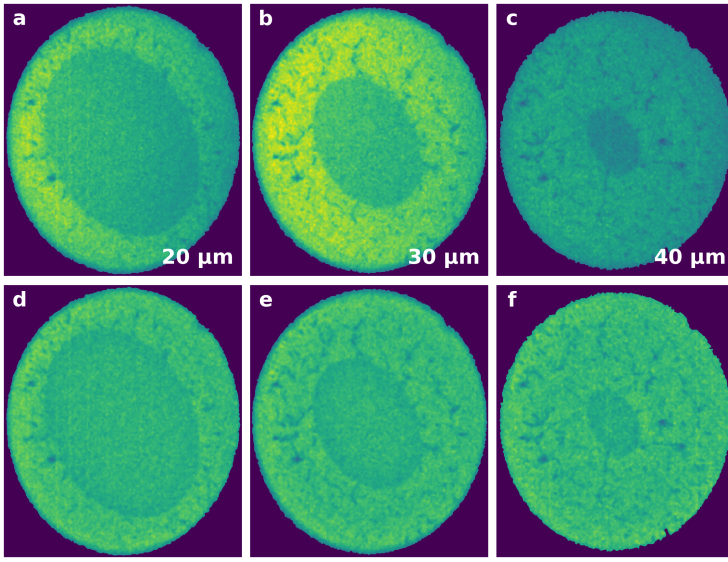


Figure 4.6 Comparison between raw DTEM frames and intensity-rescaled frames following pseudo-flat-field correction. (a - c) Subset of frames with intensity unchanged following extraction from full DTEM image. Frames correspond to 20  $\mu\text{s}$ , 30  $\mu\text{s}$ , and 40  $\mu\text{s}$  after the laser melted the sample. (d - f) Subset of frames following pseudo flat-field images created with large-sigma Gaussian filter and mean-filled background. Created from corresponding frames as (a - c) and pseudo flat-field images (Figure 4.5.d - f).

can be visualized by overlaying the fitted ellipse image on the identified regions and assigning different colors to different pixel types (Figure 4.9).

The ellipse of equal second moment from *scikit-image* (Figure 4.9) is used as a starting point for fit optimization. The parameters defining the ellipse (centroid x-coordinate, centroid y-coordinate, minor radius, major radius, and orientation) are optimized using the downhill simplex algorithm [151] implemented in *SciPy* as the function *optimize.fmin*. This function works by minimizing the value returned by a custom cost function (Equation 4.1) for a frame with  $m$  rows and  $n$  columns:

$$cost = - \left( \sum_{i=0}^m \sum_{j=0}^n T_{ij} \right) \left( \sum_{i=0}^m \sum_{j=0}^n T_{ij} + \sum_{i=0}^m \sum_{j=0}^n M_{ij} + \frac{1}{4} \sum_{i=0}^m \sum_{j=0}^n U_{ij} \right)^{-1} \quad (4.1)$$

where  $T$  represents a true fit pixel within both the identified region and the fitted ellipse,  $M$  represents a misfit pixel beyond the identified region but within the fitted ellipse, and  $U$  represents an unfit pixel beyond the identified region and the fitted ellipse. Including the sum of true fit pixels in the numerator and denominator of the cost function means that a perfect fit would be a cost value of -1. The addition of the sum of the misfit and unfit pixels in the denominator decreases the cost value from -1 for additional pixels that are

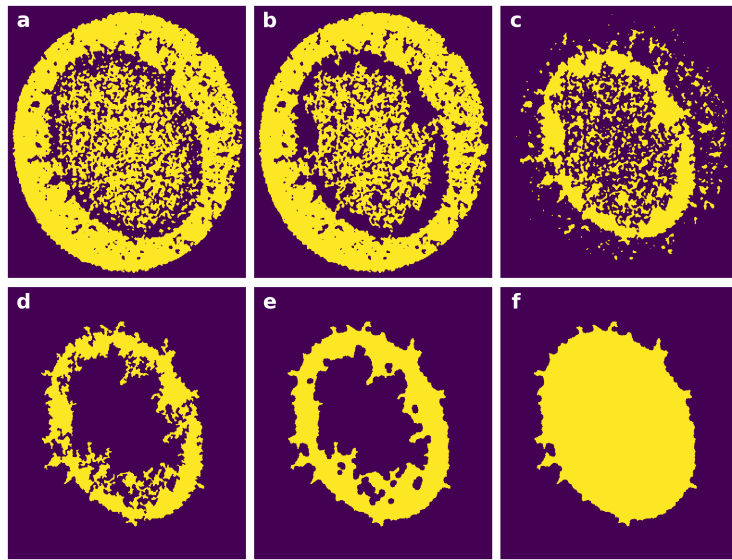


Figure 4.7 Series of morphological operations to automatically mask the liquid region of each solidifying frame from the DTEM image. (a) Upper minimum threshold of  $20 \mu\text{s}$  frame (Figure 4.6.d). (b) Result of morphological opening of (a) to severe small connections across the solid-liquid interface followed by filtering of regions smaller than the mean area of all the regions present. (c) Inversion of b followed by removal of regions connected to the border. (d) Selection of region in (c) with largest area. (e) Morphological closing of (c) to connect small gaps across the solid-liquid interface that were not disconnected in the opening in (b). (f) Filling of all holes to create the final identified region.

mismatched between the fitted ellipse image and the identified region. Since these terms are added to the sum of true fit pixels in the denominator, the effect of each additional mismatched pixel acts relative to the number of true fit pixels. For a frame with larger true fit alignment, each individual mismatched pixel contributes less to the overall cost value than the same mismatched pixel would contribute to a frame with a smaller true fit alignment. The  $\frac{1}{4}$  factor also reduces the contribution of unfit pixels, making true fit and misfit pixels the most important factor in the cost function, and therefore in the optimization process as a whole.

The outputted ellipse parameters returned from the optimization process show an improvement in the fit represented by a decrease in the sum of misfit and unfit pixels (Figure 4.10). It is interesting to note that most of the unfit pixels do not appear to be part of the melt pool, but instead correspond to darker regions of the solidified metal.

The match of the optimized ellipses and the solid-liquid interface of the experiment can be verified visually by plotting these ellipses on top of each frame of the solidifying sample (Figure 4.11).

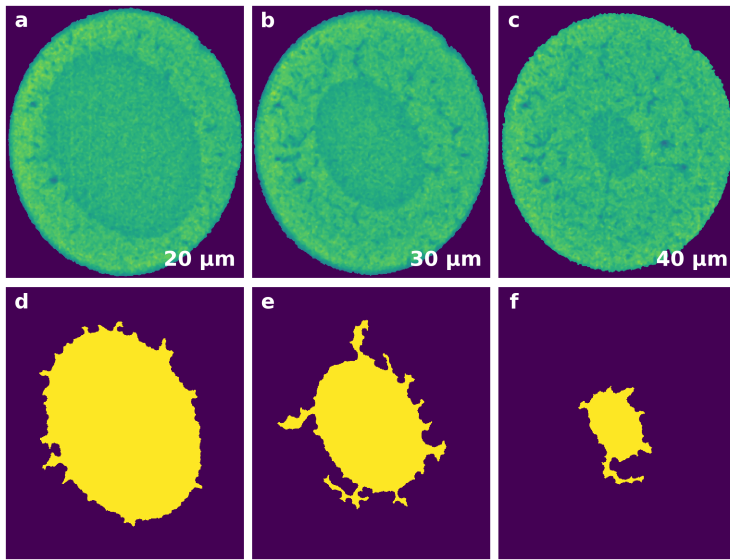


Figure 4.8 (a - c) Subset of normalized frames depicting Al-Si solidification 20  $\mu$ s, 30  $\mu$ s, and 40  $\mu$ s after the laser melted the sample. (d - f) Roughly elliptical identified regions containing the melt pools resulting from the series of morphologic operations (Figure 4.7.a - f) applied to each frame.

#### 4.2.6 Rapid Solidification Manual Measurements

The size of the optimized ellipses is compared to manual detection of the elliptical S-L interfaces. A GUI window from the Python package *napari* was once again used for the manually measurements. The series of frames segmented from the raw DTEM image was opened in a *napari* viewer window along with a points layer. A user placed a point on each side of the long (major) and short (minor) axes of the melt pool. These line segments define the size of the ellipse and was performed three times for the DTEM image such that the variance of individual manual measurements could also be analyzed in addition to the mean manual measurement when assessing the performance of the detected interface sizes.

### 4.3 Results

This section presents the detected and manually-measured solidification velocity results for each of the two type of experiments outlined in the previous section.

#### 4.3.1 Simulated AM Results

The simulated AM S-L interface detection procedure and manual measurement was applied to three separate experiments to test the performance of the procedure. Each

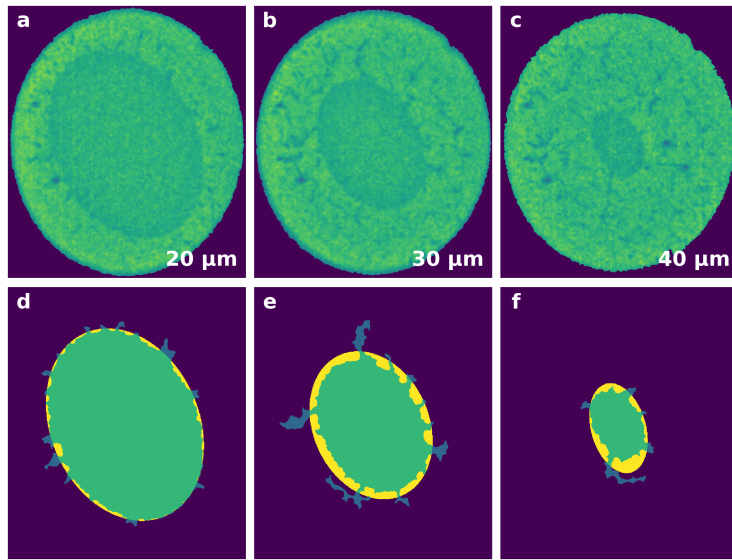


Figure 4.9 (a - c) Subset of normalized frames depicting Al-Si solidification 20  $\mu$ s, 30  $\mu$ s, and 40  $\mu$ s after the laser melted the sample. (d - f) Identified regions overlaid with fitted ellipses generated by finding ellipse parameters that match the centroid and second moment of the identified regions. The color of the pixels show the extent to which the fit matches the identified region. True fit pixels are within both the identified region and the ellipse (green), misfit pixels are beyond the identified region but still within the ellipse (yellow), and unfit pixels are beyond both the identified region and the ellipse (blue).

experiment utilized a different laser power to melt the sample: 104 W (20% maximum power), 156 W (30% maximum power), and 208 W (40% maximum power). In the 104 W experiment, the average velocity of the three manually identified interfaces were calculated to be 0.058, 0.056, and 0.058  $m\ s^{-1}$ , for a collective average velocity of 0.057  $m\ s^{-1}$  and median of 0.057  $m\ s^{-1}$ . The average velocity of the detected interfaces was 0.021  $m\ s^{-1}$ , with a median of 0.041  $m\ s^{-1}$ .

In the 156 W experiment, the average velocity of the three manually identified interfaces were calculated to be 0.046, 0.046, and 0.045  $m\ s^{-1}$ , for a collective average velocity of 0.046  $m\ s^{-1}$  and median of 0.043  $m\ s^{-1}$ . The average velocity of the detected interfaces was 0.022  $m\ s^{-1}$ , with a median of 0.041  $m\ s^{-1}$ .

In the 208 W experiment, the average velocity of the three manually identified interfaces were calculated to be 0.057, 0.058, and 0.056  $m\ s^{-1}$ , for a collective average velocity of 0.057  $m\ s^{-1}$  and median of 0.051  $m\ s^{-1}$ . The average velocity of the detected interfaces was 0.057  $m\ s^{-1}$ , with a median of 0.041  $m\ s^{-1}$ .

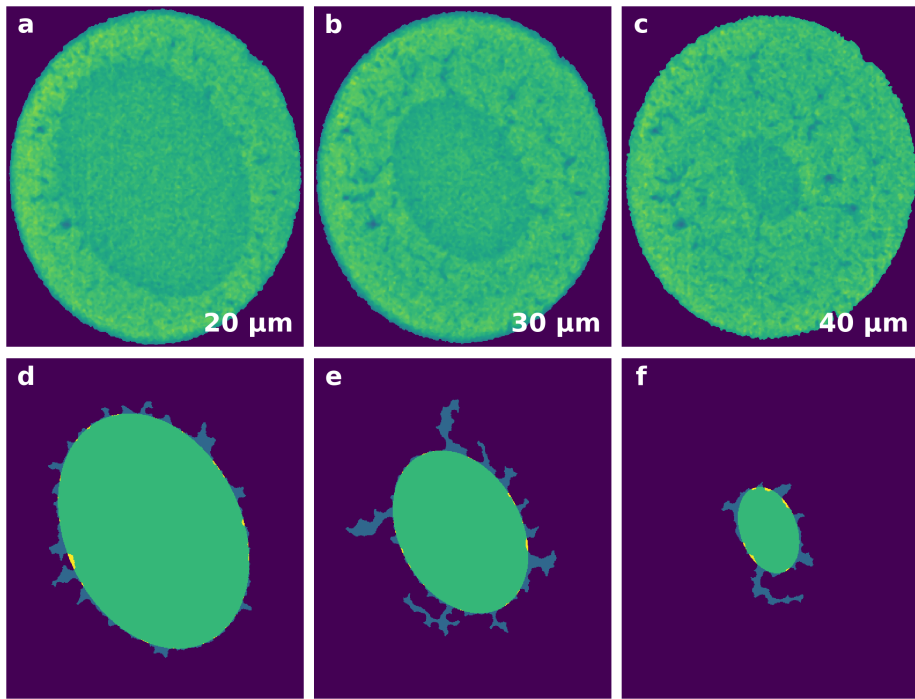


Figure 4.10 (a - c) Subset of normalized frames depicting Al-Si solidification 20  $\mu$ s, 30  $\mu$ s, and 40  $\mu$ s after the laser melted the sample. (d - f) Identified regions overlaid with ellipses of optimized fit. Optimization maximizes true fit match (green) and minimizes misfit match (yellow) and unfit match (blue). The starting point of the optimization are the ellipses of matching centroid and second moment (Figure 4.9. d - f).

#### 4.3.2 Rapid Solidification Results

The rapid solidification detection procedure and manual annotations are performed on the data from three separate rapid solidification experiments. For each of these experiments, the mean and median velocity was calculated for the major and minor axis lengths of the manually-measured and detected ellipses. In the first experiment, the average solidification velocities of the three manually identified elliptical melt pools were calculated for the major / minor axes as  $2.164 \text{ m s}^{-1}$  /  $1.654 \text{ m s}^{-1}$ ,  $2.213 \text{ m s}^{-1}$  /  $1.690 \text{ m s}^{-1}$ , and  $2.172 \text{ m s}^{-1}$  /  $1.620 \text{ m s}^{-1}$ . The average major/minor axis velocities across all three measurements was  $2.183 \text{ m s}^{-1}$  /  $1.655 \text{ m s}^{-1}$  with medians of  $2.167/1.580 \text{ m s}^{-1}$ .

In the second experiment, the average solidification velocities of the three manually identified elliptical melt pools were calculated for the major / minor axes as  $2.268 \text{ m s}^{-1}$  /  $1.675 \text{ m s}^{-1}$ ,  $2.245 \text{ m s}^{-1}$  /  $1.773 \text{ m s}^{-1}$ , and  $2.234 \text{ m s}^{-1}$  /  $1.726 \text{ m s}^{-1}$ . The average major / minor axis velocities across all three measurements were  $2.249 \text{ m s}^{-1}$  /  $1.725 \text{ m s}^{-1}$  with medians of  $2.318/1.688 \text{ m s}^{-1}$ .

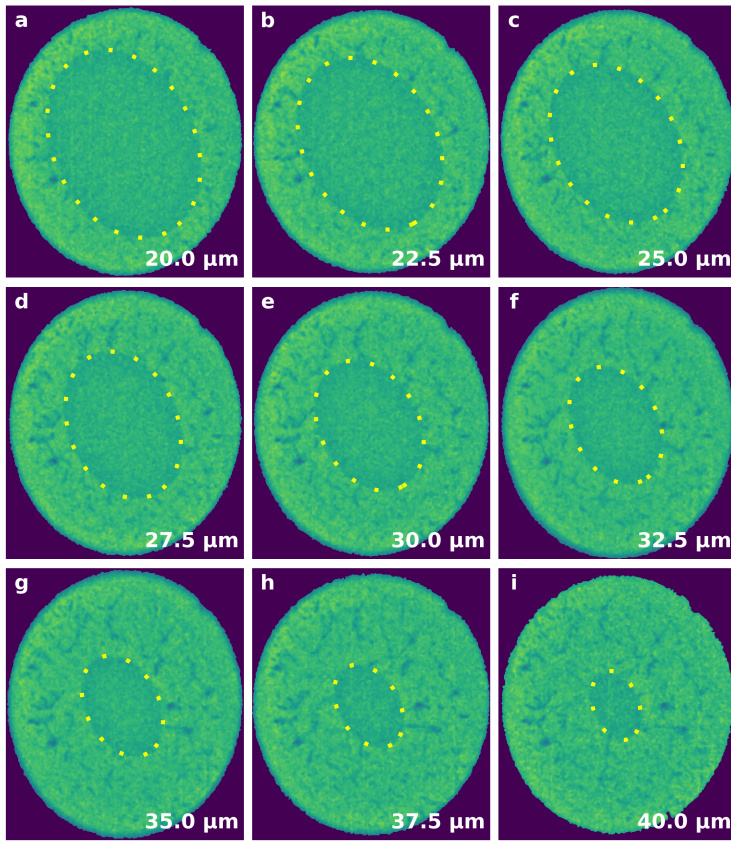


Figure 4.11 Optimized fitted ellipses overlaid on each rescaled frame as yellow dashed lines.

In the third experiment, the average solidification velocities of the three manually identified elliptical melt pools were calculated for the major/minor axes as  $2.665 \text{ m s}^{-1}$  /  $1.824 \text{ m s}^{-1}$ ,  $2.651 \text{ m s}^{-1}$  /  $1.871 \text{ m s}^{-1}$ , and  $2.602 \text{ m s}^{-1}$  /  $1.865 \text{ m s}^{-1}$ . The average major/minor axis velocities across all three measurements were  $2.640 \text{ m s}^{-1}$  /  $1.853 \text{ m s}^{-1}$  with medians of  $2.561 \text{ m s}^{-1}$  /  $1.856 \text{ m s}^{-1}$ .

## 4.4 Discussion

This section discusses the detected and manually-measured solidification velocity results for each of the two type of experiments outlined in the previous section.

### 4.4.1 AM Simulator

Rather than relying on the mean and median velocities to assess the AM simulator detection procedure, the deviations from the mean manual velocity were analyzed for each individual manual measurement and for the detected velocities. This was repeated

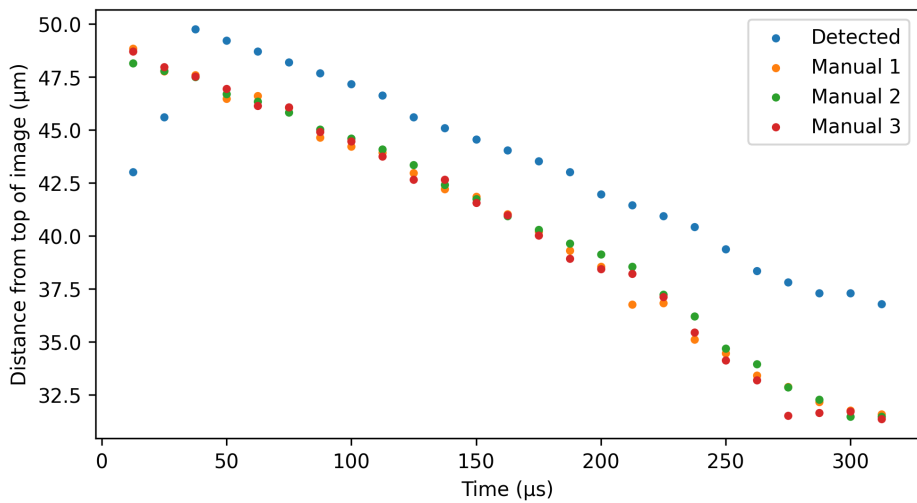


Figure 4.12 Interfaces detected by the automated procedure (blue) compared with manually identified interfaces (orange, green, and red) for the 104 W experiment. Interface location is defined by the distance from the bottom of the solid-liquid interface to top of the image, starting when the laser shuts off ( $t = 0 \mu\text{s}$ ).

for each of the three experiments to quantify the variance of the velocity as a way to quantitatively compare the automated procedure to the manual measurements. In the 104 W experiment, the mean velocities differ drastically ( $0.021 \text{ m s}^{-1}$  detected,  $0.057 \text{ m s}^{-1}$  manual), but less so across the median values ( $0.041 \text{ m s}^{-1}$  detected,  $0.043 \text{ m s}^{-1}$  manual), suggesting there are outliers in the detected data that are skewing the mean. This is further supported by analyzing the average deviations from the manual mean velocity (in terms of percent of the manual mean: 78.800% detected, 48.492% manual). The average deviations differ much like the mean velocities, however when considering the spread of these deviations throughout the experiment, 58.333% of the manually measured velocities have a deviation lower than the average manual deviation, whereas 87.5% of the detected deviations are lower than the same value. This indicates that the detected outliers are farther from the manual mean than any of the individual manual measurements, which is exemplified in Figure 4.12 by the large change in position (corresponding to a high velocity) across the first three frames, compared to the more gradual change throughout the rest of the experiment. This is especially interesting because the overall detected interface position seems to be consistently about  $2.5 \mu\text{m}$  higher than the manually measured position. Since the interface still appears to be moving at a rate similar to the manual measurements, this position discrepancy could be caused by the detection procedure capturing an optical artifact slightly above the interface that nonetheless moved at the same rate.

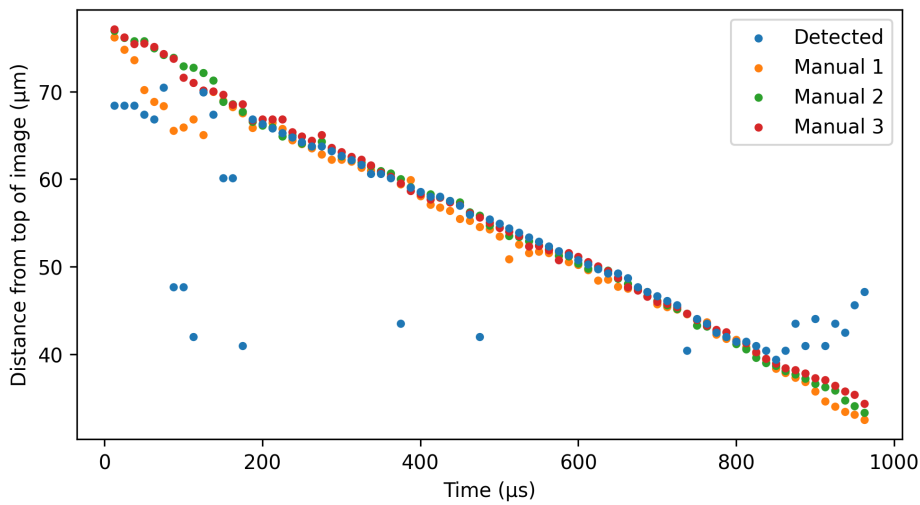


Figure 4.13 Interfaces detected by the automated procedure (blue) compared with manually identified interfaces (orange, green, and red) for the 156 W experiment. Interface location is defined by the distance from the bottom of the solid-liquid interface to top of the image, starting when the laser shuts off ( $t = 0 \mu\text{s}$ ).

In the 156 W experiment, the average velocities differ drastically ( $0.022 \text{ m s}^{-1}$  detected,  $0.046 \text{ m s}^{-1}$  manual) but similar to experiment 104 W less so across the median values ( $0.041 \text{ m s}^{-1}$  detected,  $0.043 \text{ m s}^{-1}$  manual). The detected deviation from the manual mean velocity is once again much larger than the manual deviation (in terms of percent of the manual mean: 496.037% detected, 69.798% manual). Considering the spread of these deviations yields slightly different results in that 65.789% of the manually measured velocities have a deviation lower than the average manual deviation compared to the only 50.0% of detected deviations. However, these 50.0% of detected deviations are also lower than half of the average manual deviation. The outliers of the detected velocity may be further from the manual mean than the manual measurements, but the fraction of the data that are within the average manual deviation are much closer to the average than any of the individual manual measurements. This can be seen in Figure 4.13 by the outliers of the detected positions located farther away from the cluster of other data while the detected positions closer to the rest of the data vary less across the frames than the manual measurements. It is also worth noting that both the detected and manual interface positions appear to be the most uncertain at the beginning and end of the experiment, suggesting that the interface was harder to make out than in the 104 W experiment, also supported by the fact that the average manual deviation was higher for this experiment.

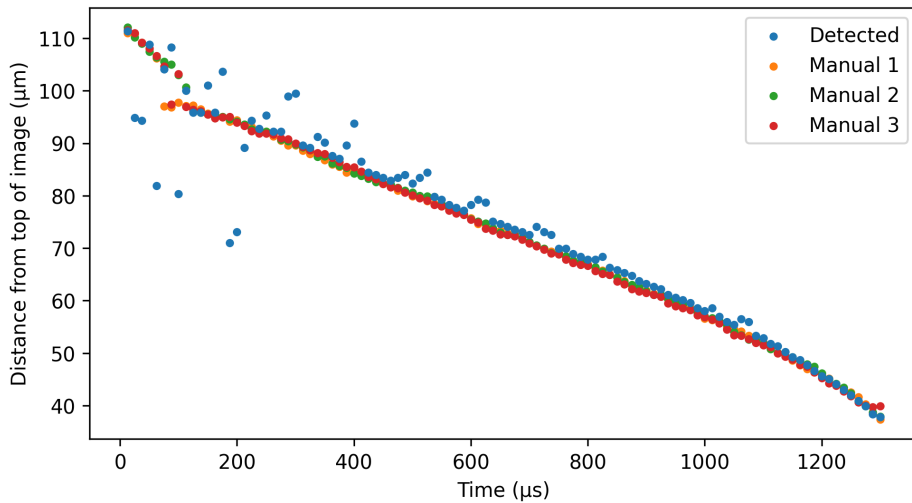


Figure 4.14 Interfaces detected by the automated procedure (blue) compared with manually identified interfaces (orange, green, and red) for the 208 W experiment. Interface location is defined by the distance from the bottom of the solid-liquid interface to top of the image, starting when the laser shuts off ( $t = 0 \mu\text{s}$ ).

In the 208 W experiment, the mean velocities are the same ( $0.057 \text{ m s}^{-1}$  detected,  $0.057 \text{ m s}^{-1}$  manual). However, the median values still differed ( $0.041 \text{ m s}^{-1}$  detected,  $0.052 \text{ m s}^{-1}$  manual), so the matching means is most likely an effect of the deviations balanced on either side of the mean. Similar to the 156 W experiment, the detected deviations from the manual mean velocity are much higher than the manual measurements (in terms of percent of the manual mean: 415.305% detected, 56.777% manual). Much like the previous experiments, the outliers of the detected velocities are much farther out from the rest of the data than the manually measured velocities the experiment. 52.427% of detected data has a deviation less than the average manual deviation which is less than the 77.670% of the manually measured velocities, but still comparable. Comparing the data that deviates within half the average manual deviation is even more similar at 33.981% of the detected velocities and 28.155% of the manually measured velocities. Figure 4.14 shows the higher deviation of the detected data far out from the mean like the previous experiments, but a notable difference is that there appears to be a cusp in the manually measured interface positions around  $100 \mu\text{s}$ . This could be due to a change in velocity of the S-L interface, but was more likely due to a secondary interface that can appear in these experiments when a melt pool becomes large enough to breach the edge of the sample. If the sample breach happens at a different height than the minima of the melt pool, the breach can appear to be a secondary interface. In this case, the breach may have been more visible than the

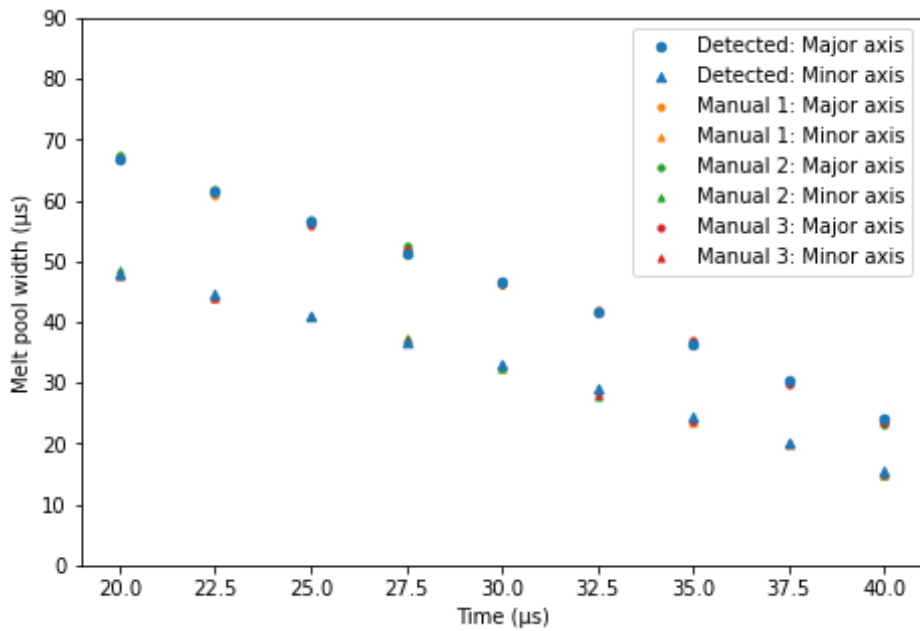


Figure 4.15 Size of melt pools over time throughout the third rapid solidification experiment. The detected ellipses (blue) have a low deviation from the manually measured interfaces (orange, green, and red).

minima of the interface at the beginning of the experiment. The first 100 - 200  $\mu\text{s}$  of the experiment is also where the detected position deviates from the mean the most. As a side note, it is not entirely a coincidence that the median velocity was the same for all three experiments, as that value ( $0.041 \text{ m s}^{-1}$ ) corresponds to the 1 pixel/frame after converting pixels to  $\mu\text{m}$  with the spatial resolution and frame number to  $\mu\text{s}$  with the experiment framerate.

#### 4.4.2 Rapid Solidification

To assess the performance of the rapid solidification detection procedure, the deviations from the mean manual velocity were analyzed for the major and minor axes of the melt pools as determined from each individual manual measurement and for the detected procedure. This analysis was repeated for each of the three DTEM experiments to characterize the performance of the procedure compared to manual measurement. In the first experiment, the mean major / minor axis velocities are similar ( $2.124 \text{ m s}^{-1}$  /  $1.619 \text{ m s}^{-1}$  detected,  $2.183 \text{ m s}^{-1}$  /  $1.655 \text{ m s}^{-1}$  manual), and so are the median velocities ( $2.167 \text{ m s}^{-1}$  /  $1.580 \text{ m s}^{-1}$  detected,  $2.101 \text{ m s}^{-1}$  /  $1.679 \text{ m s}^{-1}$  manual). The proximity of the mean to the medians for both the detected and manually measured

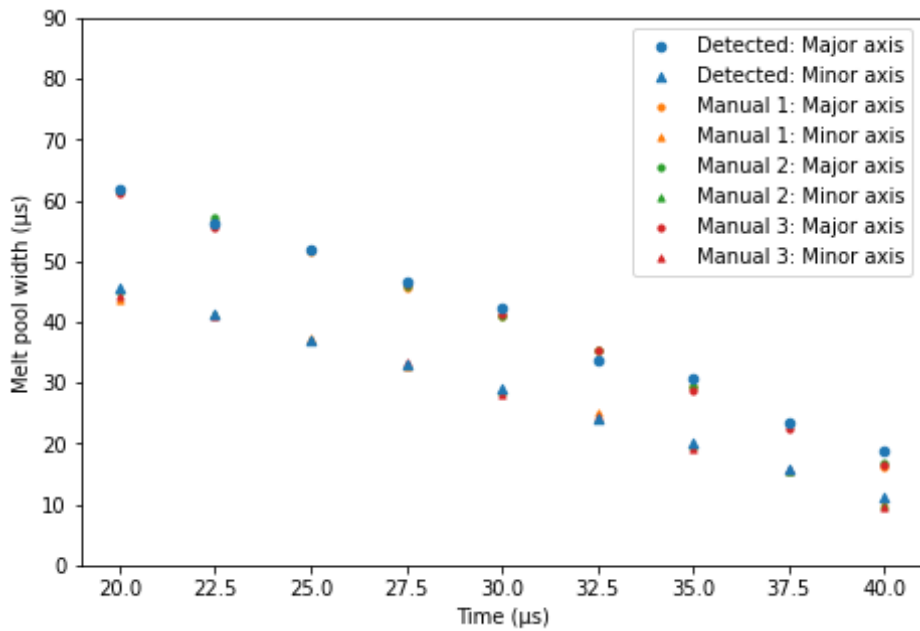


Figure 4.16 Size of melt pools over time throughout the third rapid solidification experiment. The detected ellipses (blue) have a low deviation from the manually measured interfaces (orange, green, and red).

velocities suggests a small spread of the data, which is supported by a lower deviation from the manual mean velocity (in terms of percent of the manual mean for the major / minor axes: 7.9% / 9.476% detected, 13.543% / 14.876% manual). The data is distributed closely enough that it is difficult to make out differences between the detected and manual data in the plotted positions (Figure 4.15).

In the second rapid solidification experiment, the mean major / minor axis velocities are also similar ( $2.148 \text{ m s}^{-1}$  /  $1.719 \text{ m s}^{-1}$  detected,  $2.249 \text{ m s}^{-1}$  /  $1.725 \text{ m s}^{-1}$  manual), as are the median velocities ( $2.028 \text{ m s}^{-1}$  /  $1.730 \text{ m s}^{-1}$  detected,  $2.318 \text{ m s}^{-1}$  /  $1.688 \text{ m s}^{-1}$  manual). The deviation from the manual mean velocity is also low (in terms of percent of the manual mean for the major / minor axes: 24.001% / 6.248% detected, 10.331% / 15.954% manual), however the deviation of the manual measurements is slightly larger, as can be seen by some outliers in the the position data (Figure 4.16).

In the third rapid solidification experiment, the mean major / minor axis velocities are ( $1.893 \text{ m s}^{-1}$  /  $1.628 \text{ m s}^{-1}$  detected,  $2.640 \text{ m s}^{-1}$  /  $1.853 \text{ m s}^{-1}$  manual), and the median velocities ( $2.494 \text{ m s}^{-1}$  /  $1.683 \text{ m s}^{-1}$  detected,  $2.561 \text{ m s}^{-1}$  /  $1.856 \text{ m s}^{-1}$  manual). The detected procedure had a larger deviation from the manual measurements than in either of the two previous experiments. The deviations from the manual mean velocity are much higher (in terms of percent of the manual mean for the major / minor axes:

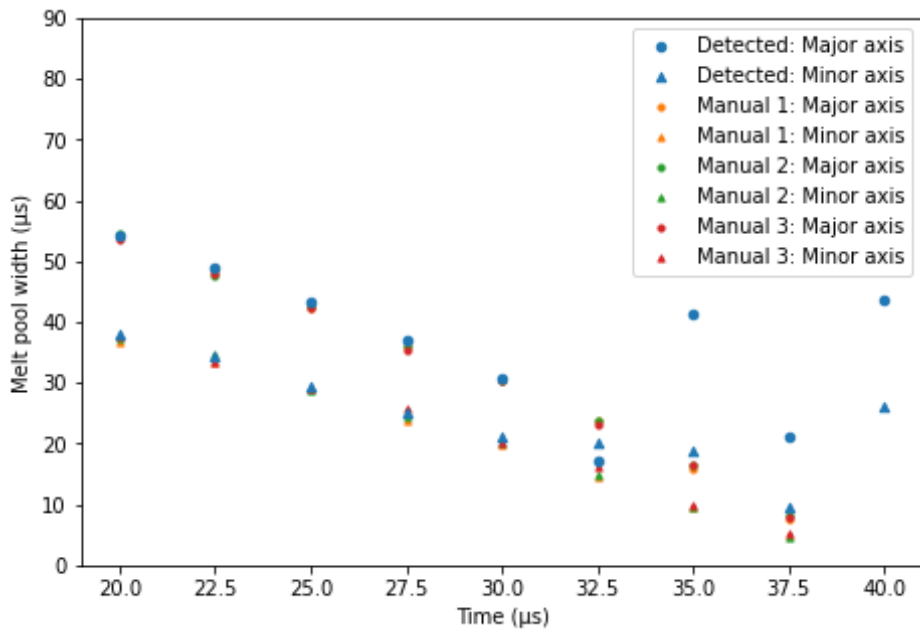


Figure 4.17 Size of melt pools over time throughout the third rapid solidification experiment. The detected ellipses (blue) have a low deviation from the manually measured interfaces (orange, green, and red) until the end of the experiment.

119.014% / 42.621% detected, 13.365% / 14.290% manual). It is worth noting that in this experiment, the manual measurements only recorded eight frames in which the elliptical melt pool was manually measured because the sample completely solidified before the last frame. As can be seen in the position data, the detected melt pool size deviates more from the manual measurements at the end of the experiment (Figure 4.17). This suggests the detection procedure is less effective when the melt pool is near closing, most likely because the shape of the melt pool is lost within the noise of the image.

## 4.5 Conclusions

Methods for calculating solidification velocities are important for accurately predicting microstructures in AM-like processes and linking those microstructures to processing parameters. Characterization tools like synchrotron x-radiography and DTEM enable high spatial and temporal resolution in-situ monitoring of solidification, but the large amounts of data these techniques yield require difficult manual analysis to retrieve quantitative information like solidification velocities. Tracking and annotating image data manually introduces human bias and error that can be inconsistent across measurements and users. Reasons for these inconsistencies include subjective

judgement calls, personal preferences, miscommunications, and user fatigue. These sources of error in measurements can be difficult, and in some cases nearly impossible, to quantify. The automated detection techniques presented in this work explored the possibility of a consistent method of analyzing image data from solidification experiments, while also reducing the effect of bias on the collected data. Two procedures were presented in this work for automating the detection of S-L interfaces and calculating solidification velocities, and each procedure was applied to three separate experiments. The first procedure determined S-L interface positions in synchrotron x-radiography images from simulated AM experiments. The second procedure automated the detection of S-L interfaces for frames in three separate DTEM images depicting thin film rapid solidification. Each procedure was similar but each took a slightly different approach to interface detection.

The simulated AM procedure performed adequately as compared to manual measurements. The detection procedure returned drastically different mean velocities from the manual measurements for the 104 W and 156 W experiments, however the median detected and manual velocities are similar, suggesting that the differing means are because of outliers in the velocity, which is supported by the significantly higher detected deviation from the manual mean velocity compared with the manual deviation from the manual mean velocity. In the 208 W experiment, the detected mean velocity is the same as the manual velocity, but the median velocities differed. Similar to the 104 W and 156 W experiments, the detected deviation from the manual mean is much higher than the manual deviation. This suggests that the 208 W experiment has a similar problem with the outliers, but that the outlying detected velocities are more evenly distributed both above and below the manual mean velocity.

The rapid solidification procedure performed well as compared to the manual measurements. For the first and second experiments, the mean and median values are both similar with low deviations from the manual mean velocity. In the third experiment, the detected mean velocity differs more than either of the previous two experiments, but the median values are still similar. The detected deviation from the manual mean is also higher in this experiment. Upon closer analysis, the detected velocity has the highest deviation from the manual mean velocity towards the end of the experiment. This is significant because the third experiment fully solidified before the other two experiments. The melt pool does not even show up in the final frame. This suggests the procedure does best when the melt pool is larger and more distinguishable from noise.

The simulated AM procedure did not include any kind of a fit optimization step. The rapid solidification procedure, which did optimize the fit of the detected melt pool, was

more successful in matching the manually measured velocities. If a similar optimization step could be included in the simulated AM procedure, there may be an increase in detection accuracy. In addition, the fitting of the interfaces to parameterized shapes would allow the solidification velocity to be calculated at multiple points along the interfaces. This is not currently possible since the procedure measures the location of the interface based on the bottom of the interface, thus only allowing for the vertical solidification velocity to be calculated.

While this work doesn't claim that these data extraction and analysis methods remove human biases altogether (the procedures were written by a human, after all), a procedure deterministically run by a computer makes the method of extracting data more consistent. The nature of the procedure development may also prompt researchers to more carefully consider biases introduced through their methods. Each step in the procedure must be actively considered to be incorporated, whereas unconscious passivity is possible in manual actions performed in a repetitive manner. The less laborious effect of automated procedures may also benefit researchers by allowing them to more quickly and easily test the effects of small changes to data extraction and analysis, as opposed to the significant time and effort to reproduce changes to manual routines. This reduced barrier to iteration could encourage researchers to test a larger number of iterations data extraction methods, potentially even resulting in more refined results.

## 4.6 Acknowledgements

A special thanks to the beamline scientists at the Advanced Photon Source that make themselves available at odd hours to keep experiments at the facility running smoothly and to the students of the Center for Advanced Non-Ferrous Structural Alloys that agreed to work all the other odd hours to run the experiments and collect the simulated AM data.

# CHAPTER 5

## IMPLEMENTING EDGE STRENGTH CORRECTIONS TO IMPROVE SEGMENTATION OF IRREGULARLY-SHAPED, MULTI-SIZED, AND TIGHTLY-CLUSTERED PARTICLES

Watershed segmentation algorithms are useful tools to separate features in an image from one another, enabling more targeted analyses. However, these algorithms often do not achieve expected results for multi-sized or irregularly-shaped particles, or particles clustered tightly together without strongly defined edges along contact surfaces. This chapter presents an image processing procedure implemented in Python (with libraries including *scikit-image*, *imageio*, *NumPy*, and *SciPy*) to improve the results of a watershed segmentation algorithm. The proposed procedure involves application of a preprocessing routine and custom algorithm which utilizes Delaunay triangulation to merge segmented regions based on edge strength between the regions. The resulting merged-region segmentation results are calculated to more closely match a manual segmentation than a typical watershed segmentation on its own. The procedure is tested on a 2D radiograph sliced from a 3D x-ray computed tomography (XCT) dataset depicting irregularly-shaped and multi-sized sand grains that are tightly clustered with a polymer binder.

### 5.1 Introduction

Image segmentation often plays a crucial role in digital image processing workflows. Segmentation enables the extraction of quantitative information from images that is only qualitatively available through visually analysis alone. Segmentation can be split into two categories: semantic segmentation and instance segmentation. In semantic segmentation, an image is separated, or segmented, into classes for analysis, often the regions of interest (the foreground) and the background. The result of this type of segmentation is a binary image, so this process can be referred to as binarization. A simple way to binarize an image is by selecting a threshold value such that pixels with an intensity above this value are categorized as one of the binary labels, while the pixels with an intensity below the thresholding value are categorized as the second label. The threshold value is often selected manually, but an algorithm can also be used to calculate this value. A useful and well-known thresholding algorithm is Otsu's method [44], which computes an optimal threshold value by analyzing the image histogram. The histogram

is split into classes at different values, and a “goodness” factor, defined by considering within-class and between-class variances, is optimized to determine the threshold value.

The second type of segmentation, instance segmentation, is used to separate specific instances of a class within an image. Instance segmentation can separate features within the foreground from one another to enable analyses including feature locations, sizes, and shapes. In some cases, it may be possible to separate multiple objects based on gray value alone by setting multiple threshold values, however instance segmentation can also be performed by analyzing the morphology of a semantic segmentation. One such method involves morphological watersheds, and is typically referred to as watershed segmentation [45–47, 152, 153]. Watershed segmentation algorithms take their name from the analogy of “flooding” an image by interpreting each intensity value as a height, as if the image is describing a topographic surface. When a flooding operation is performed algorithmically, the local minima of the image act as “catchment basins” which fill until a flood reaches a neighboring flood, at which point a “dam” is created to prevent the floods from merging. After this process is completed, the lines representing the dams remain, thus segmenting the image. As most images wouldn’t appear to represent a logical three-dimensional surface, a transformation of some kind is often applied before watershed segmentation. This can be done using the Euclidean distance transformation, which maps each foreground pixel of a binary image to an intensity representing the distance to the nearest background pixel [154]. Distance transformations are usually inverted before applying a watershed segmentation algorithm so the pixels farthest away from the background (local maxima) will be converted to local minima that will be filled first by the flooding simulation.

Watershed segmentation algorithms can operate by providing a list of markers which seed the catchment basins used in the algorithm [49, 50]. These markers provide locations to begin algorithmic flooding at the same time, regardless of the pixel intensities (“heights”) of these locations. Markers can thus be thought of as “pour points.” This can be useful to control over-segmentation (more segmented regions than expected) and under-segmentation (fewer segmented regions than expected) because in marker-defined watershed segmentation, the number of markers determines the number of catchment basins and therefore the number of final segmented regions. The limitations of segmenting an image via watershed algorithm are often related to the method employed to define the markers. A common method of generating markers is to calculate the minima of the inverse distance transformation. However, this can lead to spurious local minima for irregularly shaped and/or clustered particles, resulting in over-segmentation [26]. In these cases, rather than calculate all local minima,  $h$ -minima

can be calculated such that each minima is a value  $h$  above any surrounding minima [52, 155].

A downside to using  $h$ -minima for marker generation is that this can suppress legitimate minima corresponding to smaller particles when a variety of particle sizes are present. This has been addressed with an adaptive  $h$ -minima method for selecting watershed markers [54]. This method uses dynamic  $h$  values determined by setting a lower and upper  $h$  value for the intensity range of the image. For an inverse distance transform, the  $h$  value range is set such that minima with lower intensities (i.e., points farther from edges) have a higher  $h$  value than minima with higher intensities (i.e., points closer to edges). This translates to allowing minima to be selected that are closer together around small objects in the image but farther apart around larger objects. Another method is to remove minima within a set radius determined by the comparison of intensities between each minima and the surrounding minima [26]. This is based on the assumption that spurious minima are caused by irregularly-shaped or overlapping objects. Rather than suppress markers before seeding a watershed algorithm, another method addresses over-segmentation by detecting strong edges using the Canny edge filter and merging segmented regions if the shared boundary does not exist on an edge, as long as the edge is strongly defined [53, 156].

## 5.2 Methods

A typical watershed segmentation is performed to determine if a difficult segmentation can take advantage of one of the previously mentioned marker generating methods, based on whether segmenting based on distance transform maxima results in over- or under-segmentation. In a typical watershed segmentation routine, an image is semantically segmented and represented as a binary image, the binary image undergoes a distance transformation, and the maxima of the distance transformation is used to generate markers to seed the watershed segmentation. This type of routine is tested with an image of sand grains to see if the resulting segmentation meets expectations for an image of irregularly-shaped, multi-sized, and tightly-clustered sand grains (Figure 5.1.a). This image is loaded from file using the Python package *imageio* and converted to a *NumPy* array [98, 99]. As an array, the image is binarized using the Otsu thresholding algorithm implemented in *scikit-image* (Figure 5.1.b) [44, 100].

After creating the binary image, a series of markers are generated which will be used to seed the watershed segmentation. The distance of each foreground pixel to the nearest background pixel calculated using the Euclidean distance transformation implemented in *SciPy* [157]. This distance transformation is inverted to pass to the

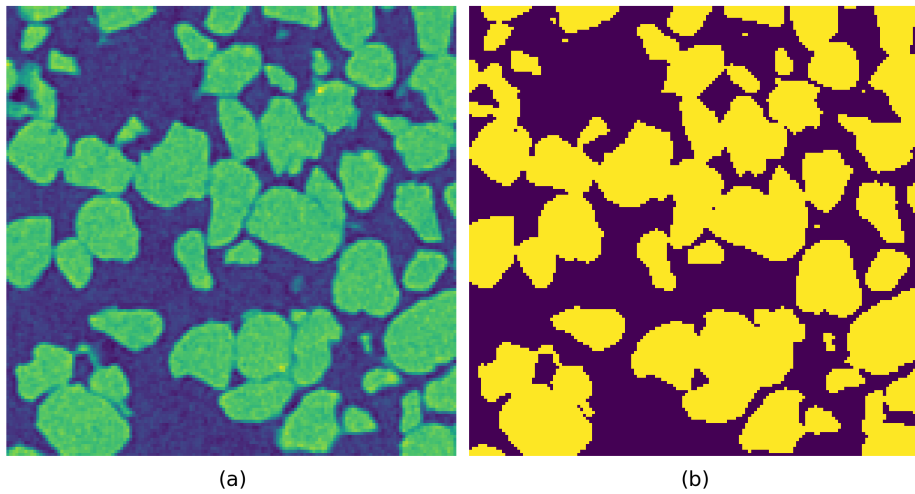


Figure 5.1 (a) Raw image depicting sand particles sliced from a 3D CT scan. (b) Binary image created from the raw image with Otsu thresholding. Yellow regions represent foreground pixels (valued one) while purple regions represent background pixels (valued zero).

watershed algorithm. The local maxima of this distance transform (equivalent to the local minima of the inverted distance transformation) correspond to the points farthest from the edges of the binary image (Figure 5.2.b). In the case of some of the oblong particles present in the image, detecting all the local minima resulted in connected groups of redundant minima where multiple neighboring pixels exist at the same distance from the edge of the binary image. This was addressed by using the *scikit-image* functions *label* and *regionprops* to retain only the centermost point of connected minima. Once disconnected and non-redundant minima were obtained, these points were used as markers to seed a watershed algorithm implemented in *scikit-image*. The resulting segmented regions (Figure 5.2.c) do not meet expectations based on the visually discernible particles in the original image. Since the segmented regions are over-segmented in some places and under-segmented in others, the methods from literature outlined previously cannot correct the segmentation.

### 5.2.1 Adding a Preprocessing Routine to Generate New Markers

To achieve segmentation results that align more closely with expectations, the strategy of the procedure outlined in this work is to first create a set of markers to intentionally over-segment the image, followed by a subsequent step of determining region neighbors and correcting the over-segmentation by merging neighboring regions according to edge strength. This will ensure there is not a combination of over- and

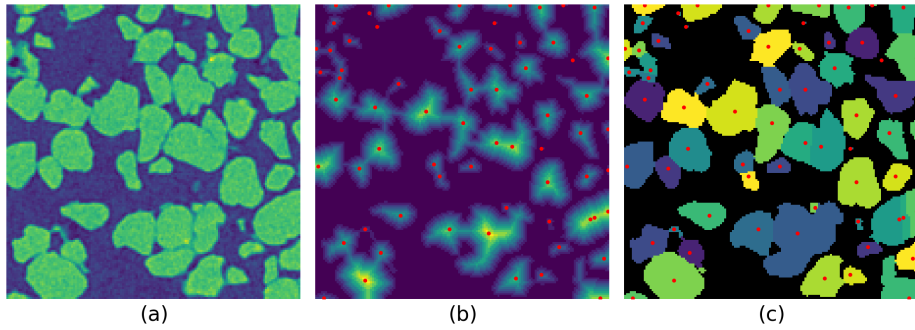


Figure 5.2 (a) Image depicting sand particles sliced from a 3D CT scan. (b) Euclidean distance transformation of Otsu-binarized image (Figure 5.1.b) with local maxima denoted by red points. (c) Watershed segmentation of inverted Euclidean distance transformation seeded by local minima of the inverted distance transformation (red points).

under-segmentation occurring. New markers are needed to achieve this over-segmentation such that each particle in the original image contains at least one marker to prevent under-segmentation. A preprocessing routine is employed to generate these markers. The original image is rescaled between the 5th and 95th percentiles (Figure 5.3.b). Histogram equalization from *scikit-image* is performed on the rescaled image to enhance the intensities of the maxima within the particles (Figure 5.3.c). Histogram equalization spreads out the values of the image across the entire range, allowing for the creation of a binary image that contains only the innermost regions of the particles. To create this binary image, the multiple-class functionality of Otsu's method implemented in *scikit-image* is used to separate the image into three classes. This can be visualized as a ternary image (Figure 5.3.d), however only the regions above the uppermost threshold value are selected to create the binary image. Holes within the created regions are filled using the function *binary\_fill\_holes* from the multidimensional image processing submodule in *SciPy* (Figure 5.3.e). This maximizes the distances calculated via distance transformation operating on the multi-Otsu binary image (Figure 5.3.f). The local maxima of this distance transformation are useful for this routine because they over-represent the particles in the image (i.e., more markers than particles), which will result in the over-segmentation desired at this stage of the procedure.

### 5.2.2 Preparing Over-Segmentation

Before the local maxima markers are used to seed a watershed segmentation, the markers are filtered such that any points close to a particle edge in the image are

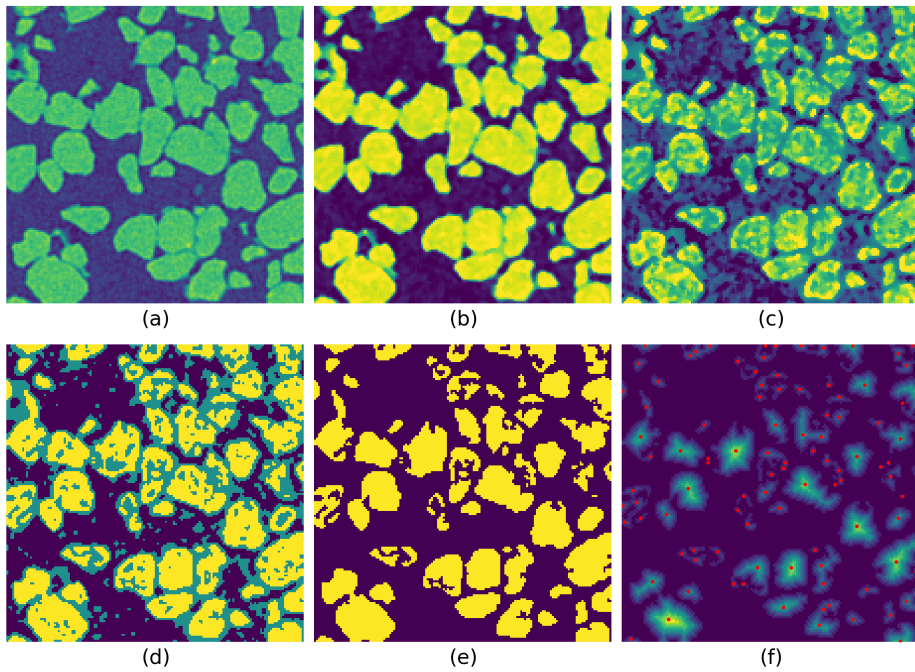


Figure 5.3 (a) Image depicting sand grains sliced from a 3D CT scan. (b) Image rescaled to the range defined by the 5th and 95th percentile intensities. (c) Rescaled image after histogram equalization to enhance maxima within the particles. (d) Histogram-equalized image converted into a ternary image following application of a multi-Otsu algorithm with three classes. (e) Binary image created by thresholding the with uppermost value calculated by multi-Otsu algorithm. All holes within resulting regions of binary image are filled. (f) Euclidean distance transformation of multi-Otsu binary image with local maxima denoted by red points.

removed. Over-segmented regions will be merged according to edge strength between the markers, so having a marker lie on an edge between two particles may prevent the edge from being detected. To remove the markers closest to edges, an image is created that enhances the intensity of particle edges by applying a Sobel filter, implemented in *scikit-image*, to the rescaled image (Figure 5.4.b) [158]. In this image, the strongest edges are represented by the highest intensities in the image. The edges in the Sobel-filtered image are further emphasized by performing adaptive histogram equalization from *scikit-image*, which increases the intensity of the weaker edges between particles.

Sampling the intensity of the edge image (Figure 5.4.c) at the locations of the inverse distance transformation minima, the points closest to the edges will have the highest intensity. The points with intensities above the 95th percentile are removed (Figure 5.5.b). The remaining minima will be used as markers to seed the watershed segmentation.

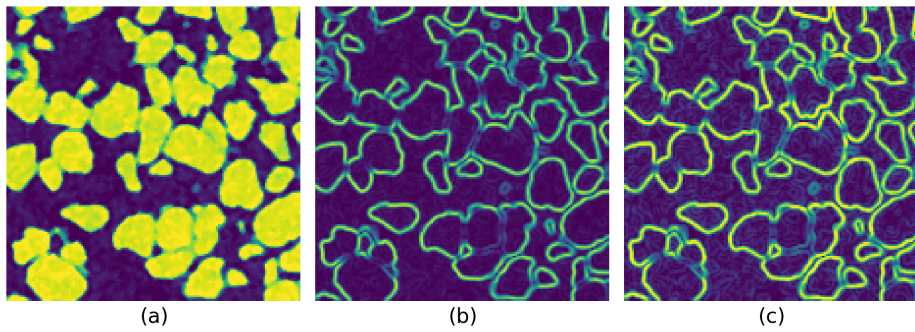


Figure 5.4 (a) Rescaled image depicting sand grains (Figure 5.3.b). (b) Rescaled image after application of a Sobel filter to enhance the edges of particles within the image. (c) Sobel-filtered image after adaptive histogram equalization is performed to further enhance particle edges.

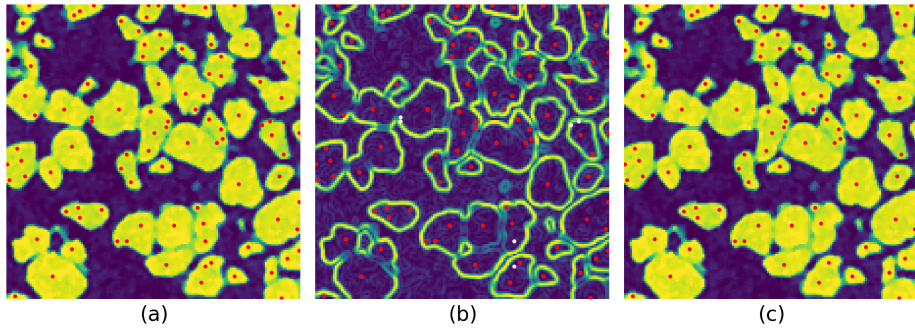


Figure 5.5 (a) Rescaled image depicting sand grains overlaid with inverted distance transformation minima in red. (b) Edge image (Figure 5.4.c) with minima overlaid. White points are removed by filtering process for being too close to the particle edges while red points will be used as markers for the watershed segmentation. (c) Edge-filtered local minima (red) overlaid on the rescaled image.

The filtered markers seed a watershed segmentation operating on the inverted distance transformation (Figure 5.6.b) created from the multi-Otsu-binarized image (Figure 5.3.e). Compared to the visually discernible sand grains in the raw image (Figure 5.6.a), the results of the watershed segmentation appear over-segmented as desired for this stage of the procedure (Figure 5.6.c).

### 5.3 Delaunay Triangulation to Connect Markers and Detect Edges

A method has been developed to merge the over-segmented regions according to edges detected in the vicinity of the regions. Locations between two regions determined to be neighbors must be searched for edges. The regions will be merged if an edge is not detected between the two regions. Before this can happen, however, a method is needed

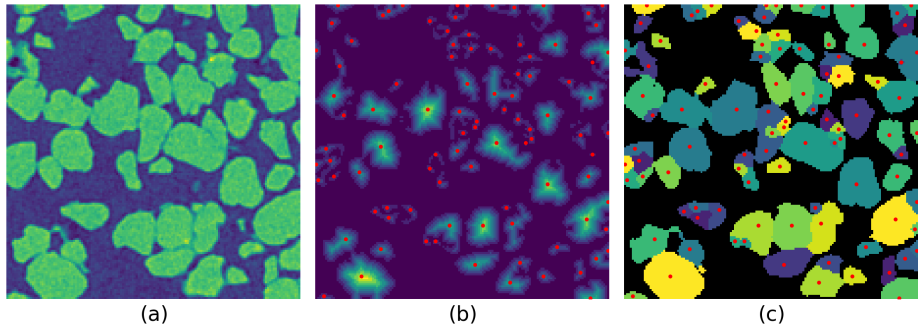


Figure 5.6 (a) Image depicting sand grains to be segmented. (b) Euclidean distance transformation of multi-Otsu-binarized image (Figure 5.3.e) with edge-filtered local maxima denoted by red points. (c) Watershed segmentation results of the inverted Euclidean distance transformation seeded by the edge-filtered local maxima in previous image.

for determining neighboring regions. Each marker used to seed the segmentation will correspond to one region, so the markers can be used to determine region neighbors, but this process is still nontrivial. As multi-sized markers will have neighbors at varying distances, a method is needed that will connect each marker to its neighboring markers without prior information about the distance to those neighboring markers. This can be achieved using Delaunay triangulation, which calculates triangles between a distribution of points such that no other points are within the circumcircle each triangle creates [159–161]. The result is a structure that connects points with line segments of varying lengths that do not overlap. Delaunay triangulation has been applied to image segmentation before as an alternative method to watershed segmentation. Wen et. al use Delaunay triangulation to segment clumps of nuclei in cell-based fluorescent imaging [162]. In their method, points of high curvature are detected in an image. These points are connected via Delaunay triangulation and a geometry constraint is applied to the triangulated lines to select the lines that separate the nuclei. The method achieves results that align with expectations, however an important requirement for this success is the consistently round shape of the segmented nuclei such that points of high curvature in the binary image only occur at the points of contact between the particles. Due to the irregular shape of the sand particles in the present work, there are high points of curvature around the perimeter of single sand grains, not only where the grains are in contact, so this method would not be effective. Instead of trying to use Delaunay triangulation as a replacement for watershed segmentation, the routine presented in this work uses Delaunay triangulation to assist in merging over-segmented regions.

The neighbors of each marker are determined by calculating a Delaunay triangulation with *SciPy*, using the markers corresponding to over-segmented regions (Figure 5.7.a) as the input vertices. The resulting network of lines connect each marker to neighboring markers (Figure 5.7.b). This is useful in the context of irregularly-shaped and multi-sized particles because the lines connecting neighboring markers can be drastically different lengths. Sampling the intensity of the edge image along each of these lines yields intensity profiles, analysis of which is used to define the edge detection. With a robust enough definition of a detected edge, edges can even be detected between tightly-clustered sand grains. In this work, an edge is defined as detected between two neighboring markers if the maximum intensity along the line connecting the markers satisfies two conditions: (1) the maximum intensity along the line must be greater than 10 percent of the edge image global maximum, and (2) the maximum intensity along the line must not occur at either end of the line. Most strongly defined edges in the image are near the edge image global maximum, but the edge detection definition must encompass a larger range of values to capture the weakly defined edges which have a much lower intensity. Since this edge detection value is so low, some lines that don't cross any edges are falsely flagged as crossing an edge. This typically happens when one or both markers at either end of the line are near particle edges, hence the necessity of the second condition. The number of falsely flagged edges is reduced by ignoring detected edges when the maximum intensity of the line occurs at either endpoint. Markers that are connected by lines on which edges are not detected are defined as belonging in the same “particle neighborhood” and are merged in the final stage of the procedure. The criteria used here for forming these particle neighborhoods were determined based on observation of the edges in this image and could be tailored to specific experiments.

## 5.4 Results

Particle neighborhoods created with the Delaunay edge detection algorithm are used to correct the over-segmented results (Figure 5.8.b) obtained from the watershed segmentation. The regions corresponding to each of the markers within a particle neighborhood are merged such that each particle neighborhood has only one associated region in the final segmented regions (Figure 5.8.c).

The merging algorithm yields a segmentation that appears to more closely align with expectations than the results from a typical watershed segmentation when compared to the visually discernible grains in the original image (Figure 5.8.a). However, in order to quantitatively determine the extent to which the merging algorithm improves the results obtained from the watershed segmentation, the results from the typical watershed and

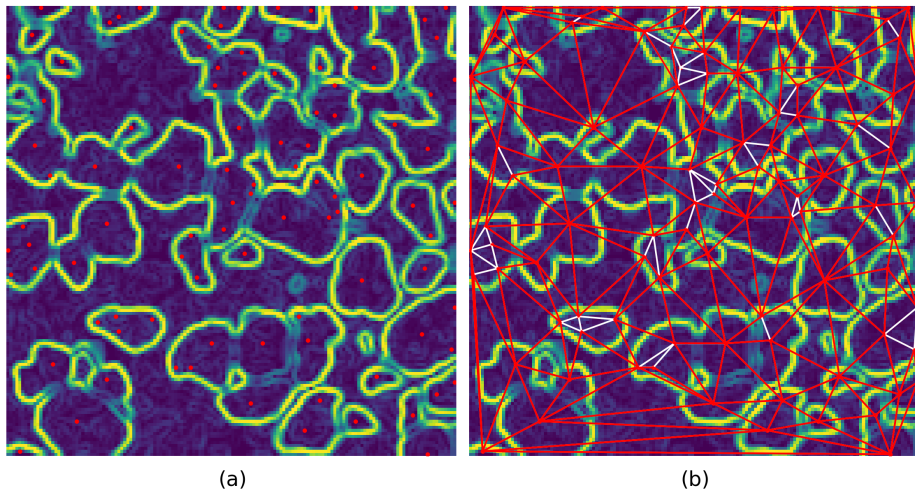


Figure 5.7 (a) Edge-filtered maxima used as markers (red) overlaid on the edge image (Figure 5.4.c). (b) Edge image overlaid with Delaunay triangulation. Red lines denote lines across which an edge was detected while white lines denote lines across which no edges were detected. Markers connected by white lines are defined as existing in the same “particle neighborhood”.

merged-region segmentations are compared to a manual segmentation of the sand grains. To generate the manual segmentation, a digital drawing application with multi-layer functionality was used to individually draw the footprint of each segmented grain on a separate layer overlaid on the raw image. Each layer was then exported as a separate PNG image. These images were loaded into Python using *imageio* and *NumPy*, and the grain in each labeled image was assigned a unique integer ID using *scikit-image*.

It is nontrivial to calculate the fit between two separate segmented images, even though the images both represent the same system. Even when labeled regions are relatively closely aligned, the labels in each segmented image will most likely not match. To solve this problem, an algorithm was written to match the labels across two separately segmented images based on maximum overlapping area without reusing any labels. This allowed for a match value to be calculated by summing the overlapping matching pixels and dividing by the sum of all pixels, matched and mismatched. Using this method, a match of 82.09% was calculated between the manual segmentation and the typical watershed segmentation, whereas a match of 89.02% was calculated between the manual segmentation and the merged-region segmentation.

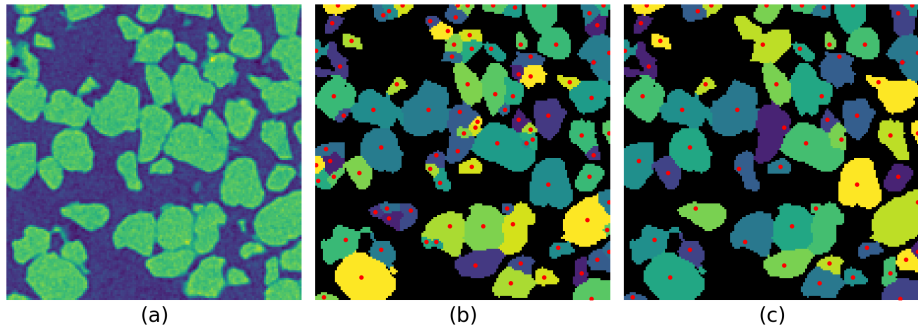


Figure 5.8 (a) Image depicting sand particles to compare with segmentation results. (b) Over-segmented regions resulting from extended watershed routine, but before regions are merged (Figure 5.6.c). Red points correspond to marker used to segment the region. (c) Final segmented regions after merging neighboring regions without a separating edge (Figure 5.7.b). Each red point corresponds to the marker of a merged region closest to the average location of all the centroids of the merged neighboring regions.

## 5.5 Discussion

The novel segmentation method proposed in this work achieves segmented results that are approximately 7% more accurate than a typical watershed segmentation when each are compared with the same manual segmentation. An overlay of the mismatched pixels can be used to visualize the improvements between segmentations more clearly than a simple comparison. Each segmentation is plotted with red pixels overlaid indicating mismatched with the manual segmentation. This visualization represents the higher number of mismatched pixels in the typical watershed segmentation (Figure 5.9.c) as a higher number of red pixels than in the merged-region segmentation (Figure 5.9.f).

The largest disagreement between the mismatch of the typical watershed and merged-region segmentations is a cluster of sand grains at the bottom center of each image. In the manual segmentation, the cluster is identified as four large sand grains and one small sand grain. In the typical watershed segmentation, the cluster is incorrectly identified as three sand grains: the small sand grain, one large sand grain, and the final three large sand grains identified as a single, larger grain. This is an example of under-segmentation because the segmentation routine did not segment the sand grains enough. The visualization of this mismatch (Figure 5.9.c) also provides some insight to the functioning of the mismatch calculation algorithm mentioned before, as the red overlay classifies only two of the three large grains in the cluster as mismatched, rather than all three. The third grain is classified as the matching portion of the cluster because it is the largest constituent of the cluster and therefore provides the highest number of

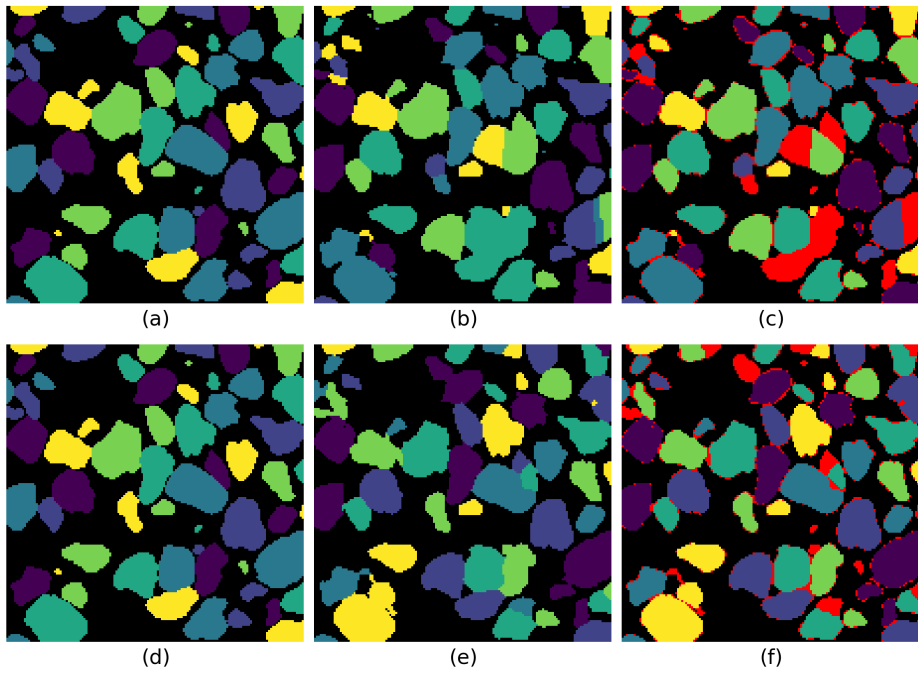


Figure 5.9 (a) Manual segmentation from hand drawing individual overlays on each visually discernible sand grain. (b) Typical watershed segmentation (Figure 5.2). This segmentation achieves an 82.09% match with the manual segmentation. (c) Watershed segmentation with red overlay depicting pixels mismatched from the manual segmentation. (d) Manual segmentation plotted again for ease of comparison with merged-region segmentation. (e) Merged-region segmentation from merging over-segmented neighboring regions without a separating edge (Figure 5.8). This segmentation achieves an 87.02% match with the manual segmentation, approximately a 7% improvement from the typical watershed segmentation. (f) Merged-region segmentation with red overlay depicting pixels mismatched from the manual segmentation.

overlapping pixels out of the three grains. This same cluster of five particles is identified differently in the merged-region segmentation. Each of the four large sand grains were identified, but the small grain was identified as part of the rightmost large sand grain. Even though the merged-region segmentation results are not perfect for this cluster, misrepresenting the small sand grain results in fewer mismatched pixels than the two larger mismatched grains in the typical watershed segmentation.

The next largest mismatch disagreement between the typical watershed and merged-region segmentation is a pair of tightly clustered sand grains, one large and one medium sized, near the center of the image. In the typical watershed segmentation, the grains are segmented into two regions, but the segmentation occurs at the wrong location, leading to the entire small sand grain identified as mismatching along with half of the large grain. In the merged-region segmentation, the large sand grain is mostly

segmented correctly (aside from a small region near the boundary with the medium grain) and the small sand grain is over-segmented into two regions instead of one. Once again, the mismatch in the merged-region segmentation is less than that of the typical watershed segmentation.

Another mismatch disagreement is in the segmentation of a large sand grain on the lower right edge of the image. In the typical watershed segmentation, the grain is over-segmented into three separate regions. The largest of these regions is identified as matching with the manual segmentation, which leaves the two smaller regions as mismatch. In the merged-region segmentation, the sand grain is correctly identified as a single region. Contrasting this over-segmentation and directly below this large grain in the bottom right corner is a pair of medium sand grains that are improperly under-segmented as a single region in the typical watershed segmentation. The two grains are segmented correctly in the merged-region segmentation, however, with only a thin region of mismatch between the two grains.

Though the merged-region segmentation was calculated as more closely matching the manual segmentation overall, there are still a few regions of mismatch disagreement between the two segmentations where the typical watershed routine yielded a segmentation that was closer to the manual segmentation than the merged-region segmentation. The largest of these regions is a pair of medium-sized grains in the top center of the image. While these grains are properly segmented in the typical watershed segmentation, the grains are under-segmented as a single region in the merged-region segmentation. This leads to the smaller of these grains being identified as mismatching. This kind of under-segmentation is also seen between a medium and small sand grain in the upper left side of the merged-region segmentation, though this pair of sand grains is also misrepresented in the typical watershed segmentation as four regions. A similar example in which the merged-region segmentation under-segmented a small sand grain occurred for a small sand grain between two larger grains in the bottom left corner of the image. The sand grain was segmented separately in the typical watershed segmentation, though even in that segmentation the surrounding area was still identified as mismatching in a way reminiscent of the merged-region segmentation.

There are also a few cases of over-segmented grains in the merged-region segmentation that are not present in the typical watershed segmentation. The largest of these is a medium sand grain in the bottom center of the image that was improperly segmented into two regions. The rest of the over-segmented regions in the merged-region segmentation (besides the over-segmentation of the smaller of two tightly clustered sand grains previously mentioned) are around the edges of the image (e.g., top

left edge, top right edge, top right corner, bottom right edge). These over-segmented regions are all rather small, so they don't contribute much to the overall mismatch with the manual segmentation, but their presence raises the question of whether this algorithm would be even more successful if it was applied to an image that contained only complete particles not split by image borders.

The last features to note in these images are the portion of the red overlays corresponding to thin regions around the edge of some sand grains. These pixels correspond to small regions of mismatch where the footprints of the manual and typical/merged-region segmentations do not agree. These mismatched areas are present because both the typical watershed and merged-region segmentations require a semantic segmentation step to create a binary image differentiating particles from background. From this binary image, markers are generated and passed to the instance segmentation portion of the routines to segment and label the individual particles. This process is mostly the same for the typical watershed and merged-region segmentation, resulting in similarly mismatched regions along the edges of the particles where the semantic segmentation slightly differs from the footprint of the manual segmentation. The reason these regions are only mostly the same for these segmentations is because the process of selecting markers from each semantic segmentation is slightly different in the merged-region segmentation versus the typical watershed, as described previously. This leads to some of the smallest sand grains not receiving a marker in one segmentation, but receiving a marker in the other, leading to discrepancies in the mismatch. Regardless, these regions are small, so their contributions to the larger mismatch of the image are minimal.

## 5.6 Conclusions

This work presented a procedure to improve the segmentation of irregularly-shaped, multi-sized, and tightly-clustered particles using a method that merges regions based on edge strength. A 2D image taken from a 3D XCT scan of polymer-bonded sand grains was used as an example image. The procedure preprocesses the image to create a binary image separating the sand grains from the background and generates a set of markers to intentionally over-segment the particles. The majority of the procedure lies in a custom algorithm which utilizes Delaunay triangulation to merge neighboring regions that are not found to be separated by an edge.

The merged-region segmentation appears to be an improvement over a typical watershed segmentation, however a manual segmentation was also performed and used as a baseline to quantitatively assess the improvement. The fit between the manual

segmentation and merged-region segmentation is calculated and compared to the fit between the same manual segmentation and the typical watershed segmentation. The merged-region segmentation was calculated to be an 89.02% fit with the manual segmentation. This is a 6.93% improvement over the typical watershed segmentation, which was calculated to be an 82.09% fit with the same manual segmentation.

# CHAPTER 6

## SEGMENTFLOW: A SEGMENTATION WORKFLOW PACKAGE FOR CREATING SIMULATION-READY GEOMETRIES FROM 3D IMAGE DATA

This chapter presents *Segmentflow*, a segmentation workflow tool that can be used to generate geometries for use in image-based physics simulations. The capabilities of *Segmentflow* are demonstrated by presenting the process of creating surface meshes from a CT scan of a mock high explosives system consisting of tens of thousands of F50 sand grains coated in a Kel-F polymeric binder. Segmented particles are produced from segmentations seeded in five different ways. Each segmentation is analyzed to assess the accuracy compared to typical F50 sand. Surface meshes are created from the segmented particles resulting from the segmentation with the lowest error. An example surface mesh is subject to a variety of postprocessing and the resulting surfaces are compared. This postprocessing exhibits the important ability of *Segmentflow* to control the complexity that geometry introduces to simulations.

### 6.1 Introduction

*Segmentflow* is a Python package for creating segmentation workflows which convert 3D image data to a format usable in image-based simulations. This software has been designed to be flexible enough to be used for a variety of applications and data types. Part of what makes *Segmentflow* flexible is the ability to tune the segmentation process and the format of the resulting outputs.

*Segmentflow* was designed to extract the geometries of granular particles embedded in a polymeric matrix for image-based simulations. Specifically, the behavior of these particles would be simulated in quasi-static, unconfined compression by performing a direct numerical simulation (DNS) on the real geometries extracted with *Segmentflow*. These samples are imaged using x-ray computed tomography (XCT). For the granular particles, the goal of the segmentation is to separate each particle from the other particles and the polymeric binder, then to convert the grayscale intensity voxel data to a labeled voxel format and a collection of surface meshes (one surface mesh for each particle). Each of these output types would be used as inputs for a different type of simulation software.

*Segmentflow* ties together the functionality from many powerful Python libraries. To improve make interfacing with *Segmentflow* more user-friendly, YAML files are used to

pass input parameters to *Segmentflow* functions using the package *PyYAML* [163]. To load and save images, the package *imageio* [99]. Image data and manipulations are performed using *NumPy* arrays [98]. Viewing images and plotting data and information about these images is accomplished with *Matplotlib* [108]. Many useful image processing algorithms implemented in *scikit-image* are utilized [100]. To save surface meshes in the STL file format, the package *numpy-stl* is used [164]. Finally, image postprocessing methods as well as 3D visualization rely on the powerful 3D data processing library *Open3D* [165].

There are two types of segmentation, and the distinction between these types is important for *Segmentflow* because many segmentation workflows depend on both types. The first type of segmentation, semantic segmentation, is the process of separating, or segmenting, features in an image by type or class. Semantic segmentation on its own can be useful to determine information like volume fractions, but often a semantic segmentation is the first step for a more involved analysis. There are different methods for performing semantic segmentation, often by setting a series of threshold values in an image and classifying features between those values. This can be done manually or procedurally. A common algorithm for procedurally determining threshold values is known as multi-Otsu thresholding [44]. The second type of segmentation is instance segmentation. In instance segmentation, a region/class of an image, is segmented into individual feature instances, or segmented particles, of that class. Often instance segmentation operates on a binary representation of a class previously determined via semantic segmentation. These segmented particles will be identified via labeled voxels in which each voxel corresponding to a unique particle will be labeled with a unique integer.

A common type of instance segmentation is watershed segmentation. Watershed segmentation can be thought of as a simulated flooding process applied to an image [45–48, 153]. As a watershed algorithm is applied to an image, the intensities of the image act as elevations of a topographic surface. Simulated “water” can be filled from the lowest elevations first, equal across the full image, or the water can be “poured” from specifically locations called markers [49, 50]. As the water fills the surface, separate “catchment basins” regions that started filling in different places begin to near one another. Any time two catchment basins come into contact, a “dam” is created. The algorithm finished when the image has been completely filled, or reaches a specified elevation/intensity. The resulting dams denote the segmented regions. It is common for watershed segmentation to be applied to a distance transformation of a binary image, which in the case of the Euclidean distance transformation (EDT), assigns a new value

to each foreground pixel according to the distance to the nearest background pixel [154]. This creates an image that is more logically akin to an elevation map, as the distance map has a natural gradient. The distance transform of a few black spots on a white image would appear as a mountainous island, with the peak of the island at the farthest point from the shore of the metaphoric white sea. If the distance map is inverted, a gradual depression is formed that can be filled by the algorithmic flooding using information about the morphology of the foreground region in an image to segment the features.

## 6.2 Methods

To demonstrate the capabilities of *Segmentflow*, a full CT scan to simulation geometry workflow is demonstrated on a mock high explosives system consisting of F50 sand grains coated in a polymeric Kel-F binder. The sand was coated with the binder and pressed into a cylindrical sample. The goal of the workflow is to create segment the sand grains from the binder and create a series of surface meshes representing each of the tens of thousands of sand grains in the sample such that the surface mesh representation of the sample could be loaded into a simulation software as an initial condition for physics simulations, such as deformation. This demonstration uses *Segmentflow* to load parameters from an input file, preprocess the CT scan images to improve the contrast, perform a semantic segmentation to identify the sand grains, create a surface mesh for each segmented particle and save that mesh as an STL file, and finally postprocess the surface meshes to change the properties of the meshes. Though this work mainly focuses on the workflow for this particular material system and application, alternative functionality is presented throughout the demonstration to show how the workflow and parameters might be adapted to other systems.

### 6.2.1 Input Handling

*Segmentflow* was designed to create simulation-ready geometries for a wide range of applications, so a parameter specification system is important to tune the various algorithms the packaged leverages to segment a specific dataset. Since *Segmentflow* is a Python package, it can easily be installed so that the functions within may be imported into other Python scripts. However, to make *Segmentflow* more user friendly, it was structured such that it could be operated by workflow scripts. Each script is tailored to a specific workflow and has its own accompanying input loading function that pulls parameters from an input file in YAML format. This allows parameters to be listed quickly and easily with text in a human-readable way while also listing out the potential

parameters that can be adjusted without having to dig through documentation to know what can be changed. The YAML file format has the added benefit of allowing parameters to be grouped together. For the *Segmentflow* input file, the grouping was made according to the section of application the parameter affects. Grouping makes tuning segmentation behavior more clear for the user while also improving code readability because parameters loaded into *Segmentflow* are stored in a nested dictionary according to these groups. In an effort to further improve accessibility, any parameters in input files are able to be left blank to set parameters to the default value. This allows users to use *Segmentflow* even if they are unfamiliar with the parameters. Parameter specification using an input file makes the segmentation routine reproducible because *Segmentflow* can be executed with the same input file multiple times to achieve the same results. A copy of the input file is also saved to the output directory specified in the input file for two reasons: to backfill default values that may have been filled for empty parameters and to store a record of segmentation parameters to preserve reproducibility in case the original input file is altered.

### 6.2.2 Preprocessing

Image preprocessing is the portion of the F50 sand segmentation procedure involves loading the raw 3D data and performing operations to improve the contrast. The location of the directory as well as the image file format are specified in the input file. With the images loaded, the next step of the preprocessing routine is to perform a series of steps, as specified in the input file, to improve the contrast of the images. In the F50 sand procedure, a median filter is applied to the CT scan to replace each voxel with the median value of the surrounding cube of voxels, reducing localized noise while maintaining the sharpness of edges (unlike Gaussian filtering which will blur edges). Intensity clipping is also performed to improve contrast by taking advantage of the full range of available intensities according to the image data type. This is done by providing an upper and lower percentile interval in the input file. The range used to rescale the F50 sand sample was [0, 99.9].

### 6.2.3 Semantic Segmentation

In the F50 sand sample, the classes that exist within the images are void, particle and binder. *Segmentflow* uses an implementation of this algorithm *scikit-image*. Multi-Otsu thresholding divides an image into  $N$  classes based on the distribution of intensities in an image by maximizing inter-class variance. To make *Segmentflow* more flexible,  $N$  is

included as an input file parameter for some workflow scripts. *Segmentflow* also includes a custom thresholding algorithm that uses a Gaussian filter to smooth the histogram of the 3D image, calculate the local maxima corresponding to the peak intensity relating to the three feature classes in images (void, binder, and sand grain). Minima are found between each of the maxima and used as the threshold values (Figure 6.1).

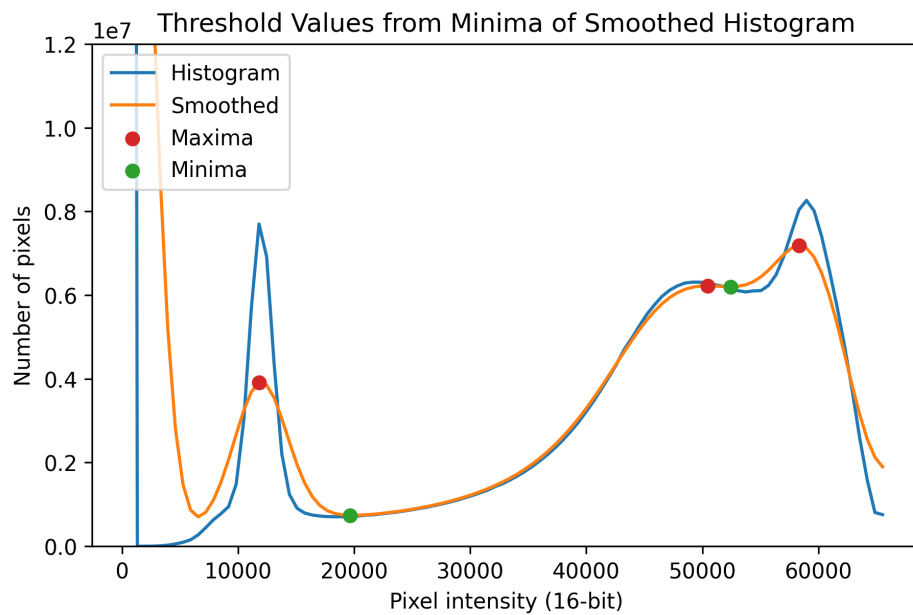


Figure 6.1 Histogram processing used to determine the threshold values to perform semantic segmentation on images. The blue line represents the raw histogram. The orange line represents the smoothed histogram. The red points denote the local maxima. The green points denote the local minima between these maxima which are used to threshold the material classes.

If this is a sufficient amount of segmentation for the given application, *Segmentflow* can save a voxel representation of the classes without undergoing further segmentation of the foreground. If this option is specified in an input file, each voxel of a class is represented by a unique integer label and saved as a collection of 2D images. Otherwise, after dividing the image into  $N$  classes, a subset of those classes are selected to form a binary image which is used to segment the defined class or classes into instances and/or create surface meshes of the features. To demonstrate the instance segmentation capabilities of *Segmentflow*, the semantic segmentation of the F50 sand sample (Figure 6.2.c) is binarized by selecting only the class corresponding to the sand grains.

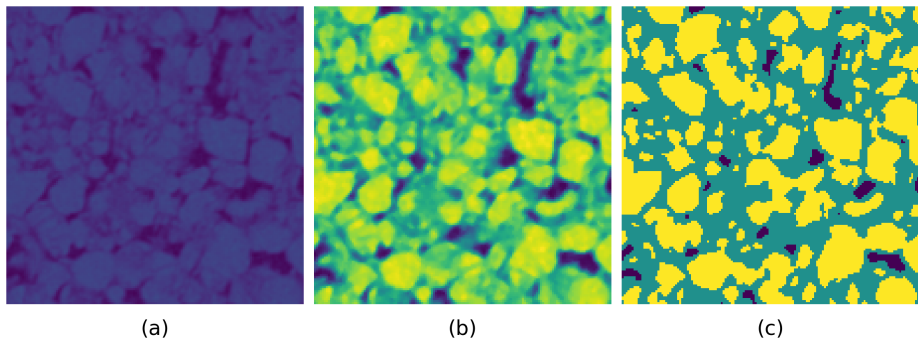


Figure 6.2 (a) Low contrast image slice from raw CT scan. (b) Image slice after intensity is rescaled. (c) Semantic segmentation following thresholding of rescaled image using the minima of the smoothed histogram (Figure 6.1). The purple regions represent the void class, the blue regions represent the binder class, and the yellow regions represent the sand grain class.

### 6.3 Instance Segmentation

*Segmentflow* uses a watershed algorithm in 3D to perform instance segmentations. First a distance map is calculated by applying an EDT algorithm implemented in *scikit-image* to a binary image. In the case of this demonstration of the F50 sand sample, a distance map is created using the binary image corresponding to the sand grain class. Local maxima are calculated to determine the markers which will seed the watershed algorithm. The 2D metaphor of watershed flooding does not extend well to 3D, but the marker points act as the starting locations from which the segmented regions will “grow” outwards. Not all local maxima from the distance map are used as markers. Only the maxima separated by a minimum distance are used. The final segmentation depends greatly on this minimum peak distance value as the number of markers is equal to the number of labeled features, or segmented particles, in the resulting segmentation. If this value is too large, the results will be under-segmented as fewer markers than sufficient are passed to the watershed algorithm, excluding maxima that are closer together than this minimum distance. This would create segmented particles larger than the true sand grains. If the value is too large, the opposite will be true: too many maxima are identified and passed to the watershed algorithm as seeds. With more markers than necessary, the results will be over-segmented as separate markers identified in the same feature will split that feature into multiple segmented regions. This would produce segmented particles smaller than the true sand grains. Segmentations were performed at a range of minimum peak distances and the resulting particles were analyzed to determine which minimum peak distance value yielded particle sizes closest to typical F50 sand.

### 6.3.1 Surface Mesh Creation

Depending on simulation type, a voxel representation of the segmented particles may be an adequate format for the geometry. However, some simulations require geometries be represented as a surface mesh rather than voxels. *Segmentflow* can output triangular surface meshes saved as STL files for each feature segmented. There are currently two voxel preprocessing methods available in *Segmentflow* to simplify geometries before any surface meshes are created: voxel smoothing and morphologic erosion. For each method, the voxels of each segmented feature are first isolated in a new 3D array. In voxel smoothing, a median filter is applied to the voxels such that each voxel is replaced by the median value (foreground or background) of the surrounding voxels ( $3 \times 3 \times 3$  cube). In morphologic erosion, the outer layer of voxels is removed, as if peeling an onion. This is performed using an algorithm implemented in *scikit-image*. The algorithm can be applied multiple times (peeling multiple onion skins) to further reduce the overall size of a feature. This can be useful to ensure voxels of separately segmented features are not in contact. After these steps, surface meshes are created for the segmented features using a marching cubes algorithm. This algorithm takes the voxels at the surface of the 3D feature and generates a surface consisting of vertices and triangles connecting the vertices [166, 167]. Each triangle has one of 26 possible normals based on the position of the other surface voxels in the immediate vicinity: six possibilities for the Cartesian vectors when neighbors of a voxel form a flat surface, 12 vectors when the voxels form an edge, and eight vectors when voxels form a corner. The *scikit-image* implementation of the algorithm allows a voxel step size to be specified to control the granularity of the voxels used to create the surface mesh. If a step size of 1 is used, each voxel is analyzed to create the surface mesh, whereas step sizes larger than 1 produce coarser mesh results, compromising finer-scale details of the volume. Resulting surface meshes can be saved as STL files.

### 6.3.2 Surface Mesh Postprocessing

The surface meshes output from the marching cubes algorithm are blocky due to the limited number of surface normals output from the data. This is an artifact of the voxel nature of the data passed into the marching cubes algorithm and is therefore not truly representative of real-world geometries. *Segmentflow* has two mesh postprocessing methods to further process the 3D data: smoothing and mesh simplification. Smoothing the blocky surface meshes output by the marching cubes is achieved through Laplacian smoothing, which interpolates normal vectors for the faces of a mesh. These meshes

may still have a large number of surface elements however because the smoothing operation does not change the number of triangles. To reduce the number of triangles, simplification can be performed through quadric decimation [168]. *Segmentflow* implements the mesh simplification by accepting a target number of triangles for the final mesh and a scale factor that allows the number of triangles to be reduced iteratively. Often smaller simplification factors yield better results because more of a surface's shape is able to be retained between smaller simplifications. Tuning the size of output surface meshes is an important feature of *Segmentflow* because the complexity of the meshes will in part determine the scale of a simulation using the geometries.

## 6.4 Results

Two separate methods were used to calculate the size distribution of segmented particles resulting from different segmentations on the same F50 sand and Kel-F CT scan. Segmented particles were analyzed for watershed segmentations seeded with markers determined with minimum peak distance values ranging from 4 to 8. These values correlate to physical distances from 55.36 to 110.72  $\mu\text{m}$ . Each method determined whether or not a particle would be retained in a separate way. The first method used spheres of equivalent volume for each segmented particle. The second method used the aspect ratio of the bounding box of each particle. To determine which minimum peak distance resulted in the most accurate size distribution, each segmentation is compared with the standard size distribution of F50 sand (Figure 6.3).

### 6.4.1 Sphere of Equivalent Volume to Determine Size

The first method method for calculating segmented particle size distribution took the volume of each particle, calculated the diameter of the sphere with an equivalent volume, and used this diameter to bin the particles between sieve mesh sizes (Figure 6.4). The error between each of the five segmentations was calculated as the cumulative difference between the equivalent sphere distribution and the typical F50 distribution. These errors are summarized for each segmentation in Table Table 6.1. The segmented particles seeded with a 6 pixel minimum peak distance has the lowest error with a cumulative difference of 25.08%. Particles seeded with a 4 pixel minimum peak distance had the largest error at 79.29%.

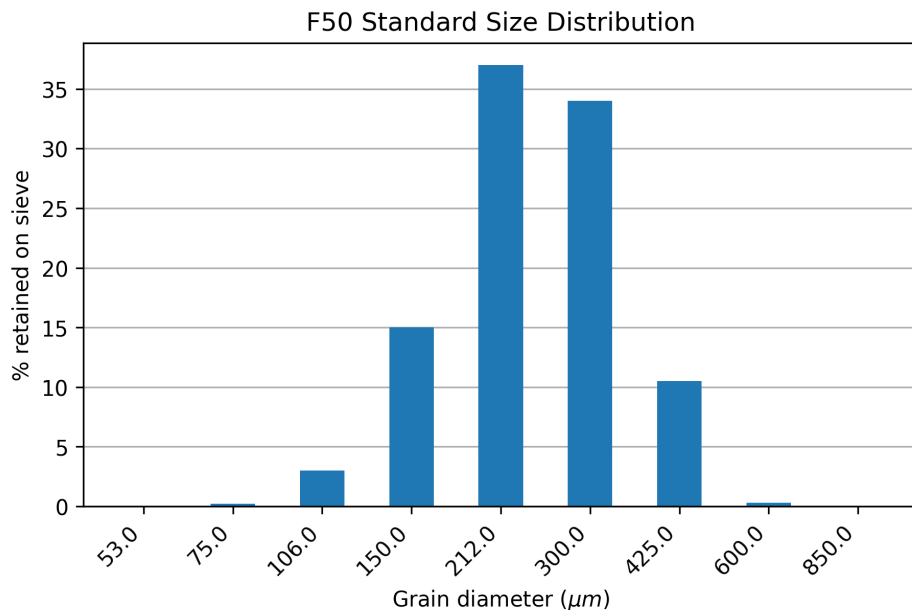


Figure 6.3 Expected result from passing F50 sand through a series of sieves, expressed in percent of total grains retained at each step. Sieve size is given in microns.

#### 6.4.2 Aspect Ratio of Bounding Box to Determine Size

The second method for calculating segmented particle size distribution found the aspect ratio of the bounding box of each segmented particle and used the maximum length of the minimum cross sectional area to bin the particles (Figure 6.5). Just like with the equivalent sphere method, the error between each of the five segmentations was calculated as the cumulative difference between the equivalent sphere distribution and the typical F50 distribution. These errors are also summarized for each segmentation in Table Table 6.1. With this method of assessing the segmentations, the particles segmented with a 5 pixel minimum peak distance have the lowest error with a cumulative difference of 45.31%. Particles seeded with an 8 pixel minimum peak distance had the largest error at nearly 95.59%.

The sum of absolute errors for each segmentation are summarized in Table Table 6.1, combining each method of determining the particle size, as well as the total error which is the sum of the error from both methods. Based on these errors, the watershed segmentation seeded with markers determined by a 6 pixel minimum peak distance yields the results that most closely align with the typical F50 sand size distribution.

Using the optimal parameter as determined by measuring the size distributions, this segmentation is used to generate surface meshes for the entire sample.

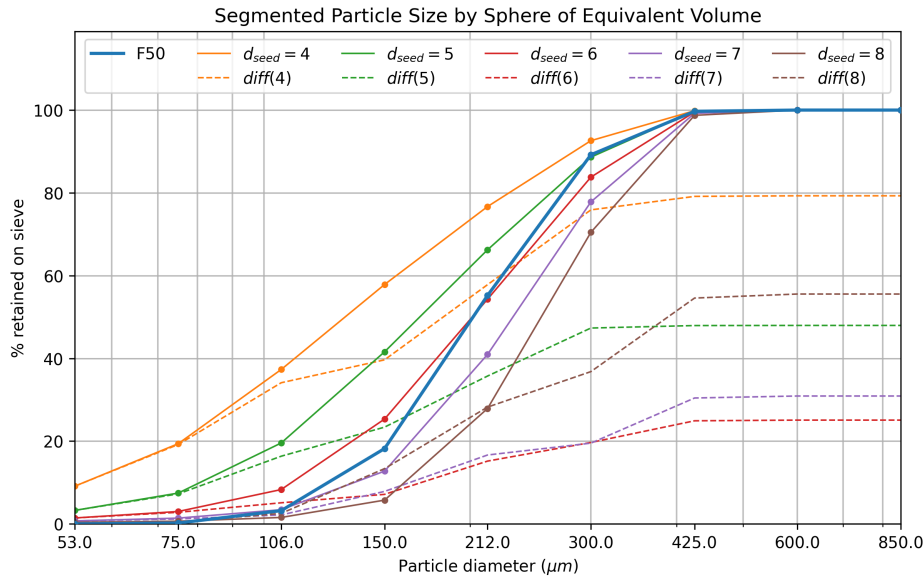


Figure 6.4 Size distribution of segmented particles binned according to the sphere of equivalent volume of each particle. Solid lines represent the cumulative distribution of particles at increasing sieve sizes. The blue solid line represents the typical values for F50 sand and the other solid lines represent the values determined from the particles obtained by segmenting the CT scan with a watershed algorithm seeded with different values for the minimum peak distance ( $d_{seed}$ ). Dashed lines of corresponding color represent the error between the segmentation and typical values.

## 6.5 Discussion

A visual example of the findings from the size distribution assessment is provided for the different segmentations of the Kel-F - F50 sand system. A comparison is made between an image sliced from the rescaled CT scan (Figure 6.7.a) and the slice at the corresponding location in each of the three segmentations determined to have the lowest total accumulated error in size distribution. These segmentations were seeded by markers selected with 5, 6, and 7 pixel minimum peak distances and are hereafter referred to as Segmentation B (Figure 6.7.b), Segmentation C (Figure 6.7.c), and Segmentation D (Figure 6.7.d), respectively. Labeled sand grains of interest (Figure 6.7.a) are compared to corresponding segmented particles in each of these segmentations.

Across these segmentations, there is a trend of particles that are more segmented in Segmentation B and become less segmented in Segmentation C and Segmentation D. There are not many over-segmented particles visible in this slice of the volume, but the evidence over-segmentation can be seen in the segmented representations of sand grain 3. In Segmentation B and Segmentation C this sand grain is over-segmented as

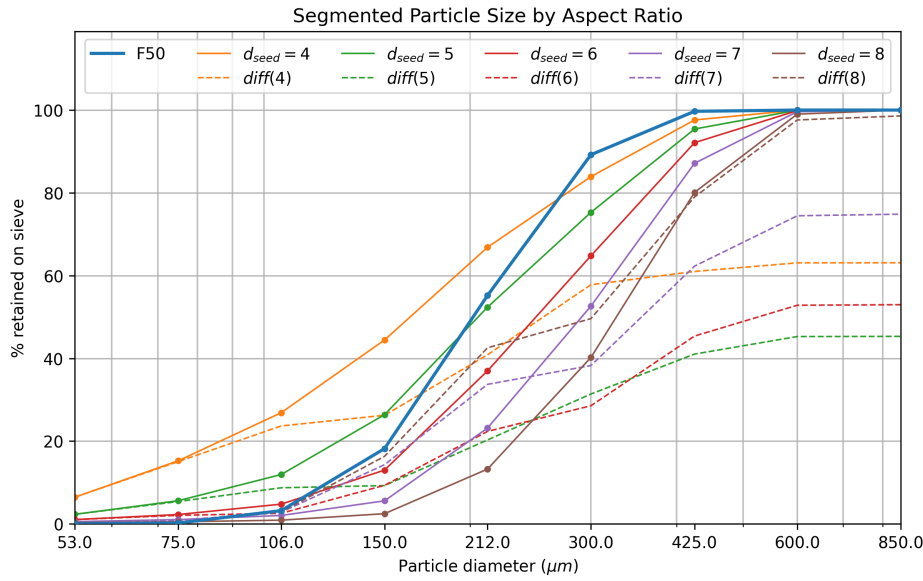


Figure 6.5 Size distribution of segmented particles binned according to the bounding box aspect ratio of each particle. Solid lines represent the cumulative distribution of particles at increasing sieve sizes. The blue solid line represents the typical values for F50 sand and the other solid lines represent the values determined from the particles obtained by segmenting the CT scan with a watershed algorithm seeded with different values for the minimum peak distance ( $d_{seed}$ ). Dashed lines of corresponding color represent the error between the segmentation and typical values.

two particles. In Segmentation D, these two regions are segmented as a single particle, but it is unclear from this slice whether or not the sand grain to the left is also merged into the particle. Other sand grains are represented distinctly in Segmentation B and Segmentation C but are erroneously under-segmented in Segmentation D as is the case with sand grain 1 and sand grain 2 as well as sand grain 11 and sand grain X. There are a few cases of sand grains segmented distinctly in Segmentation B that are under-segmented in Segmentation C and Segmentation D. This occurs with the pair of sand grains 8 and 9 as well as the group of particles 13, 14, and 15. Some particles are under-segmented in all three of the segmentations. This is true of sand grains 5 and 6, which appear as a single particle in each segmentation. There are also certain cases in which sand grains that segmented distinctly in Segmentation B appear to be un-segmented from surrounding binder material as is the case with sand grains 4 and 12. and what appears to be some of the surrounding binder material. The final class of particles that appear here are particles in Segmentation B, but are too small and close to other markers to appear in Segmentation C and Segmentation D due to the minimum distance of the markers chosen to seed these segmentations. This can be seen with sand grain 7.

Table 6.1 Segmented Particle Errors Relative to Typical F50 Sand

Error	$d_{seed} = 4$	$d_{seed} = 5$	$d_{seed} = 6$	$d_{seed} = 7$	$d_{seed} = 8$
<b>Equivalent Sphere</b>	79.29	47.95	25.08	30.90	55.54
<b>Aspect Ratio</b>	63.09	45.31	52.97	74.84	95.59
<b>Total</b>	142.38	93.26	78.05	105.74	154.13

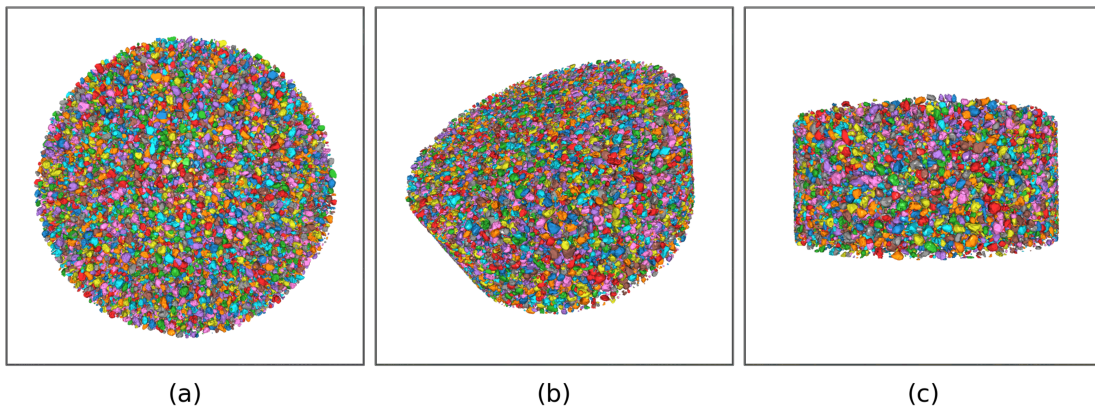


Figure 6.6 Surface meshes of all 41,553 particles segmented from the F50 sand sample loaded from three different views: (a) the top, (b) a high angle, and (c) the side.

All these examples show more under-segmented particles in Segmentation D than in Segmentation B and Segmentation C, though Segmentation B does have some under-segmented particles that appear to be properly segmented in Segmentation B. Regardless, Segmentation B and Segmentation C were both shown to minimize the lowest total accumulated error in the two size distribution analyses in part because the error was spread across the mean size of typically distributed particles, with some smaller particles as well as some larger particles. The other segmentations which resulted in higher total accumulated error mainly had particles that were either majority smaller or majority larger than the mean of the typical distribution. The fact that Segmentation C had the lowest total accumulated error suggests that the number of under-segmented particles balances out the over-segmented particles that are also shown to be present.

It is interesting that the watershed segmentation that performed the best was seeded with markers determined with a 6 pixel minimum peak distance. This correlates to a

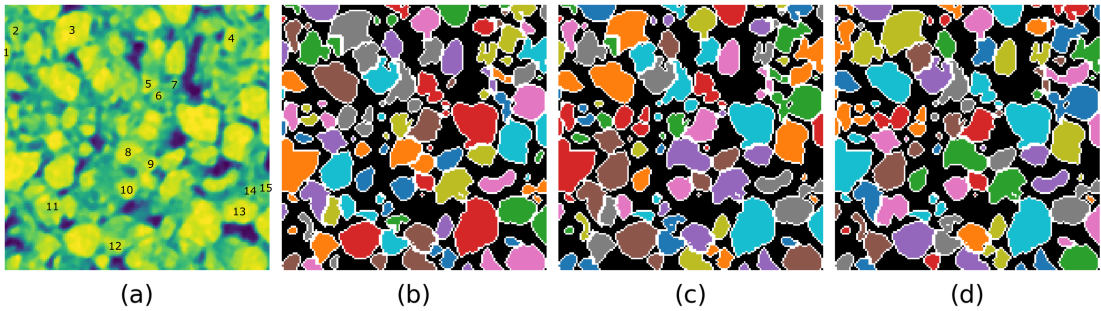


Figure 6.7 (a) A slice of the rescaled intensity CT scan image with particles of interest labeled to allow for ease of comparison and discussion between the three segmentations. (b) Corresponding slice of Segmentation B, as seeded by markers selected with a 5 pixel minimum peak distance, with the second lowest total accumulated error in particle size. (c) Corresponding slice of Segmentation C, as seeded by markers selected with a 6 pixel minimum peak distance, with the lowest total accumulated error in particle size. (d) Corresponding slice of Segmentation D, as seeded by markers selected with a 7 pixel minimum peak distance, with the third lowest total accumulated error in particle size.

physical distance of  $83.04 \mu\text{m}$  between markers, which is between the second and third smallest mesh sizes used to assess the particle sizes. The 4 pixel minimum peak distance, which corresponds most closely to the smallest mesh size ( $53 \mu\text{m}$ ) at a physical distance of  $55.36 \mu\text{m}$ , did not produce results that aligned well with the typical size distribution, with a total error among the highest of the tested segmentations. At a first glance, this is unexpected, as one might expect the minimum space between markers to be small enough to allow all the smallest particles to be segmented. However, this result shows that it is actually more important to choose a larger minimum peak distance to achieve a size distribution that is more representative of reality. As can be seen in the left-shifted cumulative size distributions of the 4 pixel minimum peak distance segmentation, the majority of particles are smaller than typical F50 particles. This means that generating markers based on a distance that is closer to the size of the smallest particles results in particles are over-segmented. In contrast, the best fitting 5 and 6 pixel minimum peak distance segmentations are distributed among each side of the typical F50 distribution, suggesting a balance of over- and under-segmentation.

To demonstrate the mesh postprocessing capabilities of *Segmentflow*, the surface mesh generated from the segmented particle corresponding to sand grain 10 (Figure 6.7.a) is shown independently and compared with the meshes resulting varying amounts of postprocessing. The surface mesh as-computed by the marching cubes algorithm is made up of 1524 triangles (Figure 6.8.a). After Laplacian smoothing, the mesh retains the same number of triangles, but the result appears less blocky

(Figure 6.8.b). The mesh is also shown after simplification past 200 triangles, resulting in mesh made up of 190 triangles (Figure 6.8.c). The final mesh shows extreme simplification past 20 triangles to a resulting mesh of only 10 triangles (Figure 6.8.d). This ability to tune the complexity of the surfaces of each segmented particle is referred to as the “exascale knob” as it allows the user to determine the complexity of the simulation which will use the resulting geometry.

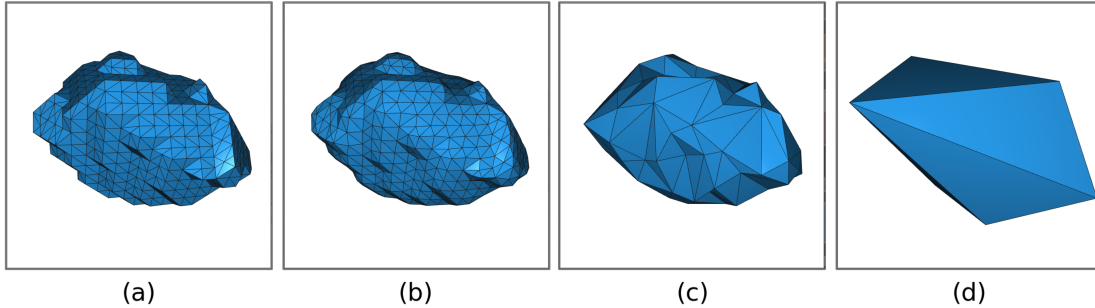


Figure 6.8 (a) Surface mesh produced from a segmented particle. Mesh originally has 1524 triangles across its surface. (b) Smoothing applied to surface mesh as part of the mesh postprocessing capabilities of *Segmentflow*. (c) Mesh simplified beyond 200 triangles. (d) Mesh simplified beyond 20 triangles.

## 6.6 Conclusions

This work presents *Segmentflow*, a segmentation workflow tool that can be used to generate geometries for use in physics simulations. A workflow is demonstrated that takes a CT scan of a mock high explosives system consisting of F50 sand grains coated in a polymeric binder. The CT scan was subject to a preprocessing procedure to increase the contrast of the image, at which point it was semantically segmented into regions labeled as one of three classes: void, binder, or sand grain. The regions corresponding to the sand grain class were subject to an instance segmentation procedure with the goal of segmenting and labeling voxels identified as individual sand grains. These segmented particles are dependent on the markers used to seed the segmentation algorithm. A variety of markers were selected by specifying a range of minimum distances separating the points. Each set of markers produced a different segmentation. The segmented particles resulting from each separate segmentation were analyzed to assess the segmentations.

Segmented particles resulting from five segmentations were analyzed. The size distribution of the segmented particles for each segmentation was compared with the

typical F50 sand size distribution to determine which segmentation yielded the most accurate segmentation. Two methods were used to determine the size distribution of the segmented particles from each segmentation. The first method used the volume of each segmented particle and calculated the diameter of the sphere of equivalent volume. This diameter was used to bin each particle between the mesh sizes defined by the typical F50 distribution. The second method used the aspect ratio of the bounding box of each particle and used the maximum length of the minimum cross section of the box to bin the particles. The sum of accumulated error was calculated for each method and the total accumulated error, summing the error from each method, was calculated for each of the five segmentations. The segmentation that was seeded by markers with a 6 pixel (83.04  $\mu\text{m}$ ) minimum peak distance was determined to have the lowest total accumulated error. A slice corresponding to the same location of the sample volume was taken from each of the three segmentations with lowest error and compared to provide a visual example of the quality of the segmentations.

The segmented particles resulting from the segmentation with lowest error was used to demonstrate the surface meshing capabilities of *Segmentflow*. The surface meshes were visualized together to show the complete geometry of the sample. Postprocessing capabilities were also demonstrated by comparing the unaltered surface mesh with smoothed and simplified representations. The particle was shown to maintain its general shape even when the number of triangles making up the surface was reduced by more than two orders of magnitude. This shows an important ability of *Segmentflow* to control the complexity of geometries and therefore the simulations for which these geometries will be used.

## CHAPTER 7

### SUMMARY AND CONCLUSIONS

This chapter summarizes the each previous chapter. Conclusions are also provided which address each of the research-driving questions posed in Chapter 1.

#### 7.1 Summary

Following the introduction in Chapter 1 and the literature review presented in Chapter 2, many topics were covered in Chapters 3 through 6. Chapter 3 presented a method for correlating x-ray intensity to sample composition by comparing intensity profiles in a radiograph to an EDS line scans measuring composition. Chapter 4 presented two automated procedures for identifying and tracking the solidification of metallic samples following laser melting. The results from each procedure were compared to manual measurements to assess the success of the automation. Chapter 5 presented a new method for the segmentation of irregular particles that cannot be accurately segmented with usual methods described in literature. This method proposed an extension to a typical segmentation method that produced results that were calculated to more closely match a manual segmentation than a typical segmentation on its own. Chapter 6 presented a Python package developed to establish a workflow for creating 3D geometries from images to be used in physics simulations. A segmentation workflow is demonstrated to generate surface meshes from an XCT scan of the plastic explosive surrogate material system F50 sand and Kel-F. Resulting segmented particles are analyzed by comparison with a typical size distribution of F50 sand.

#### 7.2 Conclusions

The work presented in Chapters 3 through 6 each address one of the research questions posed in Chapter 1. Conclusions for the work presented in each chapter are presented below in the context of the corresponding research question which drove the work.

##### 7.2.1 Relating X-Radiography to Composition

*How can in-situ x-radiography be used in conjunction with other methods of analysis to infer composition of an Al-Ag alloy during solidification?*

Chapter 3 proposed a proof-of-concept, multimodal approach to solidification analysis of an Al-Ag alloy system combining three separate methods of investigation. In-situ x-radiography measured changing grayscale intensities through the sample volume during solidification, EDS measured composition at the surface of the as-solidified sample, and the calculation of a Scheil solidification model which provided compositional information throughout a theoretical solidification. Aligning the final x-radiograph with the SEM image showing the track of the track of the EDS scan allowed for an intensity profile to be generated along the same solidified structure. Even though the radiography captured the entire thickness of the sample and the EDS measured only the surface, the two datasets showed similar trends in multiple regions in the sample. These trends show that a mapping from x-ray intensity to composition could be possible without performing an explicit calibration experiment. The Scheil solidification model calculated the composition of the solid forming at different temperatures, simulating the solidification of an alloy system matching that of the sample. The resulting data was plotted as solid composition versus fraction solid. This data was fit to the manually annotated radiographs to create a mapping from the image number to solid composition. The as-measured data fits reasonably well at the beginning of the solidification, though after about 75% of the sample solidified, the fraction solid as-measured was larger than the values calculated from the Scheil model. A potential cause for this discrepancy was that manually annotated solidifying structures, used to calculate solid fraction, were not completely solidified through the entire thickness of the sample as assumed. While this work did not make direct correlations between these three analysis methods, the comparisons provided more insight into the solidification than either of the three methods would have provided on its own. With more experiments performed, the relationships between the different methods could be identified to more confidently infer composition from the in-situ x-radiography intensities.

### **7.2.2 Procedural Analysis of Melt Pool Tracking**

*How successful is an image processing procedure at automating the identification, tracking, and velocity calculation of solid-liquid interfaces during in-situ solidification experiments?*

Chapter 4 explored the efficacy of automated procedures for identifying, tracking, and calculating the velocity of metallic solidification processes observed in situ. Two types of procedures were developed and tested: the first for synchrotron x-radiography monitoring of AM simulator experiments and the second for DTEM monitoring of thin film, rapid solidification experiments. The results from each procedure were compared to

manual measurements. In the AM simulator experiments, the automated procedure was reasonably successful identifying the interfaces when compared to the manual measurements. For two of the three experiments on which the procedure was applied, the mean solidification velocity calculated from the detected interfaces was drastically different than the manually measured velocities, but the median values were similar. The average deviation from the manual mean velocity was also higher for the detected data, but half the detected data were within the average deviation for one of the experiments, and the majority for the other experiment, which suggests that the error in the detected measurements was mainly due to large outliers from detected noise. In the third experiment, the mean detected velocity was the same as the mean manual velocity, but the median velocities differed. This suggests that the deviations were balanced above and below the mean. Like the previous experiments, the average deviation from the manual mean was still higher for the detected velocities than for the manual measurements, but the majority of detected data was within the average deviation from the manual mean, suggesting once again that the majority of the error comes from the outliers in the data.

In the rapid solidification experiments, the outlined procedure is able to accurately track the interface throughout the entire solidification process according to comparisons with the manual measurements. The velocity calculations were also in agreement with the manual calculations for the majority of the experiments, with the exception of the end of the third experiment where the melt pool much smaller and disappears before the last frame of the experiment. One reason the rapid solidification procedure performed better than the AM simulator procedure is because the melt pools generally stayed large enough to not be confused with noise (besides the end of the third experiment). The rapid solidification procedure also incorporated an optimization step. If something similar was included for the AM simulator experiment, the results might have been less sensitive to noise.

Beyond comparisons to manual results, there are additional benefits to the development of these automated procedures. Automated procedures allow for more consistent results than manual measurements. A procedure carried out by a computer will be performed the same way on any given dataset, regardless of the experience or biases of the user executing the method. The process of developing automated procedures may also be beneficial to the scientific process. When explicitly writing out a routine such that it can be interpreted by a computer, researchers may more closely consider their methods in a way uncovers previous unnoticed bias. Less justified analysis steps may be left out when a routine is made more explicit. Finally, automatic methods

may encourage researchers to test changes in analysis methods which could lead to more refined results. One barrier to refining analysis methods is the effort and time required to test changes to these methods. Especially when results are not guaranteed to improve, high time and effort barriers may prevent these results from being tested. This can lead to analysis methods that deliver "good enough" results rather than analysis methods that are proven to be superior to other methods. However, with automated procedures, more iterations of analysis methods can be tested without the same time and effort commitment. This increases the chance that improvements to the analysis method can be discovered to improve results that otherwise may not have been tested.

Overall, the success of image processing procedures in identifying, tracking, and calculating the velocity of solid-liquid interfaces was shown to be mixed when the measure of success is the accuracy related to manually determined values. The accuracy in the procedure which included an optimization step (thin film rapid solidification experiments) outperformed the procedure which did not include any optimization (AM simulator experiments). This suggests that incorporating an optimization step should be considered in development of similar procedures. Other benefits may include quantifying consistency, bias reduction, and time/effort reduction for tuning results.

### **7.2.3 Segmentation of Irregular and Tightly Clustered Particles**

*How can the segmentation of multi-sized, irregularly-shaped, and tightly-clustered particles be improved?*

Chapter 5 proposed a method for improving the segmentation of irregularly distributed features (e.g., sand grains) that are not accurately segmented using methods found in literature. A common method in literature for segmenting features of an image is the application of a watershed algorithm. Watershed segmentation enables features in contact with one another to be segmented as long as the size and shape of the features are roughly uniform. Even when the shapes are nonuniform, watershed segmentation can return accurate segmentation results as long as the features are roughly the same size. An adjustment to the routine can also be made that allows for multi-sized features to be segmented from one another, solving either over- or under-segmentation in these cases, as described in the introduction of Chapter 5. However, when features are not uniform in size or shape, the typical watershed segmentation does not yield accurate results. This inaccuracy is amplified when particles are clustered tightly enough to be misrepresented as even more irregular particles. The irregularity causes the resulting segmentation to contain a combination of over- and under-segmentation, which

cannot be adjusted by methods in literature.

This chapter presented an extension to typical watershed segmentation by including additional preprocessing steps which would intentionally generate over-segmented results. These resulting regions were then subject to a novel algorithm for merging regions based on edge strength between neighboring regions. This proposed algorithm relied on a Delaunay triangulation that identified neighboring regions across varying distances. These varying distances allowed for multi-sized features to be considered. The algorithm also relied on an assumption that neighboring regions adequately segmented would see an increase in intensity in an edge-amplified image. By assuming these spikes would not occur between two under-segmented features, the lack of presence of these spikes was used as a merging condition for neighboring regions. This method was tested on a 2D image taken from a 3D XCT scan of material system consisting of irregularly sized and shaped sand grains tightly clustered with a polymer binder. The results of the merged region segmentation were compared to a manual segmentation of the same image, along with the results from a typical watershed segmentation. The merged region segmentation achieved a fit of 89.02%, a 6.93% improvement from the typical watershed segmentation.

#### 7.2.4 Generating Image-Based Modeling Geometries

*How can a workflow be designed to extract 3D geometries from x-ray computed tomography data such that the geometry of a physical sample can be reproduced digitally for use as initial conditions in an image-based physics simulation?*

Chapter 6 presented *Segmentflow*, a Python package for building and/or executing segmentation workflows to extract information from 3D datasets like XCT scans. The goal of these workflows is to create physically informed geometries for use in image-based physics simulations. *Segmentflow* has tools for loading data and segmentation parameters, preprocessing images to improve contrast and/or reduce noise, performing semantic segmentation to classify scan data according to material type/class, performing instance segmentation by watershed algorithm, converting voxel data to surface meshes, and postprocessing surface meshes to fit the needs of a particular simulation/user.

Functionality of *Segmentflow* was presented by demonstrating a segmentation workflow for generating simulation-ready surface meshes from an XCT scan of a F50 sand and Kel-F binder system used to approximate the mechanical properties of high explosives. The XCT data was loaded with *Segmentflow* and preprocessed to improve the contrast. The sample was expected to have three classes of material represented in

the images: void, binder, and sand grain. Threshold values were calculated to segment the volume into these three classes, and a binary image was created to distinguish the sand grain class from the rest of the classes. This binary representation was used to calculate a set of markers which will each seed a watershed segmentation for a total of five separate segmentations. The resulting segmented particles from each of these segmentations were analyzed to calculate a size distribution calculated in two ways: from the sphere of equivalent volume and from the aspect ratio of the bounding box. The segmentation that produced particles with the smallest total accumulated error summed across both size distributions was assumed to be the most accurate. These segmented particles were converted to surface meshes, and all 41553 surface meshes were visualized together to show the extent of the sample. One of the particle surface meshes was used to show an example of mesh postprocessing. The example surface mesh, originally consisting of 1524 triangles, was visualized side by side with the same surface mesh after a series of postprocessing steps. The first step shows the particle after Laplacian smoothing. This retains the number of triangles, but results in a surface mesh that appears less blocky. The next step shows the surface mesh after simplifying past 200 triangles to a total of 190 triangles. The final step shows the surface mesh reduced past 20 triangles to a total of only 10 triangles. This series of postprocessing steps shows how the surface mesh can be reduced drastically. This is an important capability of *Segmentflow* as it gives the user the power to create simulation geometry that can have a range of complexity, depending on the desired scale of the simulation.

## CHAPTER 8

### RECOMMENDATIONS FOR FUTURE WORK

The work presented in this thesis answered questions that were sought at the beginning of the project. In the process, however, more questions were discovered. These discoveries provide opportunities to compound the results presented in this thesis. This chapter addresses these opportunities by providing recommendations for future work.

#### 8.1 Optimization of AM Simulator Detection

In Chapter 4, two procedures were presented detect the solid-liquid interface in a solidifying metal sample. The procedure developed first was for AM simulator experiments and was designed to detect semi-elliptical melt pools. The second procedure, developed after the first, was designed to detect elliptical melt pools in thin film, rapid solidification experiments. The procedures were similar, but the AM simulator procedure detected the bounding box of the semi-elliptical melt pools whereas the rapid solidification experiment optimized the fit of an ellipse to the elliptical melt pool. The rapid solidification procedure performed better than the AM simulator procedure. The incorporation of fit optimization may not have been the only reason for the improved performance, but incorporating some kind of an optimization step into the AM simulator would be a good place to start improving the procedure.

The optimization included in the rapid solidification procedure optimized the fit of an ellipse to the melt pool. To bring optimization to the AM simulator procedure, a shape could similarly be fit to the data. However, the fit of the ellipse was optimized by minimizing a cost function that incorporated the mismatch of the ellipse with a binary image representation of the experiment. A cost function to be optimized to improve the fit of the AM simulator could include many different parameters besides fit mismatch. Other parameters could include detected melt pool aspect ratio, difference in size with the melt pool of the previous frame, difference in location of with previous melt pool, location relative to the center of the image, or location relative to the top of the sample. Exploring the optimization using some of these parameters would make for an interesting study that is likely to achieve promising results based on the number of possibilities alone.

## 8.2 Extension of Edge Strength Corrected Segmentation

In Chapter 5, a method was presented to correct the segmentation of irregularly-shaped, multi-sized, and tightly-clustered particles. The implementation of this algorithm was successful, however the presented routine was only applied in two dimensions. The image on which this routine was tested is itself from a 3D dataset. This displays the biggest opportunity to be pursued following this work: adapting this routine to work with 3D data. The watershed segmentation and Delaunay triangulation algorithms leveraged for this procedure can both function in three dimensions, so the main focus would need to adapt the region merging algorithm to 3D. A potential obstacle is the increase in the number of neighbors for marker will in the adaption to 3D. This may require optimization of the merging algorithm, depending on the size of the datasets to which the procedure is applied.

Another path for continued study related to this method is further development of the criteria defining detected edges. The method as it stands has two conditions for detecting edges: a simple threshold dependent on the maximum intensity of the edge-amplified image and the location of any detected edges along the line connecting two markers/regions. Perhaps by applying more thorough signal processing techniques, a more robust criteria could be developed that wouldn't require fine-tuning on an image-to-image basis that is likely necessary with the current algorithms. A study on either or both of these extensions to this method would be interesting and useful, especially for the application of image-based simulations as discussed in Chapter 6.

## 8.3 Additional Segmentation Functionality for Segmentflow

Chapter 6 presented *Segmentflow*, a Python package for developing and/or executing segmentation workflows to create geometry that could be used as initial conditions in a physics simulation. *Segmentflow* is a flexible software library that has been steadily increasing the more it is used and the more diverse its user base has become. There are many additional features that could be added, but some of the most scientifically interesting include additional methods for determining particle size distributions and the ability to merge segmentation results. In Chapter 6, size distributions were calculated for the segmented particles by binning particles by diameter as determined by either assuming the particle was a sphere or using the maximum bounds of a particle. The sphere method is obviously limited because most particles are not actually spheres. For very blocky particles, this may be an underestimate of size, but for most particles, this will be a overestimate of size since the particles may have volume distributed

preferentially along one or two axes rather than all three equally. The limitations of the bounding box method, which determines the size based on the aspect ratio of the smallest box a particle could fit in does a better job of not overestimating size based on volume distribution, however, there are further limitations related to how a particle is oriented within the box. The box is constrained to the axes of the voxels, so if an oblong particle is oriented significantly askew to any of these axes, the bounding box will be much larger than the particle. A better method for approximating the size distribution of segmented particles would be to fit a tightly fitting ellipsoid around each particle, however this is not currently possible in *Segmentflow*.

As discussed in Chapter 5, segmenting irregular particles is difficult because if results are a mix of over- and under-segmented, the segmentation cannot be improved in both directions, which was the motivation for the Chapter 5 in the first place. Perhaps rather than trying to correct results from watershed segmentation, methods of segmentation could be investigated. Many of the incorrect results that can result from watershed segmentation have complex, unnatural-looking forms. Rather than try to correct these forms after segmentation, a new segmentation method might be able to avoid these forms in the first place. One potential path for this kind of a study would be to investigate a method to incorporate minimization of surface energy into a segmentation algorithm.

## REFERENCES

- [1] W. C. Röntgen. On a new kind of rays. *Science*, 3:227–231, 1896.
- [2] E.W.J. Miller and J. Beech. In-situ radiographic observations of alloy solidification. *Metallography*, 5:298–300, 1972.
- [3] E. W.J. Miller, M. P. Stephenson, and J. Beech. A technique for the direct observation of alloy solidification. *Journal of Physics E: Scientific Instruments*, 8: 33, 1975.
- [4] G. R. Cappleman. Dynamic x-radiography of liquid sodium. *Journal of Materials Science 1982* 17:8, 17:2208–2212, 1982.
- [5] S. Rondot, J. Cazaux, O. Aaboubi, J. P. Chopart, and A. Olivier. Following ion diffusion in solution. *Science*, 263:1739–1741, 1994.
- [6] P. G. Barber, R. F. Berry, W. J. Debnam, A. L. Fripp, G. Woodell, and R. T. Simchick. Growth rates and interface shapes in germanium and lead tin telluride observed in-situ, real-time in vertical bridgman furnaces. *Journal of Crystal Growth*, 147:83–90, 1995.
- [7] J. N. Koster, T. Seidel, and R. Derebail. A radioscopyc technique to study convective fluid dynamics in opaque liquid metals. *Journal of Fluid Mechanics*, 343:29–41, 1997.
- [8] Peter A. Curreri and William F. Kaukler. Real-time x-ray transmission microscopy of solidifying al-in alloys. *Metallurgical and Materials Transactions A* 1996 27:3, 27: 801–808, 1996.
- [9] William F. Kaukler, Franz Rosenberger, and Peter A. Curreri. In situ studies of precipitate formationin al-pb monotectic solidification by x-ray transmission microscopy. *Metallurgical and Materials Transactions A*, 28:1705–1710, 1997.
- [10] R. H. Mathiesen, L. Arnberg, F. Mo, T. Weitkamp, and A. Snigirev. Time resolved x-ray imaging of dendritic growth in binary alloys. *Physical Review Letters*, 83: 5062–5065, 1999.
- [11] A. R. Lang. The projection topograph: a new method in x-ray diffraction microradiography. *Acta Crystallographica*, 12:249–250, 1959.

- [12] Jun Ichi Chikawa, Isao Fujimoto, and Takao Abe. X-ray topographic observation of moving dislocations in silicon crystals. *Applied Physics Letters*, 21:295, 1972.
- [13] Jun Ichi Chikawa. Technique for the video display of x-ray topographic images and its application to the study of crystal growth. *Journal of Crystal Growth*, 24–25: 61–68, 1974.
- [14] Tatsumasa Kobayashi and Toru Imura. In situ heating device for real time x-ray topography on crystal growth from the melt. *Japanese Journal of Applied Physics*, 23:L632–L634, 1984.
- [15] W. Yamada and T. Matsumiya. In situ observation of solidification of silicon steel by synchrotron radiation x-ray topography, 1987.
- [16] G. Grange, J. Gastaldi, C. Jourdon, and B. Billia. Real-time topography of microstructures in a binary alloy. *Synchrotron Radiation News*, 7:12–15, 1994.
- [17] Ragnvald H Mathiesen, Lars Arnberg, Kjell Ramsøskar, Timm Weitkamp, Christoph Rau, and Anatoly Snigirev. Time-resolved x-ray imaging of aluminum alloy solidification processes. *Metallurgical and Materials Transactions B*, 33B: 613–623, 2002.
- [18] C. Rakete, C. Baumbach, A. Goldschmidt, D. Samberg, C. G. Schroer, F. Breede, C. Stenzel, G. Zimmermann, C. Pickmann, Y. Houltz, C. Lockowandt, O. Svenonius, P. Wiklund, and R. H. Mathiesen. Compact x-ray microradiograph for in situ imaging of solidification processes: Bringing in situ x-ray micro-imaging from the synchrotron to the laboratory. *Review of Scientific Instruments*, 82: 105108, 2011.
- [19] H. Nguyen-Thi, G. Reinhart, G. Salloum Abou Jaoude, R.H. Mathiesen, G. Zimmermann, Y. Houltz, D. Voss, A. Verga, D.J. Browne, and A.G. Murphy. Xrmon-gf: A novel facility for solidification of metallic alloys with in situ and time-resolved x-ray radiographic characterization in microgravity conditions. *Journal of Crystal Growth*, 374:23–30, 2013.
- [20] H. Nguyen Thi, H. Jamgotchian, J. Gastaldi, J. Härtwig, T. Schenk, H. Klein, B. Billia, J. Baruchel, and Y. Dabo. Preliminary in situ and real-time study of directional solidification of metallic alloys by x-ray imaging techniques. *Journal of Physics D: Applied Physics*, 36:A83, 2003.
- [21] Naji S. Husseini, Divine P. Kumah, Jian Z. Yi, Christopher J. Torbet, Dohn A. Arms, Eric M. Dufresne, Tresa M. Pollock, J. Wayne Jones, and Roy Clarke. Mapping single-crystal dendritic microstructure and defects in nickel-base superalloys with synchrotron radiation. *Acta Materialia*, 56:4715–4723, 2008.

- [22] Amy J. Clarke, Damien Tourret, Seth D. Imhoff, Paul J. Gibbs, Kamel Fezzaa, Jason C. Cooley, Wah Keat Lee, Alex Deriy, Brian M. Patterson, Pallas A. Papin, Kester D. Clarke, Robert D. Field, and James L. Smith. X-ray imaging and controlled solidification of al-cu alloys toward microstructures by design. *Advanced Engineering Materials*, 17:454–459, 2015.
- [23] W. J. Sames, F. A. List, S. Pannala, R. R. Dehoff, and S. S. Babu. The metallurgy and processing science of metal additive manufacturing. *International Materials Reviews*, 61:315–360, 2016.
- [24] T. DebRoy, H. L. Wei, J. S. Zuback, T. Mukherjee, J. W. Elmer, J. O. Milewski, A. M. Beese, A. Wilson-Heid, A. De, and W. Zhang. Additive manufacturing of metallic components - process, structure and properties. *Progress in Materials Science*, 92:112–224, 2018.
- [25] Ian Gibson, David Rosen, and Brent Stucker. Powder bed fusion processes. *Additive Manufacturing Technologies*, pages 107–145, 2015.
- [26] S. Sun, Milan Brandt, and M. Easton. Powder bed fusion processes: An overview. *Laser Additive Manufacturing: Materials, Design, Technologies, and Applications*, pages 55–77, 2017.
- [27] Ian Gibson, David Rosen, and Brent Stucker. Directed energy deposition processes. *Additive Manufacturing Technologies*, pages 245–268, 2015.
- [28] W. E. King, A. T. Anderson, R. M. Ferencz, N. E. Hodge, C. Kamath, S. A. Khairallah, and A. M. Rubenchik. Laser powder bed fusion additive manufacturing of metals; physics, computational, and materials challenges. *Applied Physics Reviews*, 2:041304, 2015.
- [29] Cang Zhao, Kamel Fezzaa, Ross W. Cunningham, Haidan Wen, Francesco De Carlo, Liyan Chen, Anthony D. Rollett, and Tao Sun. Real-time monitoring of laser powder bed fusion process using high-speed x-ray imaging and diffraction. *Scientific Reports*, 7:1–11, 2017.
- [30] Ross Cunningham, Cang Zhao, Niranjan Parab, Christopher Kantzos, Joseph Pauza, Kamel Fezzaa, Tao Sun, and Anthony D. Rollett. Keyhole threshold and morphology in laser melting revealed by ultrahigh-speed x-ray imaging. *Science*, 363:849–852, 2019.
- [31] Chu Lun Alex Leung, Sebastian Marussi, Robert C. Atwood, Michael Towrie, Philip J. Withers, and Peter D. Lee. In situ x-ray imaging of defect and molten pool dynamics in laser additive manufacturing. *Nature Communications*, 9:1–9, 2018.

- [32] Qilin Guo, Cang Zhao, Minglei Qu, Lianghua Xiong, S. Mohammad H. Hojjatzadeh, Luis I. Escano, Niranjan D. Parab, Kamel Fezzaa, Tao Sun, and Lianyi Chen. In-situ full-field mapping of melt flow dynamics in laser metal additive manufacturing. *Additive Manufacturing*, 31:100939, 2020.
- [33] Aiden A. Martin, Nicholas P. Calta, Saad A. Khairallah, Jenny Wang, Phillip J. Depond, Anthony Y. Fong, Vivek Thampy, Gabe M. Guss, Andrew M. Kiss, Kevin H. Stone, Christopher J. Tassone, Johanna Nelson Weker, Michael F. Toney, Tony van Buuren, and Manyalibo J. Matthews. Dynamics of pore formation during laser powder bed fusion additive manufacturing. *Nature Communications* 2019 10:1, 10:1–10, 2019.
- [34] Qilin Guo, Cang Zhao, Luis I. Escano, Zachary Young, Lianghua Xiong, Kamel Fezzaa, Wes Everhart, Ben Brown, Tao Sun, and Lianyi Chen. Transient dynamics of powder spattering in laser powder bed fusion additive manufacturing process revealed by in-situ high-speed high-energy x-ray imaging. *Acta Materialia*, 151: 169–180, 2018.
- [35] Qilin Guo, Cang Zhao, Minglei Qu, Lianghua Xiong, Luis I. Escano, S. Mohammad H. Hojjatzadeh, Niranjan D. Parab, Kamel Fezzaa, Wes Everhart, Tao Sun, and Lianyi Chen. In-situ characterization and quantification of melt pool variation under constant input energy density in laser powder bed fusion additive manufacturing process. *Additive Manufacturing*, 28:600–609, 2019.
- [36] Niranjan D. Parab, Lianghua Xiong, Qilin Guo, Zherui Guo, Cody Kirk, Yizhou Nie, Xianghui Xiao, Kamel Fezzaa, Wesley Everheart, Weinong W. Chen, Lianyi Chen, and Tao Sun. Investigation of dynamic fracture behavior of additively manufactured al-10si-mg using high-speed synchrotron x-ray imaging. *Additive Manufacturing*, 30:100878, 2019.
- [37] Ross Cunningham, Sneha P. Narra, Tugce Ozturk, Jack Beuth, and A. D. Rollett. Evaluating the effect of processing parameters on porosity in electron beam melted ti-6al-4v via synchrotron x-ray microtomography. *JOM*, 68:765–771, 2016.
- [38] Ross Cunningham, Sneha P. Narra, Colt Montgomery, Jack Beuth, and A. D. Rollett. Synchrotron-based x-ray microtomography characterization of the effect of processing variables on porosity formation in laser power-bed additive manufacturing of ti-6al-4v. *JOM*, 69:479–484, 2017.
- [39] Anton du Plessis. Effects of process parameters on porosity in laser powder bed fusion revealed by x-ray tomography. *Additive Manufacturing*, 30:100871, 2019.

- [40] Greet Kerckhofs, Grzegorz Pyka, Maarten Moesen, Simon Van Bael, Jan Schrooten, and Martine Wevers. High-resolution microfocus x-ray computed tomography for 3d surface roughness measurements of additive manufactured porous materials. *Advanced Engineering Materials*, 15:153–158, 2013.
- [41] Anton du Plessis, Philip Sperling, Andre Beerlink, Lerato Tshabalala, Shaik Hoosain, Ntombi Mathe, and Stephan G. le Roux. Standard method for microct-based additive manufacturing quality control 1: Porosity analysis. *MethodsX*, 5:1102–1110, 2018.
- [42] Curtis T. Rueden, Johannes Schindelin, Mark C. Hiner, Barry E. DeZonia, Alison E. Walter, Ellen T. Arena, and Kevin W. Eliceiri. Imagej2: Imagej for the next generation of scientific image data. *BMC Bioinformatics*, 18:1–26, 2017.
- [43] Nicholas Hagai Sofroniew, Talley Lambert, Kira Evans, Juan Nunez-Iglesias, Grzegorz Bokota, Gonzalo Peña-Castellanos, Philip Winston, Kevin Yamauchi, Matthias Bussonnier, Draga Doncila Pop, Ziyang Liu, ACS, Pam, alisterburt, and Genevi Buckley. napari/napari: 0.4.12rc2.
- [44] Nobuyuki Otsu. A threshold selection method from gray-level histograms. *IEEE Transaction on Systems, Man, and Cybernetics*, SMC-9, 1979.
- [45] S. Beucher and C. Lantuejoul. Use of watersheds in contour detections. *Proceedings of the International Workshop on Image Processing*, 1979.
- [46] Pierre Soille and Luc M. Vincent. Determining watersheds in digital pictures via flooding simulations. *Visual Communications and Image Processing '90: Fifth in a Series*, 1360:240–250, 1990.
- [47] Pierre J. Soille and Marc M. Ansoult. Automated basin delineation from digital elevation models using mathematical morphology. *Signal Processing*, 20: 171–182, 1990.
- [48] Luc Vincent and Pierre Soille. Watersheds in digital spaces: An efficient algorithm based on immersion simulations. *IEEE TRANSACTIONS ON PATTERN ANALYSIS AND MACHINE INTELLIGENCE*, 13:583, 1991.
- [49] Alina N. Moga and Moncef Gabbouj. Parallel marker-based image segmentation with watershed transformation. *Journal of Parallel and Distributed Computing*, 51: 27–45, 1998.
- [50] Kodimela Parvati, B. S. Prakasa Rao, and M. Mariya Das. Image segmentation using gray-scale morphology and marker-controlled watershed transformation. *Discrete Dynamics in Nature and Society*, 2008, 2008.

- [51] C. Wählby, I. M. Sintorn, F. Erlandsson, G. Borgefors, and E. Bengtsson. Combining intensity, edge and shape information for 2d and 3d segmentation of cell nuclei in tissue sections. *Journal of Microscopy*, 215:67–76, 2004.
- [52] Jierong Cheng and Jagath C. Rajapakse. Segmentation of clustered nuclei with shape markers and marking function. *IEEE Transactions on Biomedical Engineering*, 56:741–748, 2009.
- [53] Hyoungkwan Kim, Carl T. Haas, Alan F. Rauch, and Craig Browne. 3d image segmentation of aggregates from laser profiling. *Computer-Aided Civil and Infrastructure Engineering*, 18:254–263, 2003.
- [54] Sophie Burgmann, Michael Godehardt, Katja Schladitz, and Wolfgang Breit. Separation of sand and gravel particles in 3d images using the adaptive h-extrema transform. *Powder Technology*, 404:117468, 2022.
- [55] Paul J. Tadrous. On the concept of objectivity in digital image analysis in pathology. *Pathology*, 42:207–211, 2010.
- [56] Thomas Kluyver, Benjamin Ragan-Kelley, Fernando Pérez, Brian Granger, Matthias Bussonnier, Jonathan Frederic, Kyle Kelley, Jessica Hamrick, Jason Grout, Sylvain Corlay, Paul Ivanov, Damián Avila, Safia Abdalla, and Carol Willing. Jupyter notebooks—a publishing format for reproducible computational workflows. pages 87–90, 2016. ISBN 9781614996484.
- [57] M. J.M.M. Hoeijmakers, D. A. Silva Soto, I. Waechter-Stehle, M. Kasztelnik, J. Weese, D. R. Hose, and F. N.van de Vosse. Estimation of valvular resistance of segmented aortic valves using computational fluid dynamics. *Journal of Biomechanics*, 94:49–58, 2019.
- [58] Jiayao Zhang, George A. Sandison, Jayathi Y. Murthy, and Lisa X. Xu. Numerical simulation for heat transfer in prostate cancer cryosurgery. *Journal of Biomechanical Engineering*, 127:279–294, 2005.
- [59] Ming Chao, Yaoqin Xie, Eduardo G. Moros, Quynh Thu Le, and Lei Xing. Image-based modeling of tumor shrinkage in head and neck radiation therapy. *Medical Physics*, 37:2351–2358, 2010.
- [60] Matthieu Lê, Jan Unkelbach, Nicholas Ayache, and Hervé Delingette. Sampling image segmentations for uncertainty quantification. *Medical Image Analysis*, 34: 42–51, 2016.

- [61] Esmaeel Jafargholi Rangraz, Walter Coudyzer, Geert Maleux, Kristof Baete, Christophe M. Deroose, and Johan Nuyts. Multi-modal image analysis for semi-automatic segmentation of the total liver and liver arterial perfusion territories for radioembolization. *EJNMMI Research*, 9:1–21, 2019.
- [62] J. Christoph, M. Chebbok, C. Richter, J. Schröder-Schetelig, P. Bittihn, S. Stein, I. Uzelac, F. H. Fenton, G. Hasenfuß, R. F. Gilmour, and S. Luther. Electromechanical vortex filaments during cardiac fibrillation. *Nature 2018* 555:7698, 555:667–672, 2018.
- [63] Leonid P. Savchenko, Lucie Bard, Thomas P. Jensen, James P. Reynolds, Igor Kraev, Nikolay Medvedev, Michael G. Stewart, Christian Henneberger, and Dmitri A. Rusakov. Disentangling astroglial physiology with a realistic cell model in silico. *Nature Communications 2018* 9:1, 9:1–15, 2018.
- [64] Yutaro Kashiwagi, Takahito Higashi, Kazuki Obashi, Yuka Sato, Noboru H. Komiya, Seth G.N. Grant, and Shigeo Okabe. Computational geometry analysis of dendritic spines by structured illumination microscopy. *Nature Communications 2019* 10:1, 10:1–14, 2019.
- [65] T. Hutzenlaub, S. Thiele, N. Paust, R. Spotnitz, R. Zengerle, and C. Walchshofer. Three-dimensional electrochemical li-ion battery modelling featuring a focused ion-beam/scanning electron microscopy based three-phase reconstruction of a licoo<sub>2</sub> cathode. *Electrochimica Acta*, 115:131–139, 2014.
- [66] Hector Mendoza, Scott A. Roberts, Victor E. Brunini, and Anne M. Grillet. Mechanical and electrochemical response of a licoo<sub>2</sub> cathode using reconstructed microstructures. *Electrochimica Acta*, 190:1–15, 2016.
- [67] Simon Müller, Jens Eller, Martin Ebner, Chris Burns, Jeff Dahn, and Vanessa Wood. Quantifying inhomogeneity of lithium ion battery electrodes and its influence on electrochemical performance. *Journal of The Electrochemical Society*, 165:A339–A344, 2018.
- [68] Xuekun Lu, Antonio Bertei, Donal P. Finegan, Chun Tan, Sohrab R. Daemi, Julia S. Weaving, Kieran B. O'Regan, Thomas M.M. Heenan, Gareth Hinds, Emma Kendrick, Dan J.L. Brett, and Paul R. Shearing. 3d microstructure design of lithium-ion battery electrodes assisted by x-ray nano-computed tomography and modelling. *Nature Communications 2020* 11:1, 11:1–13, 2020.
- [69] Andy Vanaerschot, Francesco Panerai, Alan Cassell, Stepan V. Lomov, Dirk Vandepitte, and Nagi N. Mansour. Stochastic characterisation methodology for 3-d textiles based on micro-tomography. *Composite Structures*, 173:44–52, 2017.

- [70] J. Michael L. MacNeil, Daniela M. Ushizima, Francesco Panerai, Nagi N. Mansour, Harold S. Barnard, and Dilworth Y. Parkinson. Interactive volumetric segmentation for textile micro-tomography data using wavelets and nonlocal means. *Statistical Analysis and Data Mining: The ASA Data Science Journal*, 12:338–353, 2019.
- [71] Federico Semeraro, Joseph C. Ferguson, Marcos Acin, Francesco Panerai, and Nagi N. Mansour. Anisotropic analysis of fibrous and woven materials part 2: Computation of effective conductivity. *Computational Materials Science*, 186: 109956, 2021.
- [72] Gennadiy Nikishkov, Yuri Nikishkov, and Andrew Makeev. Finite element mesh generation for composites with ply waviness based on x-ray computed tomography. *Advances in Engineering Software*, 58:35–44, 2013.
- [73] Michael W. Czabaj, Mark L. Riccio, and William W. Whitacre. Numerical reconstruction of graphite/epoxy composite microstructure based on sub-micron resolution x-ray computed tomography. *Composites Science and Technology*, 105: 174–182, 2014.
- [74] R. M. Sencu, Z. Yang, Y. C. Wang, P. J. Withers, C. Rau, A. Parson, and C. Soutis. Generation of micro-scale finite element models from synchrotron x-ray ct images for multidirectional carbon fibre reinforced composites. *Composites Part A: Applied Science and Manufacturing*, 91:85–95, 2016.
- [75] S. M. Shah, F. Gray, J. P. Crawshaw, and E. S. Boek. Micro-computed tomography pore-scale study of flow in porous media: Effect of voxel resolution. *Advances in Water Resources*, 95:276–287, 2016.
- [76] Michael C. Krygier, Tyler LaBonte, Carianne Martinez, Chance Norris, Krish Sharma, Lincoln N. Collins, Partha P. Mukherjee, and Scott A. Roberts. Quantifying the unknown impact of segmentation uncertainty on image-based simulations. *Nature Communications 2021* 12:1, 12:1–11, 2021.
- [77] C. Gus Becker, Damien Tourret, Doug Smith, Brian Rodgers, Seth Imhoff, John Gibbs, James Hunter, Michelle Espy, Kester Clarke, and Amy Clarke. Integrating in situ x-ray imaging, energy dispersive spectroscopy, and calculated phase diagram analysis of solute segregation during solidification of an al-ag alloy. *JOM*, 9 2021.
- [78] Silvère Akamatsu and Henri Nguyen-Thi. In situ observation of solidification patterns in diffusive conditions. *Acta Materialia*, 108:325–346, 4 2016.
- [79] Ashwin J. Shahani, Xianghui Xiao, Erik M. Lauridsen, and Peter W. Voorhees. Characterization of metals in four dimensions.  
<http://mc.manuscriptcentral.com/tmrl>, 8:462–476, 2020.

- [80] Shyamprasad Karagadde, Chu Lun, Alex Leung, and Peter D Lee. materials progress on in situ and operando x-ray imaging of solidification processes. 2021.
- [81] Joseph T. McKeown, Amy J. Clarke, and Jörg M.K. Wiezorek. Imaging transient solidification behavior, 2020.
- [82] R. H. Mathiesen, L. Arnberg, F. Mo, T. Weitkamp, and A. Snigirev. Time resolved x-ray imaging of dendritic growth in binary alloys. *Physical Review Letters*, 83: 5062–5065, 1999.
- [83] C. Rakete, C. Baumbach, A. Goldschmidt, D. Samberg, C. G. Schroer, F. Breede, C. Stenzel, G. Zimmermann, C. Pickmann, Y. Houltz, C. Lockowandt, O. Svenonius, P. Wiklund, and R. H. Mathiesen. Compact x-ray microradiograph for in situ imaging of solidification processes: Bringing in situ x-ray micro-imaging from the synchrotron to the laboratory. *Review of Scientific Instruments*, 82: 105108, 2011.
- [84] B. J. Heismann, J. Leppert, and K. Stierstorfer. Density and atomic number measurements with spectral x-ray attenuation method. *Journal of Applied Physics*, 94:2073, 2003.
- [85] K. A. Jackson and J. D. Hunt. Transparent compounds that freeze like metals. *Acta Metallurgica*, 13:1212–1215, 1965.
- [86] MP Stephenson and J Beech. In situ observations of solute redistribution during solidification. *Solidification and Casting of Metals*, pages 34–38, 1977.
- [87] A. G. Murphy, J. Li, O. Janson, A. Verga, and D. J. Browne. Microgravity and hypergravity observations of equiaxed solidification of al-cu alloys using in situ x-radiography recorded in real-time on board a parabolic flight. *Materials Science Forum*, 790-791:52–58, 2014.
- [88] A. Griesche, B. Zhang, E. Solórzano, and F. Garcia-Moreno. Note: X-ray radiography for measuring chemical diffusion in metallic melts. *Review of Scientific Instruments*, 81:056104, 2010.
- [89] Insung Han, Xianghui Xiao, and Ashwin J. Shahani. Probing the growth and melting pathways of a decagonal quasicrystal in real-time. *Scientific Reports* 2017 7:1, 7:1–10, 2017.
- [90] D. Ruvalcaba, R.H. Mathiesen, D.G. Eskin, L. Arnberg, and L. Katgerman. In situ observations of dendritic fragmentation due to local solute-enrichment during directional solidification of an aluminum alloy. *Acta Materialia*, 55:4287–4292, 2007.

- [91] A. Bogno, H. Nguyen-Thi, A. Buffet, G. Reinhart, B. Billia, N. Mangelinck-Noël, N. Bergeon, J. Baruchel, and T. Schenk. Analysis by synchrotron x-ray radiography of convection effects on the dynamic evolution of the solid–liquid interface and on solute distribution during the initial transient of solidification. *Acta Materialia*, 59:4356–4365, 2011.
- [92] A. Bogno, H. Nguyen-Thi, G. Reinhart, B. Billia, and J. Baruchel. Growth and interaction of dendritic equiaxed grains: In situ characterization by synchrotron x-ray radiography. *Acta Materialia*, 61:1303–1315, 2013.
- [93] M. Becker, S. Klein, and F. Kargl. In-situ solute measurements with a laboratory polychromatic microfocus x-ray source during equiaxed solidification of an al-ge alloy. *Scripta Materialia*, 124:34–37, 2016.
- [94] Maike Becker, Laszlo Sturz, Dirk Bräuer, and Florian Kargl. A comparative in situ x-radiography and dnn model study of solidification characteristics of an equiaxed dendritic al-ge alloy sample. *Acta Materialia*, 201:286–302, 2020.
- [95] D. Tourret and A. Karma. Three-dimensional dendritic needle network model for alloy solidification. *Acta Materialia*, 120:240–254, 2016.
- [96] F. William Reuter and Harold P. Smith. Full-range solution for the measurement of thin-film surface densities with proton-excited x rays. *Journal of Applied Physics*, 43:4228, 2003.
- [97] D. Tourret, J. C. E. Mertens, E. Lieberman, S. D. Imhoff, J. W. Gibbs, K. Henderson, K. Fezzaa, A. L. Deriy, T. Sun, R. A. Lebensohn, B. M. Patterson, and A. J. Clarke. From solidification processing to microstructure to mechanical properties: A multi-scale x-ray study of an al-cu alloy sample. *Metallurgical and Materials Transactions A*, 48:5529–5546, 2017.
- [98] Charles R. Harris, K. Jarrod Millman, Stéfan J. van der Walt, Ralf Gommers, Pauli Virtanen, David Cournapeau, Eric Wieser, Julian Taylor, Sebastian Berg, Nathaniel J. Smith, Robert Kern, Matti Picus, Stephan Hoyer, Marten H. van Kerkwijk, Matthew Brett, Allan Haldane, Jaime Fernández del Río, Mark Wiebe, Pearu Peterson, Pierre Gérard-Marchant, Kevin Sheppard, Tyler Reddy, Warren Weckesser, Hameer Abbasi, Christoph Gohlke, and Travis E. Oliphant. Array programming with numpy. *Nature 2020* 585:7825, 585:357–362, 2020.
- [99] Almar Klein, Sebastian Wallkötter, Steven Silvester, Anthony Tanbakuchi, Paul Müller, Juan Nunez-Iglesias, Mark Harfouche, actions user, Antony Lee, Matt McCormick, Organicrradiation, Arash Rai, Ariel Ladegaard, Tim D. Smith, and Niklas Vaillan. imageio/imageio: v2.13.1.

- [100] Stéfan van der Walt, Johannes L. Schönberger, Juan Nunez-Iglesias, François Boulogne, Joshua D. Warner, Neil Yager, Emmanuelle Gouillart, and Tony Yu. scikit-image: image processing in python. *PeerJ*, 2:e453, 2014.
- [101] Erich Scheil. Bemerkungen zur schichtkristallbildung. *International Journal of Materials Research*, 34:70–72, 1942.
- [102] W. U. Mirihanage, K. V. Falch, I. Snigireva, A. Snigirev, Y. J. Li, L. Arnberg, and R. H. Mathiesen. Retrieval of three-dimensional spatial information from fast in situ two-dimensional synchrotron radiography of solidification microstructure evolution. *Acta Materialia*, 81:241–247, 2014.
- [103] D. Tourret and Ch A. Gandin. A generalized segregation model for concurrent dendritic, peritectic and eutectic solidification. *Acta Materialia*, 57:2066–2079, 2009.
- [104] Jin Zhang, Wolfgang Ludwig, Yubin Zhang, Hans Henrik B. Sørensen, David J. Rowenhorst, Akinori Yamanaka, Peter W. Voorhees, and Henning F. Poulsen. Grain boundary mobilities in polycrystals. *Acta Materialia*, 191:211–220, 2020.
- [105] Yasumasa Mitsuyama, Tomohiro Takaki, Shinji Sakane, Yasushi Shibuta, and Munekazu Ohno. Permeability tensor for columnar dendritic structures: Phase-field and lattice boltzmann study. *Acta Materialia*, 188:282–287, 2020.
- [106] Antonio Olmedilla, Miha Založnik, and Hervé Combeau. Quantitative 3d mesoscopic modeling of grain interactions during equiaxed dendritic solidification in a thin sample. *Acta Materialia*, 173:249–261, 2019.
- [107] Guido Van Rossum, Fred L Drake, et al. *Python reference manual*. Centrum voor Wiskunde en Informatica Amsterdam, 1995.
- [108] John D. Hunter. Matplotlib: A 2d graphics environment. *Computing in Science and Engineering*, 9:90–95, 2007.
- [109] Inkscape Community. Inkscape project. URL <https://inkscape.org>.
- [110] Chen Chu, Greg Graf, and David W Rosen. Design for additive manufacturing of cellular structures. *Computer-Aided Design and Applications*, 5:686–696, 2008.
- [111] N. Kaufmann, M. Imran, T. M. Wischeropp, C. Emmelmann, S. Siddique, and F. Walther. Influence of process parameters on the quality of aluminium alloy en aw 7075 using selective laser melting (slm). *Physics Procedia*, 83:918–926, 2016.

- [112] John H. Martin, Brennan D. Yahata, Jacob M. Hundley, Justin A. Mayer, Tobias A. Schaeder, and Tresa M. Pollock. 3d printing of high-strength aluminium alloys. *Nature* 2017 549:7672, 549:365–369, 2017.
- [113] Dongdong Gu, Hongmei Zhang, Donghua Dai, Mujian Xia, Chen Hong, and Reinhart Poprawe. Laser additive manufacturing of nano-tic reinforced ni-based nanocomposites with tailored microstructure and performance. *Composites Part B: Engineering*, 163:585–597, 2019.
- [114] R. R. Dehoff, M. Kirka, W. J. Sames, H. Bilheux, A. S. Tremsin, L. E. Lowe, and S. S. Babu. Site specific control of crystallographic grain orientation through electron beam additive manufacturing. *Materials Science and Technology (United Kingdom)*, 31:931–938, 2015.
- [115] A. Plotkowski, J. Ferguson, B. Stump, W. Halsey, V. Paquit, C. Joslin, S. S. Babu, A. Marquez Rossy, M. M. Kirka, and R. R. Dehoff. A stochastic scan strategy for grain structure control in complex geometries using electron beam powder bed fusion. *Additive Manufacturing*, 46, 2021.
- [116] J. A. Spittle. Columnar to equiaxed grain transition in as solidified alloys. *International Materials Reviews*, 51:247–269, 2013.
- [117] M. J. Bermingham, D. H. StJohn, J. Krynen, S. Tedman-Jones, and M. S. Dargusch. Promoting the columnar to equiaxed transition and grain refinement of titanium alloys during additive manufacturing. *Acta Materialia*, 168:261–274, 2019.
- [118] Yan Yan Zhu, Hai Bo Tang, Zhuo Li, Cheng Xu, and Bei He. Solidification behavior and grain morphology of laser additive manufacturing titanium alloys. *Journal of Alloys and Compounds*, 777:712–716, 2019.
- [119] Chunlei Qiu, G. A. Ravi, and Moataz M. Attallah. Microstructural control during direct laser deposition of a beta-titanium alloy. *Materials and Design*, 81:21–30, 2015.
- [120] X. Wu, R. Sharman, J. Mei, and W. Voice. Microstructure and properties of a laser fabricated burn-resistant ti alloy. *Materials and Design*, 25:103–109, 2004.
- [121] Vamsi Krishna Balla, Mitun Das, Ashfaq Mohammad, and Abdulrahman M. Al-Ahmari. Additive manufacturing of gamma-tial: Processing, microstructure, and properties. *Advanced Engineering Materials*, 18:1208–1215, 2016.

- [122] Tomasz Kurzynowski, Konrad Gruber, Wojciech Stopryra, Bogumila Kuznicka, and Edward Chlebus. Correlation between process parameters, microstructure and properties of 316 L stainless steel processed by selective laser melting. *Materials Science and Engineering: A*, 718:64–73, 2018.
- [123] Tien T. Roehling, Rongpei Shi, Saad A. Khairallah, John D. Roehling, Gabe M. Guss, Joseph T. McKeown, and Manyalibo J. Matthews. Controlling grain nucleation and morphology by laser beam shaping in metal additive manufacturing. *Materials and Design*, 195:109071, 2020.
- [124] Janet C. Hunt and B. F. Kiker. Parental time devoted to children in two- and one-wage-earner families. *Economics of Education Review*, 3:75–83, 1984.
- [125] W. Kurz, B. Giovanola, and R. Trivedi. Theory of microstructural development during rapid solidification. *Acta Metallurgica*, 34:823–830, 1986.
- [126] M. Gäumann, R. Trivedi, and W. Kurz. Nucleation ahead of the advancing interface in directional solidification. *Materials Science and Engineering: A*, 226-228: 763–769, 1997.
- [127] M. Gäumann, C. Bezençon, P. Canalis, and W. Kurz. Single-crystal laser deposition of superalloys: processing-microstructure maps. *Acta Materialia*, 49: 1051–1062, 2001.
- [128] Wilfried Kurz. Solidification microstructure-processing maps: Theory and application\*\*. *Advanced Engineering Materials*, 3:443–452, 2001.
- [129] W. Kurz, C. Bezençon, and M. Gäumann. Columnar to equiaxed transition in solidification processing. *Science and Technology of Advanced Materials*, 2: 185–191, 2001.
- [130] P. A. Kobryn and S. L. Semiatin. Microstructure and texture evolution during solidification processing of ti-6al-4v. *Journal of Materials Processing Technology*, 135:330–339, 2003.
- [131] Alec I. Saville, Sven C. Vogel, Adam Creuziger, Jake T. Benzing, Adam L. Pilchak, Peeyush Nandwana, Jonah Klemm-Toole, Kester D. Clarke, S. Lee Semiatin, and Amy J. Clarke. Texture evolution as a function of scan strategy and build height in electron beam melted ti-6al-4v. *Additive Manufacturing*, 46:102118, 2021.
- [132] Yao Jian Liang, An Li, Xu Cheng, Xiao Tong Pang, and Hua Ming Wang. Prediction of primary dendritic arm spacing during laser rapid directional solidification of single-crystal nickel-base superalloys. *Journal of Alloys and Compounds*, 688:133–142, 2016.

- [133] Yao Jian Liang, Xu Cheng, Jia Li, and Hua Ming Wang. Microstructural control during laser additive manufacturing of single-crystal nickel-base superalloys: New processing-microstructure maps involving powder feeding. *Materials and Design*, 130:197–207, 2017.
- [134] Chu Lun Alex Leung, Sebastian Marussi, Michael Towrie, Jesus del Val Garcia, Robert C. Atwood, Andrew J. Bodey, Julian R. Jones, Philip J. Withers, and Peter D. Lee. Laser-matter interactions in additive manufacturing of stainless steel ss316l and 13-93 bioactive glass revealed by in situ x-ray imaging. *Additive Manufacturing*, 24:647–657, 2018.
- [135] S. Mohammad H. Hojjatzadeh, Niranjan D. Parab, Wentao Yan, Qilin Guo, Lianghua Xiong, Cang Zhao, Minglei Qu, Luis I. Escano, Xianghui Xiao, Kamel Fezzaa, Wes Everhart, Tao Sun, and Lianyi Chen. Pore elimination mechanisms during 3d printing of metals. *Nature Communications* 2019 10:1, 10:1–8, 2019.
- [136] Sarah J. Wolff, Hao Wu, Niranjan Parab, Cang Zhao, Kornel F. Ehmann, Tao Sun, and Jian Cao. In-situ high-speed x-ray imaging of piezo-driven directed energy deposition additive manufacturing. *Scientific Reports* 2019 9:1, 9:1–14, 2019.
- [137] T. LaGrange, M. R. Armstrong, K. Boyden, C. G. Brown, G. H. Campbell, J. D. Colvin, W. J. DeHope, A. M. Frank, D. J. Gibson, F. V. Hartemann, J. S. Kim, W. E. King, B. J. Pyke, B. W. Reed, M. D. Shirk, R. M. Shuttlesworth, B. C. Stuart, B. R. Torralva, and N. D. Browning. Single-shot dynamic transmission electron microscopy. *Applied Physics Letters*, 89:044105, 2006.
- [138] Thomas LaGrange, Geoffrey H. Campbell, B. W. Reed, Mitra Taheri, J. Bradley Pesavento, Judy S. Kim, and Nigel D. Browning. Nanosecond time-resolved investigations using the in situ of dynamic transmission electron microscope (dtem). *Ultramicroscopy*, 108:1441–1449, 2008.
- [139] Judy S. Kim, Thomas LaGrange, Bryan W. Reed, Mitra L. Taheri, Michael R. Armstrong, Wayne E. King, Nigel D. Browning, and Geoffrey H. Campbell. Imaging of transient structures using nanosecond in situ tem. *Science*, 321:1472–1475, 2008.
- [140] Geoffrey H. Campbell, Thomas Lagrange, Judy S. Kim, Bryan W. Reed, and Nigel D. Browning. Quantifying transient states in materials with the dynamic transmission electron microscope. *Journal of Electron Microscopy*, 59:S67–S74, 2010.

- [141] Andreas Kulovits, Jörg M.K. Wiezorek, Thomas Lagrange, Bryan W. Reed, and Geoffrey H. Campbell. Revealing the transient states of rapid solidification in aluminum thin films using ultrafast in situ transmission electron microscopy. <http://dx.doi.org/10.1080/09500839.2011.558030>, 91:287–296, 2011.
- [142] Thomas LaGrange, Bryan W. Reed, Melissa K. Santala, Joseph T. McKeown, Andreas Kulovits, Jörg M.K. Wiezorek, Liliya Nikolova, Federico Rosei, Bradely J. Siwick, and Geoffrey H. Campbell. Approaches for ultrafast imaging of transient materials processes in the transmission electron microscope. *Micron*, 43: 1108–1120, 2012.
- [143] M. K. Santala, B. W. Reed, S. Raoux, T. Topuria, T. Lagrange, and G. H. Campbell. Irreversible reactions studied with nanosecond transmission electron microscopy movies: Laser crystallization of phase change materials. *Applied Physics Letters*, 102:174105, 2013.
- [144] Joseph T. McKeown, Andreas K. Kulovits, Can Liu, Kai Zweiacker, Bryan W. Reed, Thomas Lagrange, Jörg M.K. Wiezorek, and Geoffrey H. Campbell. In situ transmission electron microscopy of crystal growth-mode transitions during rapid solidification of a hypoeutectic al–cu alloy. *Acta Materialia*, 65:56–68, 2014.
- [145] K. W. Zweiacker, M. A. Gordillo, C. Liu, J. T. McKeown, G. H. Campbell, T. LaGrange, B. W. Reed, and J. M. Wiezorek. Quantitative phase analysis of rapid solidification products in al-cu alloys by automated crystal orientation mapping in the tem. *Microscopy and Microanalysis*, 21:1465–1466, 2015.
- [146] Thomas LaGrange, Bryan W. Reed, and Daniel J. Masiel. Movie-mode dynamic electron microscopy. *MRS Bulletin*, 40:22–28, 2015.
- [147] John D. Roehling, Daniel R. Coughlin, John W. Gibbs, J. Kevin Baldwin, James C.E. Mertens, Geoffrey H. Campbell, Amy J. Clarke, and Joseph T. McKeown. Rapid solidification growth mode transitions in al-si alloys by dynamic transmission electron microscopy. *Acta Materialia*, 131:22–30, 2017.
- [148] Kaihua Ji, Elaheh Dorari, Amy J. Clarke, and Alain Karma. Microstructural pattern formation during far-from-equilibrium alloy solidification. *Physical Review Letters*, 130, 2023.
- [149] Anil Kokaram. An algorithm for total variation minimization and applications. *Journal of Mathematical Imaging and Vision*, 20:89–97, 2004.
- [150] T. Y. Zhang and C. Y. Suen. A fast parallel algorithm for thinning digital patterns. *Communications of the ACM*, 27:236–239, 1984.

- [151] J. A. Nelder and R. Mead. A simplex method for function minimization. *The Computer Journal*, 7:308–313, 1965.
- [152] Jean Serra. *Image Analysis and Mathematical Morphology: Vol.: 2: Theoretical Advances*. Academic Press, 1988.
- [153] Serge Beucher. The watershed transformation applied to image segmentation. *Scanning Microscopy*, 1992.
- [154] Per Erik Danielsson. Euclidean distance mapping. *Computer Graphics and Image Processing*, 14:227–248, 1980.
- [155] Chanho Jung and Changick Kim. Segmenting clustered nuclei using h-minima transform-based marker extraction and contour parameterization. *IEEE Transactions on Biomedical Engineering*, 57:2600–2604, 10 2010.
- [156] John Canny. A computational approach to edge detection. *IEEE Transactions on Pattern Analysis and Machine Intelligence*, PAMI-8:679–698, 11 1986. ISSN 0162-8828.

- [157] Pauli Virtanen, Ralf Gommers, Travis E. Oliphant, Matt Haberland, Tyler Reddy, David Cournapeau, Evgeni Burovski, Pearu Peterson, Warren Weckesser, Jonathan Bright, Stéfan J. van der Walt, Matthew Brett, Joshua Wilson, K. Jarrod Millman, Nikolay Mayorov, Andrew R.J. Nelson, Eric Jones, Robert Kern, Eric Larson, C. J. Carey, İlhan Polat, Yu Feng, Eric W. Moore, Jake VanderPlas, Denis Laxalde, Josef Perktold, Robert Cimrman, Ian Henriksen, E. A. Quintero, Charles R. Harris, Anne M. Archibald, Antônio H. Ribeiro, Fabian Pedregosa, Paul van Mulbregt, Aditya Vijaykumar, Alessandro Pietro Bardelli, Alex Rothberg, Andreas Hilboll, Andreas Kloeckner, Anthony Scopatz, Antony Lee, Ariel Rokem, C. Nathan Woods, Chad Fulton, Charles Masson, Christian Häggström, Clark Fitzgerald, David A. Nicolson, David R. Hagen, Dmitrii V. Pasechnik, Emanuele Olivetti, Eric Martin, Eric Wieser, Fabrice Silva, Felix Lenders, Florian Wilhelm, G. Young, Gavin A. Price, Gert Ludwig Ingold, Gregory E. Allen, Gregory R. Lee, Hervé Audren, Irvin Probst, Jörg P. Dietrich, Jacob Silterra, James T. Webber, Janko Slavič, Joel Nothman, Johannes Buchner, Johannes Kulick, Johannes L. Schönberger, José Vinícius de Miranda Cardoso, Joscha Reimer, Joseph Harrington, Juan Luis Cano Rodríguez, Juan Nunez-Iglesias, Justin Kuczynski, Kevin Tritz, Martin Thoma, Matthew Newville, Matthias Kümmerer, Maximilian Bolingbroke, Michael Tartre, Mikhail Pak, Nathaniel J. Smith, Nikolai Nowaczyk, Nikolay Shebanov, Oleksandr Pavlyk, Per A. Brodtkorb, Perry Lee, Robert T. McGibbon, Roman Feldbauer, Sam Lewis, Sam Tygier, Scott Sievert, Sebastiano Vigna, Stefan Peterson, Surhud More, Tadeusz Pudlik, Takuya Oshima, Thomas J. Pingel, Thomas P. Robitaille, Thomas Spura, Thouis R. Jones, Tim Cera, Tim Leslie, Tiziano Zito, Tom Krauss, Utkarsh Upadhyay, Yaroslav O. Halchenko, and Yoshiaki Vázquez-Baeza. Scipy 1.0: fundamental algorithms for scientific computing in python. *Nature Methods* 2020 17:3, 17:261–272, 2020.
- [158] Nick Kanopoulos, Nagesh Vasanthavada, and Robert L. Baker. Design of an image edge detection filter using the sobel operator. *IEEE Journal of Solid-State Circuits*, 23:358–367, 1988.
- [159] Georges Voronoi. Nouvelles applications des paramètres continus à la théorie des formes quadratiques. deuxième mémoire. recherches sur les paralléloèdres primitifs. *Journal für die Reine und Angewandte Mathematik*, pages 198–287, 7 1908.
- [160] Boris Delaunay. Sur la sphere vide. *Izv. Akad. Nauk SSSR, Otdelenie Matematicheskii i Estestvennyka Nauk*, 7:1–2, 1934.
- [161] Franz Aurenhammer. Voronoi diagrams-a survey of a fundamental geometric data structure. *ACM Computing Surveys*, 23:345–405, 1991.

- [162] Quan Wen, Hang Chang, and Bahram Parvin. A delaunay triangulation approach for segmenting clumps of nuclei. *Proceedings - 2009 IEEE International Symposium on Biomedical Imaging: From Nano to Macro, ISBI 2009*, pages 9–12, 2009.
- [163] Kirill Simonov and The-YAML-Community. Pyyaml. URL <https://pyyaml.org/wiki/PyYAML>.
- [164] Rick van Hattem and numpy-stl contributors. numpy-stl: 3.0.0. URL <https://pypi.org/project/numpy-stl/>.
- [165] Qian-Yi Zhou, Jaesik Park, and Vladlen Koltun. Open3d: A modern library for 3d data processing. 2018.
- [166] William E. Lorensen and Harvey E. Cline. Marching cubes: A high resolution 3d surface construction algorithm. *ACM SIGGRAPH Computer Graphics*, 21: 163–169, 1987.
- [167] Thomas Lewiner, Hélio Lopes, Antônio Wilson Vieira, and Geovan Tavares. Efficient implementation of marching cubes' cases with topological guarantees. *Journal of Graphics Tools*, 8:1–15, 2012.
- [168] Michael Garland and Paul S. Heckbert. Surface simplification using quadric error metrics. *Proceedings of the 24th Annual Conference on Computer Graphics and Interactive Techniques, SIGGRAPH 1997*, pages 209–216, 1997.

## APPENDIX COPYRIGHT PERMISSIONS

Proof of permission from the publisher and co-authors to reprint the 2023 JOM article “Integrating In Situ x-Ray Imaging, Energy Dispersive Spectroscopy, and Calculated Phase Diagram Analysis of Solute Segregation During Solidification of an Al-Ag Alloy” [77] as Chapter 3.

### **A.1 Permission from Publisher**

The following pages express permission from the publisher of JOM, Springer Nature, to reprint the journal article in question as part of this thesis.

SPRINGER NATURE LICENSE  
TERMS AND CONDITIONS

Oct 24, 2022

---

---

This Agreement between Mr. Gus Becker ("You") and Springer Nature ("Springer Nature") consists of your license details and the terms and conditions provided by Springer Nature and Copyright Clearance Center.

License Number        5350311265027

License date        Jul 15, 2022

Licensed Content  
Publisher            Springer Nature

Licensed Content  
Publication        JOM Journal of the Minerals, Metals and Materials Society

Licensed Content Title        Integrating In Situ x-Ray Imaging, Energy Dispersive Spectroscopy,  
and Calculated Phase Diagram Analysis of Solute Segregation  
During Solidification of an Al-Ag Alloy

Licensed Content  
Author              C. Gus Becker et al

Licensed Content Date Sep 20, 2021

Type of Use        Thesis/Dissertation

Requestor type        academic/university or research institute

Format              print and electronic

Portion              full article/chapter

Will you be no  
translating?

Circulation/distribution 1 - 29

Author of this Springer yes  
Nature content

Title Algorithmic Analyses of Image-Based Material Investigations

Institution name Colorado School of Mines

Expected presentation Aug 2022  
date

Mr. Gus Becker  
209 19th St NE #1

Requestor Location  
WASHINGTON, DC 20002  
United States  
Attn: Colorado School of Mines

Total 0.00 USD

Terms and Conditions

### **Springer Nature Customer Service Centre GmbH Terms and Conditions**

This agreement sets out the terms and conditions of the licence (the **Licence**) between you and **Springer Nature Customer Service Centre GmbH** (the **Licensor**). By clicking 'accept' and completing the transaction for the material (**Licensed Material**), you also confirm your acceptance of these terms and conditions.

#### **1. Grant of License**

**1. 1.** The Licensor grants you a personal, non-exclusive, non-transferable, world-wide licence to reproduce the Licensed Material for the purpose specified in your order only. Licences are granted for the specific use requested in the order and for no other use, subject to the conditions below.

**1. 2.** The Licensor warrants that it has, to the best of its knowledge, the rights to license reuse of the Licensed Material. However, you should ensure that the material you are requesting is original to the Licensor and does not carry the copyright of

another entity (as credited in the published version).

**1. 3.** If the credit line on any part of the material you have requested indicates that it was reprinted or adapted with permission from another source, then you should also seek permission from that source to reuse the material.

## 2. Scope of Licence

**2. 1.** You may only use the Licensed Content in the manner and to the extent permitted by these Ts&Cs and any applicable laws.

**2. 2.** A separate licence may be required for any additional use of the Licensed Material, e.g. where a licence has been purchased for print only use, separate permission must be obtained for electronic re-use. Similarly, a licence is only valid in the language selected and does not apply for editions in other languages unless additional translation rights have been granted separately in the licence. Any content owned by third parties are expressly excluded from the licence.

**2. 3.** Similarly, rights for additional components such as custom editions and derivatives require additional permission and may be subject to an additional fee.

Please apply to

[Journalpermissions@springernature.com](mailto:Journalpermissions@springernature.com)/[bookpermissions@springernature.com](mailto:bookpermissions@springernature.com) for these rights.

**2. 4.** Where permission has been granted **free of charge** for material in print, permission may also be granted for any electronic version of that work, provided that the material is incidental to your work as a whole and that the electronic version is essentially equivalent to, or substitutes for, the print version.

**2. 5.** An alternative scope of licence may apply to signatories of the [STM Permissions Guidelines](#), as amended from time to time.

## 3. Duration of Licence

**3. 1.** A licence for is valid from the date of purchase ('Licence Date') at the end of the relevant period in the below table:

Scope of Licence	Duration of Licence
Post on a website	12 months
Presentations	12 months
Books and journals	Lifetime of the edition in the language purchased

## 4. Acknowledgement

**4. 1.** The Licensor's permission must be acknowledged next to the Licenced Material in print. In electronic form, this acknowledgement must be visible at the same time as the figures/tables/illustrations or abstract, and must be hyperlinked to the journal/book's homepage. Our required acknowledgement format is in the Appendix below.

## **5. Restrictions on use**

**5. 1.** Use of the Licensed Material may be permitted for incidental promotional use and minor editing privileges e.g. minor adaptations of single figures, changes of format, colour and/or style where the adaptation is credited as set out in Appendix 1 below. Any other changes including but not limited to, cropping, adapting, omitting material that affect the meaning, intention or moral rights of the author are strictly prohibited.

**5. 2.** You must not use any Licensed Material as part of any design or trademark.

**5. 3.** Licensed Material may be used in Open Access Publications (OAP) before publication by Springer Nature, but any Licensed Material must be removed from OAP sites prior to final publication.

## **6. Ownership of Rights**

**6. 1.** Licensed Material remains the property of either Licensor or the relevant third party and any rights not explicitly granted herein are expressly reserved.

## **7. Warranty**

IN NO EVENT SHALL LICENSOR BE LIABLE TO YOU OR ANY OTHER PARTY OR ANY OTHER PERSON OR FOR ANY SPECIAL, CONSEQUENTIAL, INCIDENTAL OR INDIRECT DAMAGES, HOWEVER CAUSED, ARISING OUT OF OR IN CONNECTION WITH THE DOWNLOADING, VIEWING OR USE OF THE MATERIALS REGARDLESS OF THE FORM OF ACTION, WHETHER FOR BREACH OF CONTRACT, BREACH OF WARRANTY, TORT, NEGLIGENCE, INFRINGEMENT OR OTHERWISE (INCLUDING, WITHOUT LIMITATION, DAMAGES BASED ON LOSS OF PROFITS, DATA, FILES, USE, BUSINESS OPPORTUNITY OR CLAIMS OF THIRD PARTIES), AND WHETHER OR NOT THE PARTY HAS BEEN ADVISED OF THE POSSIBILITY OF SUCH DAMAGES. THIS LIMITATION SHALL APPLY NOTWITHSTANDING ANY FAILURE OF ESSENTIAL PURPOSE OF ANY LIMITED REMEDY PROVIDED HEREIN.

## **8. Limitations**

**8. 1. BOOKS ONLY:** Where 'reuse in a dissertation/thesis' has been selected the following terms apply: Print rights of the final author's accepted manuscript (for clarity, NOT the published version) for up to 100 copies, electronic rights for use only on a personal website or institutional repository as defined by the Sherpa guideline ([www.sherpa.ac.uk/romeo/](http://www.sherpa.ac.uk/romeo/)).

**8. 2.** For content reuse requests that qualify for permission under the [STM Permissions Guidelines](#), which may be updated from time to time, the STM Permissions Guidelines supersede the terms and conditions contained in this licence.

## **9. Termination and Cancellation**

**9. 1.** Licences will expire after the period shown in Clause 3 (above).

**9. 2.** Licensee reserves the right to terminate the Licence in the event that payment is not received in full or if there has been a breach of this agreement by you.

## **Appendix 1 — Acknowledgements:**

### **For Journal Content:**

Reprinted by permission from [the Licensor]: [Journal Publisher (e.g. Nature/Springer/Palgrave)] [JOURNAL NAME] [REFERENCE CITATION (Article name, Author(s) Name), [COPYRIGHT] (year of publication)

### **For Advance Online Publication papers:**

Reprinted by permission from [the Licensor]: [Journal Publisher (e.g. Nature/Springer/Palgrave)] [JOURNAL NAME] [REFERENCE CITATION (Article name, Author(s) Name), [COPYRIGHT] (year of publication), advance online publication, day month year (doi: 10.1038/sj.[JOURNAL ACRONYM].)

### **For Adaptations/Translations:**

Adapted/Translated by permission from [the Licensor]: [Journal Publisher (e.g. Nature/Springer/Palgrave)] [JOURNAL NAME] [REFERENCE CITATION (Article name, Author(s) Name), [COPYRIGHT] (year of publication)

### **Note: For any republication from the British Journal of Cancer, the following credit line style applies:**

Reprinted/adapted/translated by permission from [the Licensor]: on behalf of Cancer Research UK: : [Journal Publisher (e.g. Nature/Springer/Palgrave)] [JOURNAL NAME] [REFERENCE CITATION (Article name, Author(s) Name), [COPYRIGHT] (year of publication)

### **For Advance Online Publication papers:**

Reprinted by permission from The [the Licensor]: on behalf of Cancer Research UK: [Journal Publisher (e.g. Nature/Springer/Palgrave)] [JOURNAL NAME] [REFERENCE CITATION (Article name, Author(s) Name), [COPYRIGHT] (year of publication), advance online publication, day month year (doi: 10.1038/sj. [JOURNAL ACRONYM])

### **For Book content:**

Reprinted/adapted by permission from [the Licensor]: [Book Publisher (e.g. Palgrave Macmillan, Springer etc) [Book Title] by [Book author(s)] [COPYRIGHT] (year of publication)

## **Other Conditions:**

Questions? [customercare@copyright.com](mailto:customercare@copyright.com) or +1-855-239-3415 (toll free in the US) or  
+1-978-646-2777.

---

---

## **A.2 Permission from Co-Authors**

The following pages express permission from the co-authors of the journal article in question to reprint the article as part of this thesis.

## Gus Becker

---

**From:** damien.tourret@imdea.org  
**Sent:** Monday, October 24, 2022 4:21 PM  
**To:** Chandler Becker  
**Cc:** Douglas Smith; Brian Rodgers; Imhoff, Seth D; jwgibbs@lanl.gov; jhunter@lanl.gov; Espy, Michelle A; Kester Clarke; Amy Clarke  
**Subject:** [External] Re: Requesting Permission to Use JOM 2021 Paper in Thesis

Of course!! Best of luck with the thesis!

Damien

On 2022-10-24 22:12, Chandler Becker wrote:

Hi all,

I hope everyone is doing well.

I'm writing you all to ask for each of your permission to include our JOM 2021 paper "Integrating In Situ x-Ray Imaging, Energy Dispersive Spectroscopy, and Calculated Phase Diagram Analysis of Solute Segregation During Solidification of an Al-Ag Alloy" as a chapter in my thesis. If everybody agrees, I will include each of your responses in an appendix in my thesis. A simple email response will suffice!

Thank you,

**C. Gus Becker** (he, him, his)

CANFSA: Center for Advanced Non-Ferrous Structural Alloys  
PhD Candidate, Materials Science, Colorado School of Mines  
B.S. Engineering Physics 2017, [Colorado School of Mines](#)

## Gus Becker

---

**From:** Douglas Smith  
**Sent:** Monday, October 24, 2022 6:01 PM  
**To:** Chandler Becker  
**Subject:** RE: Requesting Permission to Use JOM 2021 Paper in Thesis

Hi Gus,

That's fine with me. Best of luck with writing!

-Doug

---

**From:** Chandler Becker <chbecker@mines.edu>  
**Sent:** Monday, October 24, 2022 2:12 PM  
**To:** damien.tourret@imdea.org; Douglas Smith <dodsmith@mines.edu>; Brian Rodgers <brodgers@mines.edu>; Imhoff, Seth D <sdi@lanl.gov>; jwgibbs@lanl.gov; jhunter@lanl.gov; Espy, Michelle A <espy@lanl.gov>; Kester Clarke <kclarke@mines.edu>; Amy Clarke <amyclarke@mines.edu>  
**Subject:** Requesting Permission to Use JOM 2021 Paper in Thesis

Hi all,

I hope everyone is doing well.

I'm writing you all to ask for each of your permission to include our JOM 2021 paper "Integrating In Situ x-Ray Imaging, Energy Dispersive Spectroscopy, and Calculated Phase Diagram Analysis of Solute Segregation During Solidification of an Al-Ag Alloy" as a chapter in my thesis. If everybody agrees, I will include each of your responses in an appendix in my thesis. A simple email response will suffice!

Thank you,

**C. Gus Becker** (he, him, his)

CANFSA: Center for Advanced Non-Ferrous Structural Alloys  
PhD Candidate, Materials Science, [Colorado School of Mines](#)  
B.S. Engineering Physics 2017, [Colorado School of Mines](#)

## Gus Becker

---

**From:** Brian Rodgers  
**Sent:** Monday, October 24, 2022 4:14 PM  
**To:** Chandler Becker  
**Subject:** RE: Requesting Permission to Use JOM 2021 Paper in Thesis

Hey Gus,

Permission granted. Good luck on the thesis!

Best,  
Brian

---

**From:** Chandler Becker <chbecker@mines.edu>  
**Sent:** Monday, October 24, 2022 2:12 PM  
**To:** damien.tourret@imdea.org; Douglas Smith <dodsmith@mines.edu>; Brian Rodgers <brodgers@mines.edu>; lmhoff, Seth D <sdi@lanl.gov>; jwgibbs@lanl.gov; jhunter@lanl.gov; Espy, Michelle A <espy@lanl.gov>; Kester Clarke <kclarke@mines.edu>; Amy Clarke <amyclarke@mines.edu>  
**Subject:** Requesting Permission to Use JOM 2021 Paper in Thesis

Hi all,

I hope everyone is doing well.

I'm writing you all to ask for each of your permission to include our JOM 2021 paper "Integrating In Situ x-Ray Imaging, Energy Dispersive Spectroscopy, and Calculated Phase Diagram Analysis of Solute Segregation During Solidification of an Al-Ag Alloy" as a chapter in my thesis. If everybody agrees, I will include each of your responses in an appendix in my thesis. A simple email response will suffice!

Thank you,

**C. Gus Becker** (he, him, his)

CANFSA: Center for Advanced Non-Ferrous Structural Alloys  
PhD Candidate, Materials Science, [Colorado School of Mines](#)  
B.S. Engineering Physics 2017, [Colorado School of Mines](#)

## Gus Becker

---

**From:** Gibbs, John W <jwgibbs@lanl.gov>  
**Sent:** Tuesday, October 25, 2022 1:46 PM  
**To:** Espy, Michelle A; Chandler Becker; damien.tourret@imdea.org; Douglas Smith; Brian Rodgers; Imhoff, Seth D; Hunter, James F; Kester Clarke; Amy Clarke  
**Subject:** [External] Re: Requesting Permission to Use JOM 2021 Paper in Thesis

Gus,

That's ok with me.

John

---

**From:** Espy, Michelle A  
**Sent:** Monday, October 24, 2022 5:14 PM  
**To:** Chandler Becker; damien.tourret@imdea.org; Douglas Smith; Brian Rodgers; Imhoff, Seth D; Gibbs, John W; Hunter, James F; Kester Clarke; Amy Clarke  
**Subject:** RE: Requesting Permission to Use JOM 2021 Paper in Thesis

Hi Gus,

You have my permission.

Michelle

---

**From:** Chandler Becker <chbecker@mines.edu>  
**Sent:** Monday, October 24, 2022 2:12 PM  
**To:** damien.tourret@imdea.org; Douglas Smith <dodsmith@mines.edu>; Brian Rodgers <brodgers@mines.edu>; Imhoff, Seth D <sdi@lanl.gov>; Gibbs, John W <jwgibbs@lanl.gov>; Hunter, James F <jhunter@lanl.gov>; Espy, Michelle A <espy@lanl.gov>; Kester Clarke <kclarke@mines.edu>; Amy Clarke <amyclarke@mines.edu>  
**Subject:** [EXTERNAL] Requesting Permission to Use JOM 2021 Paper in Thesis

Hi all,

I hope everyone is doing well.

## Gus Becker

---

**From:** Imhoff, Seth D <sdi@lanl.gov>  
**Sent:** Monday, October 24, 2022 7:19 PM  
**To:** Chandler Becker  
**Subject:** [External] RE: Requesting Permission to Use JOM 2021 Paper in Thesis

You have my permission to use the paper.

Thanks,  
Seth

---

Seth D. Imhoff  
Los Alamos National Laboratory  
Sigma Division,  $\Sigma$   
P.O. Box 1663 / Mail Stop G774  
Los Alamos, NM 87545  
Tel: (505) 664-0747  
Pager: (505) 664-3273  
Cell: (505) 695-3514  
E-mail: [sdi@lanl.gov](mailto:sdi@lanl.gov)

---

\*\*correspondence\*\*

---

**From:** Chandler Becker <chbecker@mines.edu>  
**Sent:** Monday, October 24, 2022 2:12 PM  
**To:** damien.tourret@imdea.org; Douglas Smith <dodsmith@mines.edu>; Brian Rodgers <brodgers@mines.edu>; Imhoff, Seth D <sdi@lanl.gov>; Gibbs, John W <jwgibbs@lanl.gov>; Hunter, James F <jhunter@lanl.gov>; Espy, Michelle A <espy@lanl.gov>; Kester Clarke <kclarke@mines.edu>; Amy Clarke <amyclarke@mines.edu>  
**Subject:** [EXTERNAL] Requesting Permission to Use JOM 2021 Paper in Thesis

Hi all,

I hope everyone is doing well.

I'm writing you all to ask for each of your permission to include our JOM 2021 paper "Integrating In Situ x-Ray Imaging, Energy Dispersive Spectroscopy, and Calculated Phase Diagram Analysis of Solute Segregation During Solidification of an Al-Ag Alloy" as a chapter in my thesis. If everybody agrees, I will include each of your responses in an appendix in my thesis. A simple email response will suffice!

Thank you,

**C. Gus Becker** (he, him, his)  
CANFSA: Center for Advanced Non-Ferrous Structural Alloys  
PhD Candidate, Materials Science, [Colorado School of Mines](#)  
B.S. Engineering Physics 2017, [Colorado School of Mines](#)

## Gus Becker

---

**From:** Hunter, James F <jhunter@lanl.gov>  
**Sent:** Monday, October 24, 2022 7:06 PM  
**To:** Chandler Becker; damien.tourret@imdea.org; Douglas Smith; Brian Rodgers; Imhoff, Seth D; Gibbs, John W; Espy, Michelle A; Kester Clarke; Amy Clarke  
**Subject:** [External] RE: Requesting Permission to Use JOM 2021 Paper in Thesis

Hi Gus,  
You have my permission.

James

---

**From:** Chandler Becker <chbecker@mines.edu>  
**Sent:** Monday, October 24, 2022 2:12 PM  
**To:** damien.tourret@imdea.org; Douglas Smith <dodsmith@mines.edu>; Brian Rodgers <brodgers@mines.edu>; Imhoff, Seth D <sdi@lanl.gov>; Gibbs, John W <jwgibbs@lanl.gov>; Hunter, James F <jhunter@lanl.gov>; Espy, Michelle A <espy@lanl.gov>; Kester Clarke <kclarke@mines.edu>; Amy Clarke <amyclarke@mines.edu>  
**Subject:** [EXTERNAL] Requesting Permission to Use JOM 2021 Paper in Thesis

Hi all,  
I hope everyone is doing well.

I'm writing you all to ask for each of your permission to include our JOM 2021 paper "Integrating In Situ x-Ray Imaging, Energy Dispersive Spectroscopy, and Calculated Phase Diagram Analysis of Solute Segregation During Solidification of an Al-Ag Alloy" as a chapter in my thesis. If everybody agrees, I will include each of your responses in an appendix in my thesis. A simple email response will suffice!

Thank you,

**C. Gus Becker** (he, him, his)  
CANFSA: Center for Advanced Non-Ferrous Structural Alloys  
PhD Candidate, Materials Science, [Colorado School of Mines](#)  
B.S. Engineering Physics 2017, [Colorado School of Mines](#)

## Gus Becker

---

**From:** Espy, Michelle A <espy@lanl.gov>  
**Sent:** Monday, October 24, 2022 7:15 PM  
**To:** Chandler Becker; damien.tourret@imdea.org; Douglas Smith; Brian Rodgers; Imhoff, Seth D; Gibbs, John W; Hunter, James F; Kester Clarke; Amy Clarke  
**Subject:** [External] RE: Requesting Permission to Use JOM 2021 Paper in Thesis

Hi Gus,

You have my permission.

Michelle

---

**From:** Chandler Becker <chbecker@mines.edu>  
**Sent:** Monday, October 24, 2022 2:12 PM  
**To:** damien.tourret@imdea.org; Douglas Smith <dodsmith@mines.edu>; Brian Rodgers <brodgers@mines.edu>; Imhoff, Seth D <sdi@lanl.gov>; Gibbs, John W <jwgibbs@lanl.gov>; Hunter, James F <jhunter@lanl.gov>; Espy, Michelle A <espy@lanl.gov>; Kester Clarke <kclarke@mines.edu>; Amy Clarke <amyclarke@mines.edu>  
**Subject:** [EXTERNAL] Requesting Permission to Use JOM 2021 Paper in Thesis

Hi all,

I hope everyone is doing well.

I'm writing you all to ask for each of your permission to include our JOM 2021 paper "Integrating In Situ x-Ray Imaging, Energy Dispersive Spectroscopy, and Calculated Phase Diagram Analysis of Solute Segregation During Solidification of an Al-Ag Alloy" as a chapter in my thesis. If everybody agrees, I will include each of your responses in an appendix in my thesis. A simple email response will suffice!

Thank you,

**C. Gus Becker** (he, him, his)

CANFSA: Center for Advanced Non-Ferrous Structural Alloys  
PhD Candidate, Materials Science, [Colorado School of Mines](#)  
B.S. Engineering Physics 2017, [Colorado School of Mines](#)